Theoretical studies on ultrafast dynamics of liquid water using linear and nonlinear spectroscopy

Sho Imoto

Department of Functional Molecular Science

School of Physical Sciences

The Graduate University for Advanced Studies

2013

Contents

Chapter 1 General introduction 1

Chapter 2 Theoretical background and computational method 14

2.1 Linear response theory and IR spectroscopy 14

2.2 Third-order response and third-order infrared spectroscopy 18

2.3 Basis of molecular dynamics simulations 22

2.4 TTM3-F potential 24

Chapter 3 IR spectra of the HOH bend in liquid water and ice 28

3.1 Introduction 28

3.2 Computational method 30

3.3 Computational details 31

3.4 Results and discussion 34

3.5 Conclusions 46

Chapter 4 Frequency fluctuation of the OH stretch and the HOH bend in liquid water 50

4.1 Introduction 50

4.2 Theoretical method and computational details 52

4.3 Results and discussion 56

4.4 Conclusions 65

Chapter 5 Energy relaxation of the OH stretch and the HOH bend in liquid water 70

5.1 Introduction 70

5.2 Computational methods and details 72

5.3 Results and discussion 78

5.4 Conclusion 87

Chapter 6 General conclusion 91

Acknowledgments

This dissertation is the summary of my works carried out at Department of Functional molecular Science, School of Physics, the Graduate University of Advanced Studies from April 2010 to September 2013.

I would like to express my sincere gratitude to my supervisor, Professor Shinji Saito, for invaluable instruction, discussion, and warm encouragement. He provided me the opportunity of studying interesting theme. Acknowledgements are made to the member of Saito group: Professor Kang Kim, Dr. Chigusa Kobayashi, Dr. Takuma Yagasaki, Dr. Takashi Sumikama, Dr. Masahiro Higashi, Dr. Junichi Ono, Harumi Kikuoka, Ritsuko Kawaguchi, and Naoko Kondo.

I thank Professor Iwao Ohmine for his continuous encouragement. I spent my undergraduate and master course in his laboratory. I wish heartily to thank Dr. Sotiris Xantheas for the collaborative study. I also wish to thank Professor Andrei Tokmakoff for valuable discussion.

Finally, I would like to thank my family for all their love and encouragement.

Chapter 1

General introduction

Water is the most abundant liquid on the earth and it has a lot of anomalous thermodynamic and dynamical properties, e.g. maximum density at 4 degree Celsius, large heat capacity, and ultrafast energy dissipation [1]. These thermodynamic and dynamic properties of liquid water arise from its fleeting three-dimensional hydrogen bond (HB) network [2]. There are many experimental and theoretical studies on the HB in water [3,4]. In particular, the infrared (IR) spectrum of the water has intensively been investigated because it is sensitive to the HBs structure [5]. Figure 1.1 shows the experimental IR spectrum of liquid water. The broad band below 1000 cm^{-1} arises from the intermolecular motions. The band from 300 to 1000 cm^{-1} results from the librational motions. In particular, the high frequency part (~800 cm^{-1}) is related to the librational motion around molecular y-axis (Fig. 1.2(a)), whereas the low frequency part (~500 cm^{-1}) is caused by the librational motions around molecular x- and z-axes (Figs. 1.2(b-c)). The shoulders at ~ 200 and ~60 cm^{-1} arise from the HB stretch (Fig. 1.2(d)) and the HB bend (Fig. 1.2(e)), respectively. The peaks at 1600 and 3500 cm^{-1} are assigned to the HOH bend and the OH stretch, respectively. It is well known that the IR spectrum of the OH stretch is sensitive to the local HB strength; the strong HB makes the OH stretch frequency low.

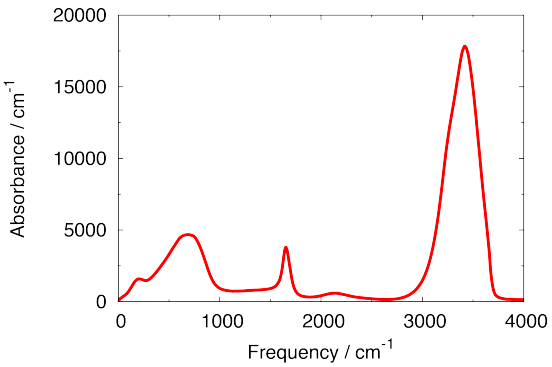

Figure 1.1: IR spectrum of liquid water at ambient temperature (Ref. 5).

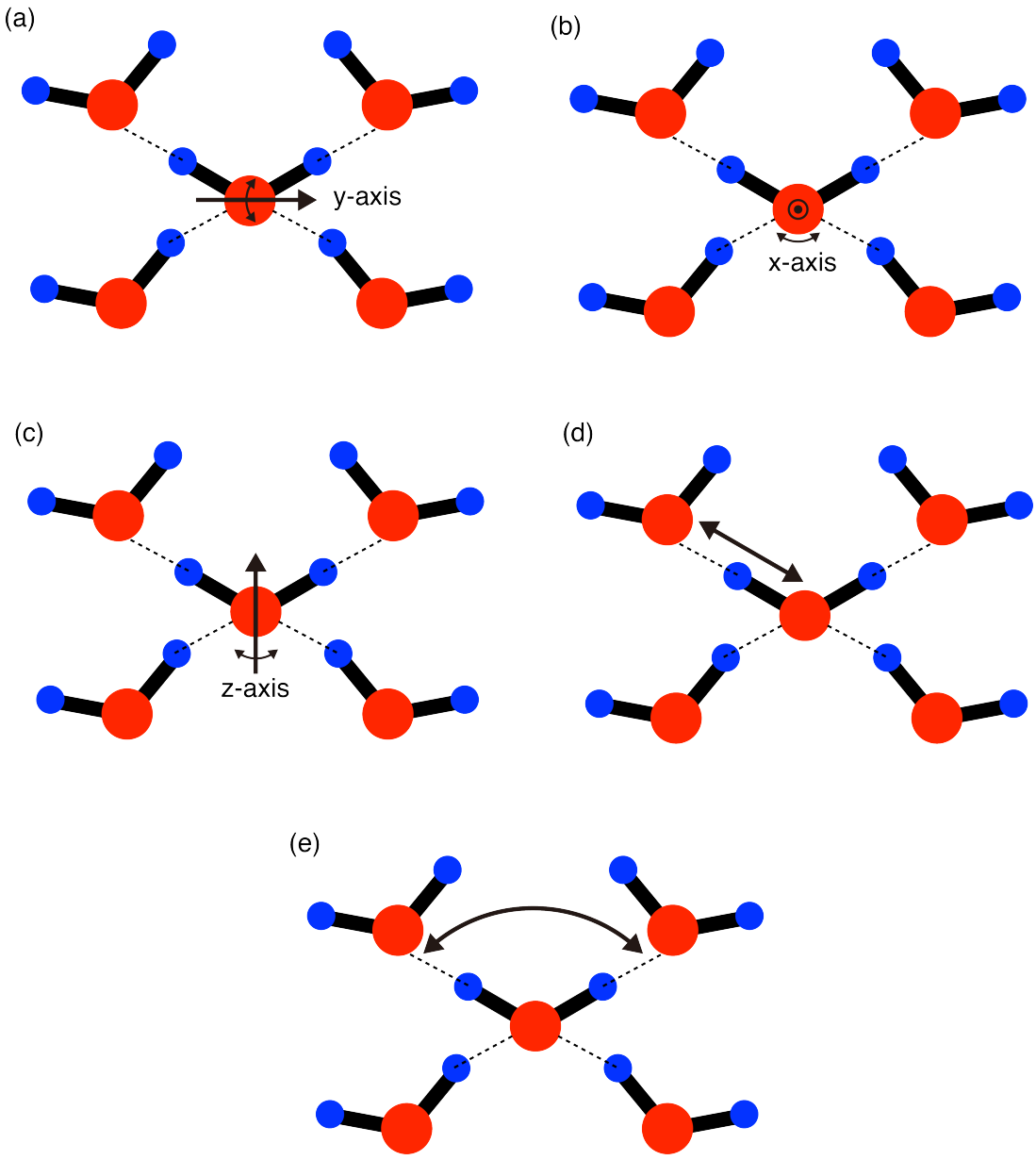

Figure 1.2: Schematics of intermolecular motions of liquid water. (a) libration around molecular y-axis, (b) libration around molecular x-axis, (c) libration around molecular z-axis, (d) HBs stretch, and (e) HBs bend.

Information obtained from linear spectroscopy is limited and, thus, the detailed dynamics of water cannot be fully resolved. The dynamics of water has been investigated by using third-order non-linear spectroscopy, e.g. two-dimensional (2D) and pump-probe spectra [6-11,17-24]. As shown in chapter 2, the 2D IR spectra are sensitive to the frequency fluctuation of a vibrational mode while the pump-probe spectra are sensitive to the energy relaxation of a vibrational mode. These nonlinear spectra of the OH stretch especially have provided new perspective on the local dynamics of HB. Figure 1.3 shows the 2D IR spectra of the OH stretch in liquid D_2O. The frequency correlation of the OH stretch in liquid D_2O shows a fast decay with a 60 fs time constant due to the librational motion, a recursion with a 130~180 fs time constant because of the HB stretch, and a slow decay with a ~1 ps time constant arising from the HB rearrangement [6,7]. In addition, the 2D IR spectra indicate the inhomogeneous frequency fluctuation of the OH stretch in liquid D_2O due to the difference of the HB strength [8]. As shown in Figure 1.4, the frequency fluctuation of the OH stretch in neat water is quite fast, less than 50 fs, due to strong inter- and intra-molecular couplings [10,11].

The frequency fluctuation of the OH stretch has also been investigating in theoretical studies [12-16]. The theoretical studies on the 2D IR spectra show that the frequency fluctuation of the OH stretch in liquid D_2O is correlated to the fluctuation of the electric field along the OH bond [12,13]. The theoretically calculated 2D IR spectra of the OH stretch in

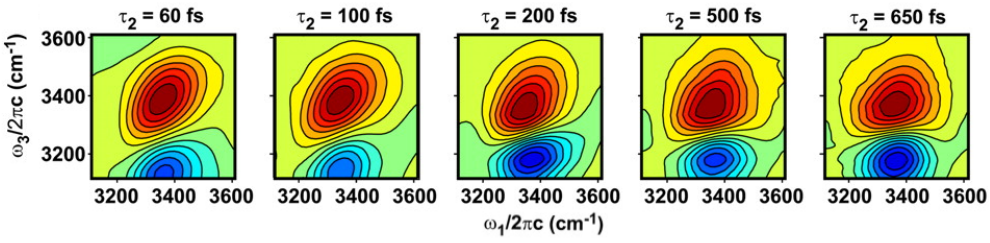

Figure 1.3: Experimental 2D IR spectra of the OH stretch in liquid D_2O. Figure reprinted with permission from Ref. 7. Copyright 2005 National Academy of Sciences.

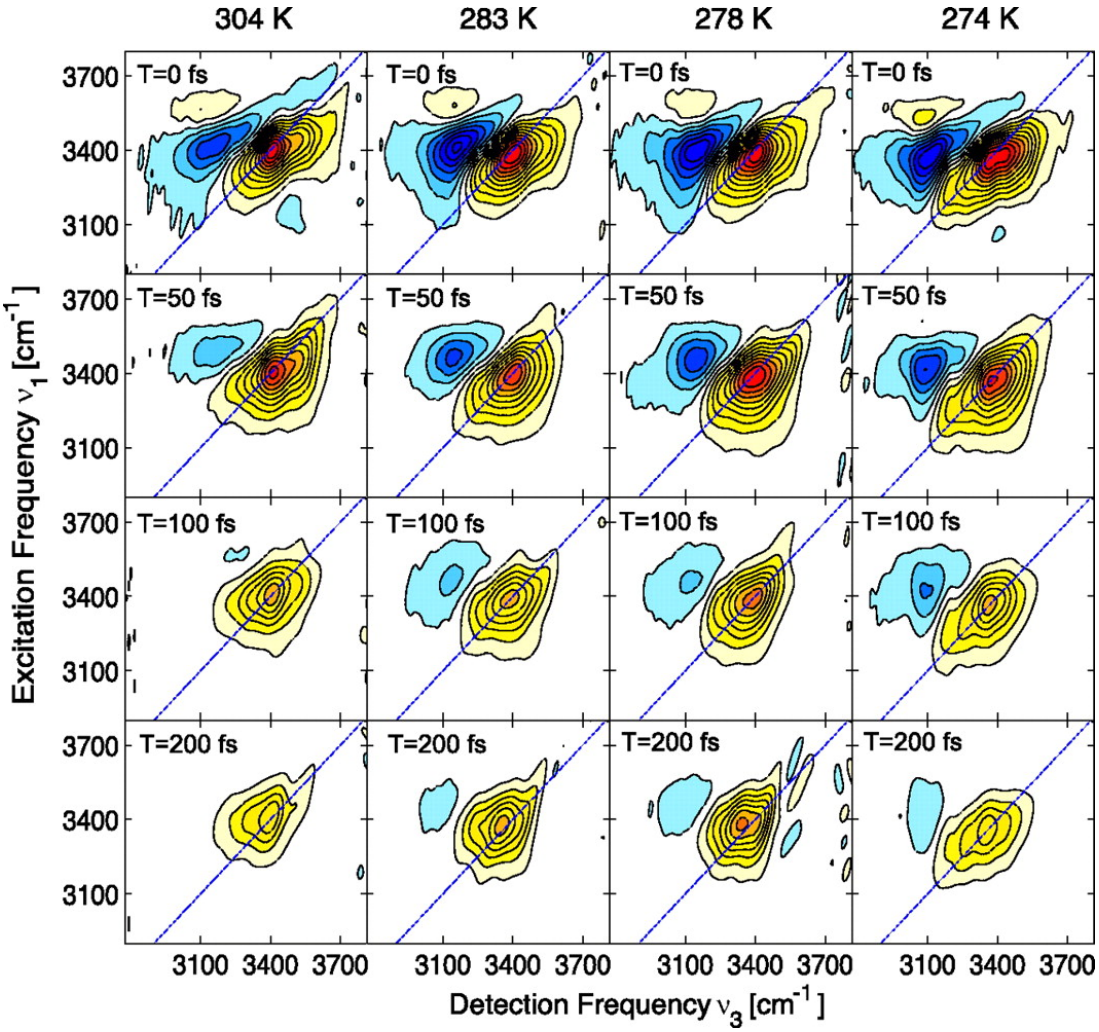

Figure 1.4: Temperature dependence of the 2D IR spectra of the OH stretch in liquid water. Figure reprinted with permission from Ref. 11. Copyright 2008 National Academy of Sciences.

liquid water by solving the Schrödinger equation for the OH stretch along the classical trajectories calculated from molecular dynamics (MD) simulations show that the intermolecular coupling between the OH stretching motions causes the fast spectral diffusion after 200 fs [14-16].

In addition to the frequency fluctuation, the energy relaxation dynamics of the OH stretch has been examined. The experimental pump-probe spectra of the OH stretch in

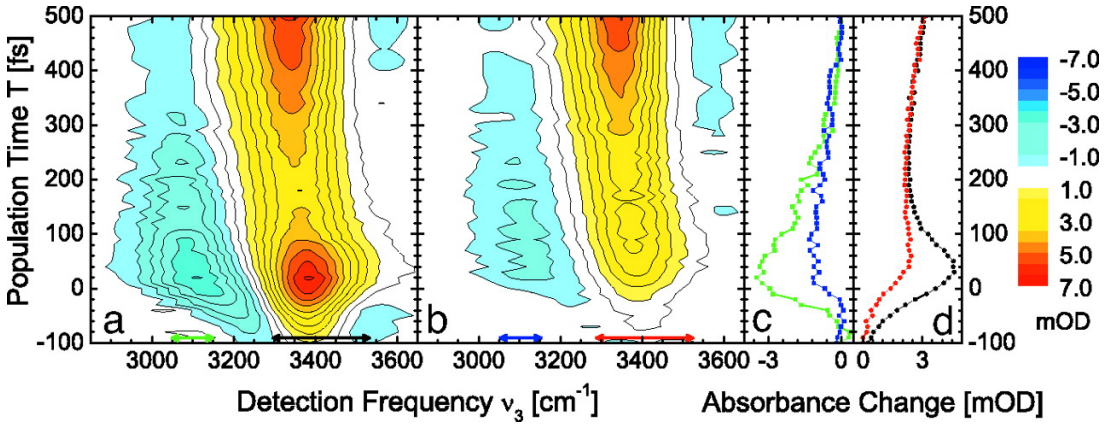

Figure 1.5: Pump-probe spectra of the OH stretch in liquid water. (a) parallel and (b) perpendicular polarizations. (c) Pump-probe cross-sections integrated between 3050-3150 cm^{-1} for parallel (green) and perpendicular (blue) polarizations. (d) Pump-probe cross-sections integrated between 3300-3600 cm^{-1} for parallel (black) and perpendicular (red) polarizations. Figure reprinted with permission from Ref. 11. Copyright 2008 National Academy of Sciences.

liquid water and heavy water are presented in figures 1.5 and 1.6, respectively. The vibrational energy of the OH stretch in liquid water and heavy water decays with the time constants of 270-300 fs [17-24] and 700 fs [6], respectively. It is believed that the ultrafast energy relaxation of the OH stretch in liquid water is due to the Fermi resonance between the OH stretch and the HOH bend as well as the strong nonlinear coupling between the OH stretch and intermolecular motions. However, the detail of the relaxation mechanism of the OH stretch in liquid water is still controversial [21-24].

The energy relaxation of the OH stretch has also been investigating in theoretical studies. Lawrence *et al.* investigated the relaxation time of the OH stretch in liquid D_2O by using the Landau-Teller theory and obtained the time constant of 2.3-2.7 ps [25,26]. Kandratsenka *et al.* analyzed the relaxation pathway and time constant of the OH stretch in liquid D_2O by

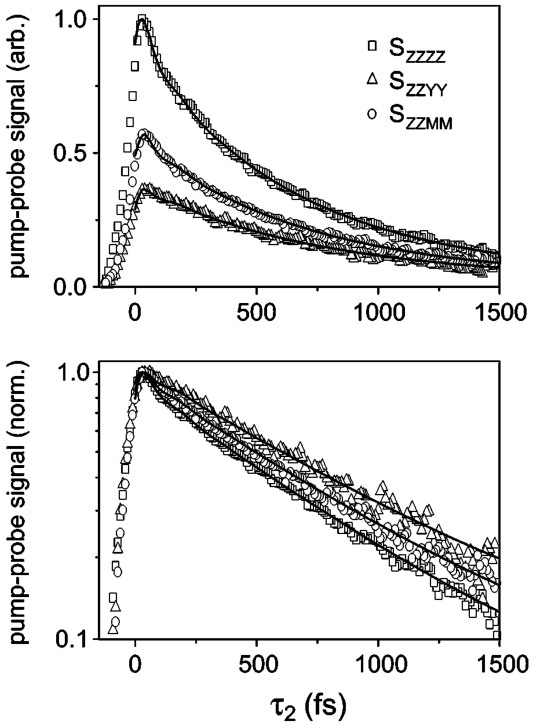

Figure 1.6: Pump-probe signals in parallel (squares), perpendicular (triangles), and magic angle polarization (circles) of the OH stretch in liquid D_2O. The bottom panel is a semilog plot. Figure reprinted with permission from Ref. 6. Copyright 2005 American Institute of Physics.

using non-equilibrium molecular dynamics simulations and found that the half of the excited energy of the OH stretch transfers to the HOD bend of the same molecule with a time constant of 2.7 ps [27].

Contrast to the OH stretch, the HOH bend has not been extensively studied. It is known from the experimental results that the IR spectrum of the HOH bend is also sensitive to the HB structure [28]. For example, the IR spectrum of the HOH bend in ice is weaker and broader than that of liquid water [29]. However, the molecular origin of the difference in the IR spectrum of ice and liquid water has not been revealed. The energy relaxation mechanism from the HOH bend to the intermolecular motions in liquid water has been

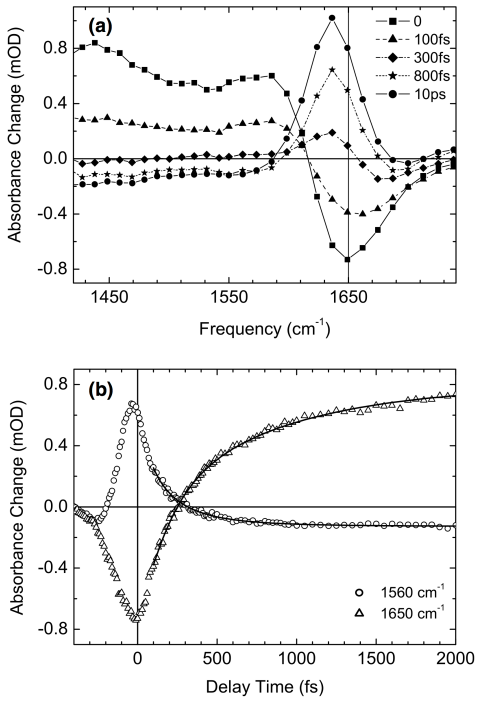

Figure 1.7: (a) Cross-section of the pump-probe spectrum of the HOH bend. (b) Pump-probe signals of (ω_{pump}, ω_{probe}) = (1650 cm^{-1}, 1650 cm^{-1})(triangles) and (ω_{pump}, ω_{probe}) = (1650 cm^{-1}, 1560 cm^{-1})(circles). Figure reprinted with permission from Ref. 30. Copyright 2005 Elsevier.

investigated with pump-probe spectroscopy by several groups [21-24,30,31]. Figure 1.7 shows pump-probe spectra of the HOH bend in liquid water. Elsaesser, Ashihara, and their co-workers found that the excited energy of the HOH bend quickly transfers to the motion between the librational motion and the HOH bend, i.e. 1000 - 1400 cm^{-1}, with a time constant of 170 fs [21,22,30,31]. Lindner *et al.* found that the lifetime of the HOH bend is 260 fs regardless whether the OH stretch or the HOH bend is excited [23,24].

The frequency fluctuation of the HOH bend has been investigated neither experimentally nor theoretically. In the all theoretical studies except for Yagasaki and Saito [32,33] and Hasegawa and Tanimura [34], the 2D IR spectra have been calculated by using the so-colled

'mapping-method', in which the relationship between the frequency of a mode and the electric field along the vibrational mode is used. However, the relationship between the HOH bend and the electric field or structural parameters, which is required to the mapping approach, has not been clarified. In addition to difficulty of the application of the mapping approach to the HOH bend, the structural and dynamical properties of the HOH bend cannot be well reproduced with conventional model potentials. For example, simple model potentials cannot reproduce the increase in the HOH angle in liquid water and the correct IR intensity of the HOH bend [35].

Xantheas and his co-worker showed that considering the intramolecular charge transfer is the essential to the correct description of the HOH bend [36]. The Thole-type model (TTM) potential family developed by Xantheas and his co-workers is the flexible, polarizable, and intramolecular charge transferable model for water and it can reproduce the correct HOH bend properties [37,38]. In addition, the intramolecular potential surface of the TTM family is based on the high level *ab initio* calculations [39].

The author theoretically investigated the static and dynamic properties of the OH stretch and the HOH bend in condensed phases in terms of linear and non-linear spectroscopy by using the TTM3-F potential which is the latest version of the TTM family [38]. The detail of the TTM3-F potential is described in Sec. 2.4. At first, the author investigated the difference between the IR spectra of the HOH bend in ice and liquid water by using MD simulations [40]. The calculated IR intensity of the HOH bend in ice is indeed weak compared with that in liquid water. The IR spectrum is expressed by the fluctuation of the dipole moment consisting of the permanent and induced dipole moments. The author analyzed the origin of the decrease in the IR intensity in ice by decomposing the spectrum into the contributions between the permanent and induced dipole moments. The author revealed that the decrease in the IR intensity of the HOH bend of the ice is due to the strong

anti-correlation between the permanent dipole moment of a molecule and the induced dipole moment of its neighboring molecules. In addition, the author showed that the anti-correlation becomes strong with the increase in the ordered HB structure, i.e. from liquid water to ice. This result indicates that the intensity of the IR spectrum of the HOH bend is sensitive to the local HB structure. In addition to the analysis of the HOH bend, the increase in the IR intensity of the OH stretch associated with the transition from liquid water to ice was studied. The author showed the permanent and induced dipole moments have a positive correlation for the OH stretch and this positive correlation is enhanced by the structured HB.

Then, the author investigated the frequency fluctuations of the OH stretch and the HOH bend in liquid water by calculating the 2D IR spectra [41]. The third-order response function, which is a key physical quantity of the 2D IR spectra, is directly calculated from non-equilibrium MD simulations. In present approach, different from the frequently used mapping method [14-16], both the inter-OH stretch coupling and the coupling between the OH stretch and the HOH bend are correctly considered in this calculation. The calculated 2D IR spectra of the OH stretch show that the frequency correlation of the OH stretch decays with the time constant of ~40 fs, the plateau from 60 to 100 fs, and the slow decay with time constant of ~180 fs. The calculated results are slower than the experimental results by Miller and his co-workers [11,12]. However, the more recent experimental result by Tokmakoff *et al.* is similar to the present result [42]. The author also analyzed that the frequency fluctuation of the HOH bend based on the calculated 2D IR spectra. It was found that the tilt-angle of the 2D IR spectra of HOH bend is small even at short waiting times, indicating ultrafast loss of the frequency correlation. The author found that the frequency fluctuation of the HOH bend also proceeds with three steps: the initial decay with the time constant of ~60 fs, the plateau from 100 to 150 fs, and the slow decay with the time constant of ~120 fs. The author elucidated that the ultrafast frequency fluctuation of the HOH bend is

due to the strong couplings with the intermolecular HB bend at 60 cm^{-1} as well as the OH stretch.

Finally, the author examined the energy relaxation of the OH stretch and the HOH bend in liquid water by calculating the pump-probe spectra which are also third-order nonlinear spectroscopy as the 2D IR spectra. The calculated relaxation time constants of the OH stretch and the HOH bend are 250 and 240 fs, respectively, which are in agreement with experimental results [11,12,17-24,30,31]. The detailed relaxation pathways from the OH stretch and the HOH bend have been examined in terms of the frequency-resolved transient kinetic energy analysis [41], in which the difference in the density of states between the excited state by an external field and the equilibrium state is examined. The author showed that the OH stretch is strongly coupled with the HOH bend and the intermolecular modes below ~1000cm^{-1}. The close investigation of the frequency-resolved transient kinetic energy analysis showed that the OH stretch more strongly coupled to the intermolecular HB stretch at 150 cm^{-1} than other motions. The HOH bend is coupled to the lower frequency motions, in particular strong nonlinear couplings between the librational and intermolecular HB bend motions. The strong couplings among all the motions cause the fast thermalization, i.e. the transition to the so-called 'hot ground state', with a time constant of ~1ps.

This thesis is organized as follow. In chapter 2, the author describes theoretical backgrounds on linear and nonlinear spectroscopy, basis of MD simulations, and the details of the TTM3-F potential. The analysis of the IR spectrum of the HOH bend in ice and liquid water is presented at chapter 3. The analysis of the frequency fluctuations of the OH stretch and the HOH bend is presented at chapter 4. The analysis of the energy relaxation from the OH stretch and the HOH bend to intermolecular motions is presented at chapter 5. The general conclusion is given in chapter 6.

References of chapter 1

[1] D. Eisenberg and W. Kauzmann, *The structure and properties of water*, Clarendon Press, 1969.

[2] I. Ohmine and H. Tanaka, Chem. Rev. **93**, 2545 (1993).

[3] I. Ohmine and S. Saito, Acc. Chem. Res. **32**, 741 (1999).

[4] T. Head-Gordon and G. Hura, Chem. Rev. **102**, 2651 (2002).

[5] J. E. Bertie and Z. Lan, Appl. Spectrosc. **50**, 1047 (1996).

[6] C. J. Fecko, J. J. Loparo, S. T. Roberts, and A. Tokmakoff, J. Chem. Phys. **122**, 054506 (2005)

[7] J. D. Eaves, J. J. Loparo, C. J. Fecko, S. T. Roberts, A. Tokmakoff, and P. L. Geissler, Proc. Natl. Acad. Sci. **102**, 13019 (2005).

[8] J. J. Loparo, S. T. Roberts, and A. Tokmakoff, J. Chem. Phys. **125**, 194522 (2006).

[9] J. B. Asbury, T. Steinel, K. Kwak, S. A. Corcelli, C. P. Lawrence, J. L. Skinner, and M. D. Fayer, J. Chem. Phys. **121**, 12431 (2004).

[10] M. L. Cowan, B. D. Bruner, N. Huse, J. R. Dwyer, B. Chugh, E. T. J. Nibbering, T. Elsaesser, and R. J. D. Miller, *Nature* **434**, 199 (2005).

[11] D.Kraemer, M. L. Cowan, A. Paarmann, N. Huse, E. T. J. Nibbering, T. Elsaesser, and R. J. D. Miller, Proc. Natl. Acad. Sci. **105**, 437 (2008).

[12] C. P. Lawrence and J. L. Skinner, J. Chem. Phys. **118**, 264 (2003).

[13] B. Auer, R. Kumar, J. R. Schmidt, and J. L. Skinner, Proc. Natl. Acad. Sci. **104**, 14215 (2007)

[14] A. Paarmann, T. Hayashi, S. Mukamel, and R. J. D. Miller, J. Chem. Phys. **128**, 191103 (2008).

[15] A. Paarmann, T. Hayashi, S. Mukamel, and R. J. D. Miller, J. Chem. Phys. **130**, 204110 (2009).

[16] T. L. C. Jansen, B. M. Auer, M. Yang, and J. L. Skinner, J. Chem. Phys. **132**, 224503 (2010).

[17] S. Woutersen, U. Emmerichs and H. J. Bakker, Science **278**, 658 (1997).

[18] S. Woutersen, U. Emmerichs, H. K. Nienhuys, and H. J. Bakker, Phys. Rev. Lett. **81**, 1106 (1998).

[19] S. Woutersen and H. J. Bakker, Nature **402**, 507 (1999).

[20] A. J. Lock, and H. J. Bakker, J. Chem. Phys. **117**, 1708 (2002).

[21] S. Ashihara, N. Huse, A. Espagne, E. T. J. Nibbering, and T. Elsaesser, J. Phys. Chem. A **111**, 743 (2007).

[22] S. Ashihara, N. Huse, A. Espagne, E. T. J. Nibbering, and T. Elsaesser, Chem. Phys. Lett. **424**, 66 (2006).

[23] J. Lindner, P. Vohringer, M. S. Pshenichnikov, D. Cringus, D. A. Wiersma, and M. Mostovoy, Chem. Phys. Lett. **421**, 329 (2006).

[24] J. Lindner, D. Cringus, M. S. Pshenichnikov, P. Vohringer, Chem. Phys. **341**, 326 (2007).

[25] C. P. Lawrence and J. L. Skinner, J. Chem. Phys. **117**, 5827 (2002).

[26] C. P. Lawrence and J. L. Skinner, J. Chem. Phys. **119**, 1623 (2003).

[27] A. Kandratsenka, J. Schroeder, D. Schwarzer, and V. S. Vikhrenko, J. Chem. Phys. **130**, 174507 (2009).

[28] J. E. Bertie, H. J. Labbe, and E. Whalley, J. Chem. Phys. **50**, 4501 (1969).

[29] B. Zelent, N. V. Nucci, and J. M. Vanderkooi, J. Phys. Chem. A **108**, 11141 (2004).

[30] N. Huse, S. Ashihara, E. T. J. Nibbering, and T. Elsaesser, Chem. Phys. Lett. **404**, 389 (2005)

[31] S. Ashihara, S. Fujioka, and K. Shibuya, Chem. Phys. Lett. **502**, 57 (2010).

[32] T. Yagasaki and S. Saito, J. Chem. Phys. **128**, 154521 (2008).

[33] T. Yagasaki, J. Ono, and S. Saito, J. Chem. Phys. **131**, 164511 (2009).

[34] T. Hasegawa and Y. Tanimura, J. Chem. Phys. **128**, 154521 (2008).

[35] J. Jeon, A. E. Lefohn, and G. A. Voth, J. Chem. Phys. **118**, 7504 (2003).

[36] G. S. Fanourgakis and S. S. Xantheas, J. Chem. Phys. **124**, 174504 (2006).

[37] C. J. Burnham and S. S. Xantheas, J. Chem. Phys. **116**, 5115 (2002).

[38] G. S. Fanourgakis and S. S. Xantheas, J. Chem. Phys. **128**, 074506 (2008).

[39] H. Partridge and D. W. Schwenke, J. Chem. Phys. **106**, 4618 (1997).

[40] S. Imoto, S. S. Xantheas, and S. Saito, J. Chem. Phys. **138**, 054506 (2013).

[41] S. Imoto, S. S. Xantheas, and S. Saito, J. Chem. Phys. **139**, 044503 (2013).

[42] K. Ramasesha, "Dynamics of Water and Aqueous Protons studied using Ultrafast Multi-dimensional Infrared Spectroscopy", Ph. D. thesis at the Massachusetts Institute of Technology (2013) (http://dspace.mit.edu/handle/1721.1/79257).

[43] T. Yagasaki and S. Saito, J. Chem. Phys. **134**, 184503 (2011).

Chapter 2

Theoretical background and computational method

2.1 Linear response function and IR spectroscopy

IR spectroscopy is a powerful tool to analyze the molecular interactions and dynamics. It measures the polarization per unit volume induced by an external infrared (IR) field. In this subsection, the author describes how the induced polarization of the system is expressed [1,2].

The system is assumed to be in an equilibrium state with temperature *T*. The density operator of the equilibrium state is given by

$$\rho_{\mathrm{eq}} = e^{-\beta H_0}/\mathrm{Tr}\{e^{-\beta H_0}\}, \tag{2.1}$$

where H_0 is the unperturbed Hamiltonian of the system and β is the inverse of the temperature. When an external force, $F(t)$, is applied to the system, the corresponding perturbed Hamiltonian is expressed as

$$H'(t) = -AF(t), \tag{2.2}$$

where A is the dynamical variable which couples to the external force. Thus, the total Hamiltonian, H(t), is given by

$$H(t) = H_0 + H'(t). \tag{2.3}$$

For simplicity, A is assumed to depend on only coordinates of the system, $A = A(\mathbf{q}(t))$, and $F(t)$ is the δ-function with respect to time, $F(t) = \delta(t)$.

The time evolution of the density matrix is described by the Liouville equation

$$\frac{\partial \rho}{\partial t} = -iL_0\rho(t) - iL'\rho(t) = -\frac{i}{\hbar}[H_0, \rho(t)] - \frac{i}{\hbar}[H', \rho(t)], \tag{2.4}$$

where L_0 and L' are the Liouville operators corresponding to the unperturbed and perturbed Hamiltonian, H_0 and H' in Eq. (2.3) and $\hbar$ is the Planck constant.

The time-dependent density matrix, $\rho(t)$, is assumed to be expressed as

$$\rho(t) = \rho_{\mathrm{eq}} + \rho_1(t) + \rho_2(t) + \cdots. \tag{2.5}$$

Substituting Eq. (2.5) into Eq. (2.4), we have

$$\frac{\partial \rho_{\mathrm{eq}}}{\partial t} + \frac{\partial \rho_1(t)}{\partial t} + \frac{\partial \rho_2(t)}{\partial t} + \cdots$$

$$= -\frac{i}{\hbar}\{[H_0, \rho_{\mathrm{eq}}] + [H'(t), \rho_{\mathrm{eq}}] + [H_0, \rho_1(t)] + [H'(t), \rho_1(t)] + \cdots\}. \tag{2.6}$$

The first-order solution in Eq. (2.6) satisfies the following equation,

$$\frac{\partial \rho_1(t)}{\partial t} = -\frac{i}{\hbar}[H'(t), \rho_{\mathrm{eq}}] - \frac{i}{\hbar}[H_0(t), \rho_1(t)]. \tag{2.7}$$

Integration of Eq. (2.7) yields

$$\rho_1(t) = -\frac{i}{\hbar}\int_{-\infty}^{t} d\tau e^{-iL_0(t-\tau)}[H'(\tau), \rho_{\mathrm{eq}}]. \tag{2.8}$$

By using Eq. (2.8), the first-order response of the dynamical variable A due to the perturbation is given by

$$\langle \Delta A(t) \rangle = \mathrm{tr}\{A\rho_1(t)\}$$

$$= \int_0^{\infty} dt' R^{(1)}(t') F(t - t'), \tag{2.9}$$

where $t' = t - \tau$ and $R^{(1)}(t)$ is the linear, i.e. first-order, response function expressed as

$$R^{(1)}(t) = -\frac{i}{\hbar}\mathrm{tr}\{A(t)[A(0), \rho_{\mathrm{eq}}]\}$$

$$= -\frac{i}{\hbar}\mathrm{tr}\{[A(t), A(0)]\rho_{\mathrm{eq}}\} = -\frac{i}{\hbar}\langle [A(t), A(0)] \rangle. \tag{2.10}$$

Here $\langle X \rangle$ indicates the expectation value of the operator X. Equation (2.10) shows that the linear response function is given by the expectation value of the commutation relation of $A(t)$ and $A(0)$.

The author is interested in the dynamics of many-body systems such as liquids. It is, however, impossible to compute the quantum mechanical response functions, Eq. (2.10), of a system with many degrees of freedom even with the state-of-the-art supercomputers. Thus, classical approximations has to be applied to calculate the response function. By using the relationship between the commutator and the Poisson bracket (PB),

$$-\frac{i}{\hbar}[A,B] \xrightarrow{\hbar\to 0} \sum_i \left(\frac{\partial A}{\partial q_i}\frac{\partial B}{\partial p_i} - \frac{\partial B}{\partial q_i}\frac{\partial A}{\partial p_i}\right)_{\mathrm{PB}}, \tag{2.11}$$

we have the following classical expression of the first-order response function,

$$R_{\mathrm{cl}}^{(1)}(t) = \beta \langle A(t) \sum_i \frac{\partial A(0)}{\partial q_i}\frac{\partial q_i}{\partial t}\rangle^{\mathrm{cl}} = \beta\langle A(t)\dot{A}(0)\rangle^{\mathrm{cl}}. \tag{2.12}$$

Here $\langle X\rangle^{\mathrm{cl}}$ indicates the classical ensemble average of the physical variable *X*. It is notable that the first-order response function is calculated by the correlation function of the variable *A* and the time derivative of the *A* in the equilibrium system.

The response function is obtained from non-equilibrium MD simulations. By using the following identity [3],

$$\frac{i}{\hbar}[A(t), \ \ ] \equiv iL_A(t) = \lim_{\epsilon\to 0}\frac{1}{\epsilon}\{\exp(i\epsilon L_A(t)) - 1\}, \tag{2.13}$$

the first-order response function can be recast by using Liouville operator

$$R^{(1)}(t) = \lim_{\epsilon\to 0}\frac{1}{\epsilon}\mathrm{tr}\{A(t_1)(\exp(i\epsilon L_A(0)) - 1)\rho_{\mathrm{eq}}\}. \tag{2.14}$$

By using the classical approximation for the time evolution, we obtain the following expression for the linear response function based on non-equilibrium approach,

$$R_{\mathrm{cl}}^{(1)}(t) \propto \langle A(t)\rangle_{\mathbf{0}}^{\mathrm{cl}} - \langle A(t)\rangle^{\mathrm{cl}}. \tag{2.15}$$

Here, the subscript of the first term in the right hand side denotes the time of the application

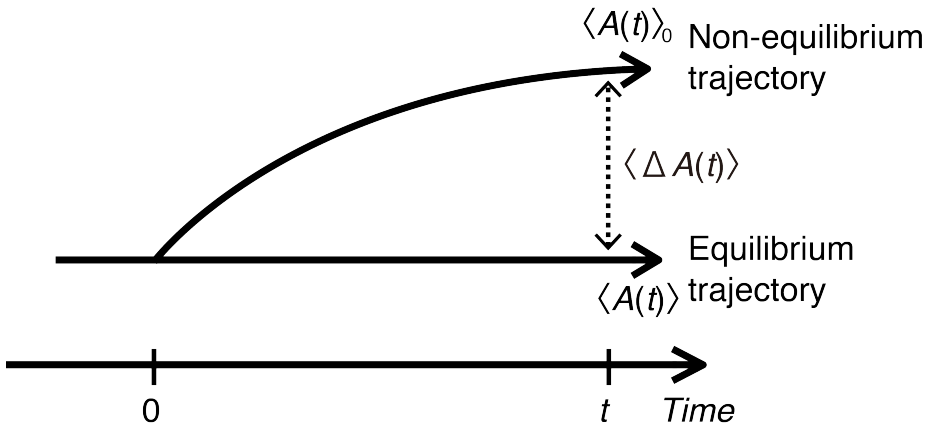

Figure 2.1: Schematic of computational procedure for Eq. (2.15.)

of the external force, i.e. the first term indicates the variable A at t in the presence of the external force at $t = 0$. The computational scheme for Eq. (2.15) is shown in Fig 2.1. To reduce the contamination of higher-order responses, the inversed force method can be used [4]

$$R_{\mathrm{cl}}^{(1)}(t) \propto \frac{1}{2}\left(\langle A(t)\rangle_0^{\mathrm{cl}} - \langle A(t)\rangle^{\mathrm{cl}}\right) - \frac{1}{2}\left(\langle A(t)\rangle_{\bar{0}}^{\mathrm{cl}} - \langle A(t)\rangle^{\mathrm{cl}}\right)$$

$$= \frac{1}{2}\left(\langle A(t)\rangle_0^{\mathrm{cl}} - \langle A(t)\rangle_{\bar{0}}^{\mathrm{cl}}\right), \tag{2.16}$$

where the over-bar on the subscript represents the opposite direction of the external force.

For IR spectroscopy, the perturbed Hamiltonian is expressed as

$$H'(t) = -ME(t)\,, \tag{2.17}$$

where M and $E(t)$ are the dipole operator of the system and the electric field, respectively, and, thus, the first-order IR response function is given as

$$R_{\mathrm{cl}}^{(1)}(t) = \beta\langle \dot{M}(0)M(t)\rangle. \tag{2.18}$$

The observable of the IR spectroscopy is the first-order induced polarization per volume. The IR spectrum is, therefore, expressed as

$$I(\omega) = \frac{4\pi^2\omega}{3Vc}\frac{1}{2\pi}\int dt\, R^{(1)}(t)e^{-i\omega t}dt$$

$$= \frac{4\pi^2\omega}{3V\hbar c}(1 - e^{-\beta\hbar\omega})\frac{1}{2\pi}\int\langle M(0)M(t)\rangle e^{-i\omega t}dt, \tag{2.19}$$

where c and V are the speed of light and the volume of the system, respectively. It should be noted that the correlation function in Eq. (2.19) is the quantum mechanical correlation function. Since any classical time correlation function is a real function, the spectrum calculated from a classical time correlation function does not satisfy the detailed balance condition. Various methods have been proposed for the correction of the detailed balance condition [5]. When the harmonic approximation is used for the correlation of the detailed balance condition, the IR spectrum is given by

$$I(\omega) = \frac{4\pi^2\beta\omega^2}{3Vc}\frac{1}{2\pi}\int\langle M(0)M(t)\rangle_{\mathrm{cl}}e^{-i\omega t}dt. \tag{2.20}$$

2.2 Third-order response function and third-order spectroscopy

In multidimensional spectroscopy, a system interacts with external fields at several times, e.g., three different times in two-dimensional (2D) IR spectroscopy. The above result of the linear response function can be generalized to the system interacting with multiple external fields [6]. The corresponding perturbed Hamiltonian is expressed as

$$H' = -\sum_{i=1}^{N} AF_i(t-\tau_i), \tag{2.21}$$

where N is the number of the external forces. Applying the similar procedure for the derivation of the linear response given by Eq. (2.9), the responses of the variable A, i.e. ΔA, to the two and three external forces are

$$\begin{aligned}\langle \Delta A(t)\rangle &= \mathrm{tr}\{A\rho_2(t)\} \\ &= \int_0^\infty dt' \int_0^\infty dt'' R^{(2)}(t',t'')F_2(t-t')F_1(t-t'-t''),\end{aligned} \tag{2.22}$$

$$\begin{aligned}\langle \Delta A(t)\rangle &= \mathrm{tr}\{A\rho_3(t)\} \\ &= \int_0^\infty dt' \int_0^\infty dt'' \int_0^\infty dt''' R^{(3)}(t',t'',t''')F_3(t-t')F_2(t-t'-t'')F_1(t-t'-t''-t'''),\end{aligned} \tag{2.23}$$

with the second- and third-order response functions which are expressed as

$$R^{(2)}(t_1,t_2) = \left(\frac{i}{\hbar}\right)^2 \mathrm{tr}\{A(t_1+t_2)[A(t_1),[A(0),\rho_{eq}]]\}, \tag{2.24}$$

$$R^{(3)}(t_1,t_2,t_3) = \left(\frac{i}{\hbar}\right)^3 \mathrm{tr}\{A(t_1+t_2+t_3)[A(t_1+t_2),[A(t_1),[A(0),\rho_{\mathrm{eq}}]]]\}. \tag{2.25}$$

2D IR and pump-probe spectra are categorized into third-order nonlinear spectroscopy and, thus, they can be expressed in terms of the third-order response function. As mentioned above, the calculation of the quantum mechanical response function is impossible for the system with many degrees of freedom. Hence, some classical approximation has to be employed.

When the relationship between the commutator and the Poisson bracket is used, the classical expressions of third-order response functions are [7,8]

$$R_{\mathrm{cl}}^{(3)}(t_1,t_2,t_3)=\beta\langle\dot{A}(0)\{\{A(t_1+t_2+t_3),A(t_1+t_2)\}_{\mathrm{PB}},A(t_1)\}_{\mathrm{PB}}\rangle^{\mathrm{cl}}, \tag{2.26}$$

$$=\beta\langle(\beta\dot{A}(0)\dot{A}(t_1)+\{\dot{A}(0),A(t_1)\}_{\mathrm{PB}})\{A(t_1+t_2+t_3),A(t_1+t_2)\}_{\mathrm{PB}}\rangle^{\mathrm{cl}}. \tag{2.27}$$

It should be noted that the Poisson bracket consisting of quantities at different times, $\{X(t),Y(0)\}_{\mathrm{PB}}$, is essential for the nonlinear response functions, Eqs. (2.26) and (2.27), though it is not required for the linear response function as seen in Eq. (2.12). When *X* and *Y* are the functions of coordinates, $\{X(t),Y(0)\}_{\mathrm{PB}}$ is given by

$$\{X(t),Y(0)\}_{\mathrm{PB}}=-\frac{\partial X(t)}{\partial\mathbf{p}(t)}\frac{\partial\mathbf{p}(t)}{\partial\mathbf{p}(0)}\frac{\partial Y(t)}{\partial\mathbf{q}(t)}. \tag{2.28}$$

The partial derivative matrix, $\partial\mathbf{p}(t)/\partial\mathbf{p}(0)$, represents the variation of momentum at *t* induced by a small change of momentum at $t=0$. This matrix is a sub-matrix of the so-called stability matrix, $\mathbf{J}(t)=\partial\gamma(t)/\partial\gamma(0)$, where $\gamma(t)=(\mathbf{q}(t),\mathbf{p}(t))$. The stability matrix represents the transformation of the phase space along the trajectory and plays an important role in nonlinear mechanics and semi-classical theory [9,10]. Thus, the nonlinear response functions defined by using $\{X(t),Y(0)\}_{\mathrm{PB}}$ are highly sensitive to the trajectory and provide more detailed information about dynamics than the linear response function [11].

By using the identity of Eq. (2.13), Eq. (2.25) can be rewritten in the form

$$R^{(3)}(t_1,t_2,t_3)=\lim_{\epsilon\to0}\frac{1}{\epsilon^2}\mathrm{tr}\{A(t_1+t_2+t_3)(\exp(i\epsilon L_A(t_1+t_2))-1)$$

$$(\exp(i\epsilon L_A(t_1))-1)\frac{i}{\hbar}[A(0),\rho_{\mathrm{eq}}]\}. \tag{2.29}$$

By applying the classical approximation for the Liouville equation and the commutation relation between $A(0)$ and ρ_{eq}, the third-order response function is expressed as [8,12,13]

$$R_{\mathrm{cl}}^{(3)}(t_1,t_2,t_3)\propto\langle\dot{A}(0)A(t_1+t_2+t_3)\rangle_{t_1,t_1+t_2}^{\mathrm{cl}}-\langle\dot{A}(0)A(t_1+t_2+t_3)\rangle_{t_1}^{\mathrm{cl}}$$

$$-\langle\dot{A}(0)A(t_1+t_2+t_3)\rangle_{t_1+t_2}^{\mathrm{cl}}+\langle\dot{A}(0)A(t_1+t_2+t_3)\rangle. \tag{2.30}$$

Using the inverse force method leads yields to

$$R_{\mathrm{cl}}^{(3)}(t_1,t_2,t_3)\propto\langle\dot{A}(0)A(t_1+t_2+t_3)\rangle_{t_1,t_1+t_2}^{\mathrm{cl}}+\langle\dot{A}(0)A(t_1+t_2+t_3)\rangle_{\overline{t_1,t_1+t_2}}^{\mathrm{cl}}$$

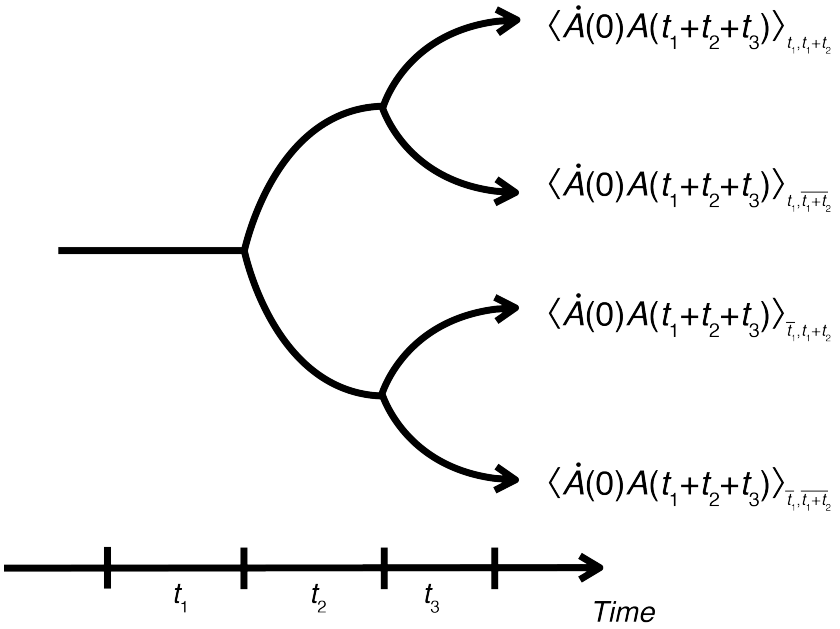

Figure 2.2: Schematic of computational procedure for Eq. (2.31).

$$-\langle \dot{A}(0)A(t_1+t_2+t_3)\rangle^{\mathrm{cl}}_{\overline{t_1},t_1+t_2} - \langle \dot{A}(0)A(t_1+t_2+t_3)\rangle^{\mathrm{cl}}_{t_1,\overline{t_1+t_2}}. \quad (2.31)$$

The computational scheme for Eq. (2.31) is shown in Fig 2.2. The third-order IR response function used in the present analysis is given as

$$R^{(3)}_{\mathrm{cl}}(t_1,t_2,t_3) \propto \langle \dot{M}(0)M(t_1+t_2+t_3)\rangle^{\mathrm{cl}}_{t_1,t_1+t_2} + \langle \dot{M}(0)M(t_1+t_2+t_3)\rangle^{\mathrm{cl}}_{\overline{t_1},\overline{t_1+t_2}}$$
$$-\langle \dot{M}(0)M(t_1+t_2+t_3)\rangle^{\mathrm{cl}}_{\overline{t_1},t_1+t_2} - \langle \dot{M}(0)M(t_1+t_2+t_3)\rangle^{\mathrm{cl}}_{t_1,\overline{t_1+t_2}}. \quad (2.32)$$

Third-order IR spectroscopy measures the third-order polarization, $P^{(3)}(\tau,T,t)$, expressed by the convolution of the third-order IR response function, $R^{(3)}(t_1,t_2,t_3)$, with the finite width electric field as [2],

$$P^{(3)}(\tau,T,t) = \int_0^\infty dt_3 \int_0^\infty dt_2 \int_0^\infty dt_1\, E(t_s-t_3,\{\tau_i\})E(t_s-t_3-t_2,\{\tau_i\})$$
$$\times E(t_s-t_3-t_2-t_1,\{\tau_i\})R^{(3)}(t_1,t_2,t_3), \quad (2.33)$$

where

$$E(t,\{\tau_i\}) = \sum_{i=1}^{3} \varepsilon_i(t-\tau_i)\exp\big(-i\omega_i(t-\tau_i)\big)\exp(-i\mathbf{k}_i\mathbf{r}_i) + \text{ c. c.}. \quad (2.34)$$

Here, τ_1, τ_2, and τ_3 are the times of the centers of pulses and the three time intervals are defined as $\tau = \tau_2 - \tau_1$, $T = \tau_3 - \tau_2$, and $t = t_s - \tau_3$. The ω_i, k_i, and $\varepsilon_i(t)$ are the carrier frequency, wave vector, and envelope function of the pulse i, respectively. Figure 2.3 presents a schematic of third-order IR spectroscopy. Equation (2.33) can be written as

$$P^{(3)}(\tau,T,t) = \sum_{\alpha=\mathrm{I}}^{\mathrm{IV}} \exp(-i\mathbf{k}_\alpha \mathbf{r}) P_\alpha^{(3)}(\tau,T,t) + \text{c. c.}, \tag{2.35}$$

where $P_{\mathrm{I}}^{(3)}$, $P_{\mathrm{II}}^{(3)}$, $P_{\mathrm{III}}^{(3)}$, and $P_{\mathrm{IV}}^{(3)}$ denote the third-order polarizations generated in the $\mathbf{k}_{\mathrm{I}} = -\mathbf{k}_1 + \mathbf{k}_2 + \mathbf{k}_3$, $\mathbf{k}_{\mathrm{II}} = \mathbf{k}_1 - \mathbf{k}_2 + \mathbf{k}_3$, $\mathbf{k}_{\mathrm{III}} = \mathbf{k}_1 + \mathbf{k}_2 - \mathbf{k}_3$, and $\mathbf{k}_{\mathrm{IV}} = \mathbf{k}_1 + \mathbf{k}_2 + \mathbf{k}_3$ phase matching conditions, respectively.

In 2D IR spectroscopy, the waiting-time dependence of the so-called 2D IR correlation spectra, hereafter the author calls it 2D IR spectra just for the simplicity, has been examined. The 2D IR spectrum is expressed using $P_{\mathrm{I}}^{(3)}(\tau,T,t)$ and $P_{\mathrm{II}}^{(3)}(\tau,T,t)$ as [14]

$$S(\omega_1,T,\omega_3) = \mathrm{Re}\int_0^\infty dt \int_0^\infty d\tau \exp(i(\omega_1\tau - \omega_3 t)) i P_{\mathrm{I}}^{(3)}(\tau,T,t) \tag{3.36}$$

$$+\mathrm{Re}\int_0^\infty dt \int_0^\infty d\tau \exp(i(\omega_1\tau + \omega_3 t)) i P_{\mathrm{II}}^{(3)}(\tau,T,t).$$

The 2D IR spectra are sensitive to the correlation of the two vibrational frequencies, ω_1 and ω_3, separated by the waiting time T. Examples for the 2D IR spectra of short and long waiting times are pictured in Fig. 2.4. When T is shorter than the time scale of the frequency fluctuation, the 2D IR spectra are elongated to the diagonal direction because of the strong

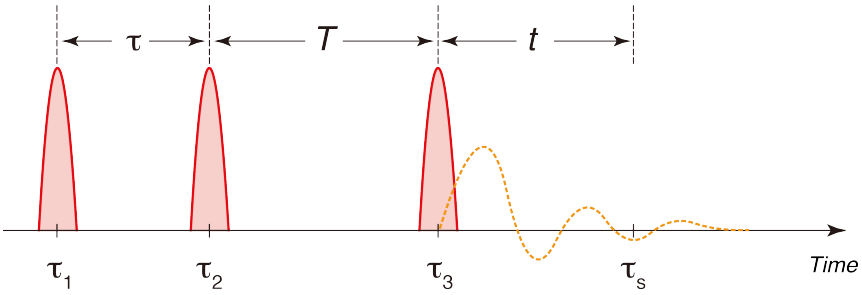

Figure 2.3: Schematic of third-order IR spectroscopy. Three pulses are applied to the system at τ_1, τ_2, and τ_3, and the signal is measured at τ_s.

correlation between ω_1 and ω_3 (Fig. 2.4(a)). In contrast, when T is longer than the time scale of the frequency fluctuation, the two frequencies lose their correlation and in that case the 2D IR spectra become parallel to ω_1 axis (Fig. 2.4(b)). That is, the slope of the 2D IR spectra is correlated to the extent of the initial inhomogeneity.

The energy relaxation processes in condensed phase are often investigated by using the pump-probe spectroscopy. In the pump-probe spectroscopy, the pump pulse makes the population state and, then, the absorption change induced by the pump pulse is measured by the probe pulse. The observable of the pump-probe spectroscopy, i.e. the spectrally integrated absorption change at the waiting time T, is given by [2]

$$\Delta\alpha(T) \propto \omega_{\mathrm{probe}} \mathrm{Im} \int dt\, E^{*}_{\mathrm{probe}}(t)(P^{(3)}_{\mathrm{I}}(0,T,t)+P^{(3)}_{\mathrm{II}}(0,T,t)). \qquad (2.37)$$

Here ω_{probe} and E_{peobe} are the frequency and electric field of the probe pulse. The energy relaxation processes are analyzed by the waiting time dependence of the change in the absorbance. Once $P^{(3)}_{\mathrm{I}}$ and $P^{(3)}_{\mathrm{II}}$ are calculated from Eqs. (2.33) and (2.35), the 2D IR spectra and pump-probe signals can be obtained from Eqs. (2.36) and (2.37), respectively.

2.3 Basis of molecular dynamics simulation

Molecular dynamics (MD) simulations are techniques for computing properties of many-body systems [15,16]. In particular, MD simulations provid detailed information on the static and dynamic properties of atoms and molecules [17]. The interactions between

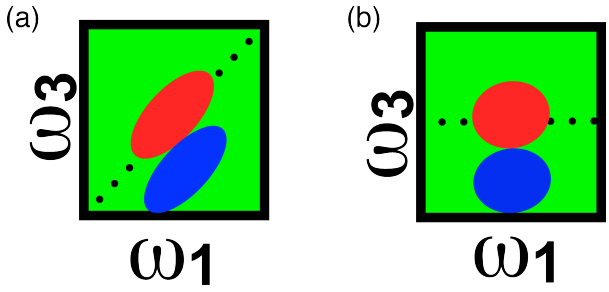

Figure 2.4: Examples of the 2D IR spectra of (a) short and (b) long waiting times.

particles, i.e. atoms and molecules, of the system are given by a model potential U and the Hamiltonian of the system is given as

$$H = \sum_i^N \frac{\mathbf{p_i}^2}{2m_i} + U(\mathbf{q}_1, \mathbf{q}_2, \cdots, \mathbf{q}_N), \tag{2.38}$$

where $\mathbf{q}_i$, $\mathbf{p}_i$, m_i are the Cartesian coordinate and momentum and mass of particle i, and N is a number of particles in the system. The equations of motion for the system are given by

$$\dot{\mathbf{q}}_i = \frac{\partial H}{\partial \mathbf{p}_i} = \frac{\mathbf{p}_i}{m_i},$$

$$\dot{\mathbf{p}}_i = -\frac{\partial H}{\partial \mathbf{q}_i} = -\frac{\partial U}{\partial \mathbf{q}_i} = \mathbf{F}_i, \tag{2.39}$$

where $\mathbf{F}_i$ is the force acting on particle i. The time evolution of the system from $T = 0$ to $T = t$ is describe as follow

$$\begin{pmatrix} \mathbf{p}(t) \\ \mathbf{q}(t) \end{pmatrix} = \exp(iLt) \begin{pmatrix} \mathbf{p}(0) \\ \mathbf{q}(0) \end{pmatrix}, \tag{2.40}$$

where L is the Liouville operator, $iL \equiv \sum_i \left\{ \frac{\partial H}{\partial p_i}\frac{\partial}{\partial q_i} - \frac{\partial H}{\partial q_i}\frac{\partial}{\partial p_i} \right\}$. The Liouville operator can be written as a sum of two contributions

$$iL = iL_1 + iL_2, \tag{2.41}$$

where

$$iL_1 = \sum_i \frac{\partial H}{\partial p_i}\frac{\partial}{\partial q_i} = \sum_i \frac{p_i}{m_i}\frac{\partial}{\partial q_i}, \tag{2.42}$$

$$iL_2 = -\sum_i \frac{\partial H}{\partial q_i}\frac{\partial}{\partial p_i} = \sum_i F_i \frac{\partial}{\partial p_i}. \tag{2.43}$$

Since iL_1 and iL_2 do not commute, the propagator $\exp(iLt) = \exp(i(L_1 + L_2)t)$ cannot be separated into a simple product, $\exp(iL_1 t)\exp(iL_2 t)$. By using the symmetric Trotter theorem, the propagator can be recast into form of

$$\exp(i(L_1 + L_2)t) = \lim_{P\to\infty}[\exp(iL_2 t/(2P))\exp(iL_1 t/P)\exp(iL_2 t/(2P))]^P. \tag{2.44}$$

Equation (2.44) indicates that the propagator can be approximated by a product of $\exp(iL_1 t/P)$ and $\exp(iL_2 t/(2P))$. Thus, using Eq. (2.44) truncated at $P = 1$, the propagator from $T = 0$ to $T = t$ is described as follow

$$\begin{pmatrix}\mathbf{p}(t)\\ \mathbf{q}(t)\end{pmatrix} \approx \exp\left(\frac{t}{2}\sum_i F_i \frac{\partial}{\partial p_i}\right) \exp\left(t\sum_i \frac{p_i}{m}\frac{\partial}{\partial q_i}\right) \exp\left(\frac{t}{2}\sum_i F_i \frac{\partial}{\partial p_i}\right) \begin{pmatrix}\mathbf{p}(0)\\ \mathbf{q}(0)\end{pmatrix}. \quad (2.45)$$

This method is called velocity-Verlet method. The integrator can be implemented as a three-step procedure:

$$\mathbf{p}_i(t/2) = \mathbf{p}_i(0) + t/2\mathbf{F}_i(\mathbf{q}(0))$$

$$\mathbf{q}_i(t) = \mathbf{q}_i(0) + t/m_i\mathbf{p}_i(t/2)$$

$$\mathbf{p}_i(t) = \mathbf{p}_i(t/2) + t/2\mathbf{F}_i(\mathbf{q}(t)) \quad (2.46)$$

The error of this method is proportional to $O(t^3)$.

2.4 TTM3-F potential

The accurate model potential is essential for MD simulations and theoretical calculations of linear and nonlinear spectra. In the present thesis, the author has employed the TTM3-F potential developed by Fanourgakis and Xantheas [18]. The TTM3-F potential is a flexible, polarizable, and intramolecular charge transferable potential and it reproduces the intramolecular dynamics of liquid water correctly. The intramolecular potential energy surface and intramolecular charge transfer scheme of the TTM3-F potential are based on the high level *ab initio* calculation of the gas phase water monomer [19].

The intramolecular potential energy surface is given by

$$U(r_1, r_2, \theta) = U^a(r_1) + U^a(r_2) + U^b(r_{\mathrm{HH}}) + U^c(r_1, r_2, \theta), \quad (2.47)$$

where the r_i are the OH bond length, r_{HH} is the HH distance, and θ is the HOH angle,

$$U^a(r) = D(1 - e^{-a(r-r_0)})^2, \quad (2.48)$$

$$U^b(r) = Ae^{-br}, \quad (2.49)$$

$$U^c(r_1, r_2, \theta) = c_{000} + \exp\{-\beta[(r_1 - r_e)^2 + (r_2 - r_e)^2]\} \times \sum_{ijk} c_{ijk}[(r_1 - r_e)/r_e]^i[(r_2 - r_e)/r_e]^j[\cos(\theta) - \cos(\theta_e)]^k. \quad (2.50)$$

Here, the parameters D, a, r_0, A, b, r_e, β, θ_e, and c_{ijk} were determined by performing a weighted least square fit to the *ab initio* data [19].

The point charges on atomic sites (H_1, H_2, O) are given by [18,19]

$$q_{H_1} = q(r_1, r_2, \theta),$$

$$q_{H_2} = q(r_2, r_1, \theta),$$

$$q_O = -(q_{H_1} + q_{H_2}), \tag{2.51}$$

where

$$\begin{aligned} q(r_1, r_2, \theta) = {} & A({r_1}^{-b} + {r_2}^{-b})[c_0 + c_1 P_1(\cos(\theta)) + c_2 P_2(\cos(\theta))] \\ & + \{c_{000} + \exp\{-\beta[(r_1 - r_e)^2 + (r_2 - r_e)^2]\}\} \\ & \times \sum_{ijk} c_{ijk}[(r_1 - r_e)/r_e]^i [(r_2 - r_e)/r_e]^j [\cos(\theta) - \cos(\theta_e)]^k \\ & + d_r(r_1 - r_e) + d_\theta(\theta - \theta_e). \end{aligned} \tag{2.52}$$

Here, P_l is l-the order Legendre polynomial, c_0, c_1, c_2, and c_{ijk} were determined by a least square fit to the *ab initio* data [19] using the function with $i + j + k \leq 6$, and d_r and d_θ are related to the correction of the dipole moment in liquid water. It is noted that q is not symmetric with respect to interchanging r_1 and r_2.

The intermolecular interaction is described by electrostatic and van der Waals (vdW) interactions. An additional site (M-site) carries the negative charge instead of the oxygen atom. Employing the M-site and effective charges, $(\tilde{q}_{H_1}, \tilde{q}_{H_2}, \tilde{q}_M)$, improves the quadrupole of the water molecule, whereas the dipole moment of water molecules is conserved. The position vector of the M-site is given by

$$\mathbf{r}_\mathrm{M} = (1 - \gamma)\mathbf{r}_\mathrm{O} + \frac{\gamma}{2}(\mathbf{r}_{\mathrm{H}_1} + \mathbf{r}_{\mathrm{H}_2}), \tag{2.53}$$

where γ is a constant. The effective charges are given by

$$\tilde{q}_{H_1} = q_{H_1} - \frac{\gamma}{2(1-\gamma)} q_O,$$

$$\tilde{q}_{H_2} = q_{H_2} - \frac{\gamma}{2(1-\gamma)} q_O,$$

$$\tilde{q}_M = -(\tilde{q}_{H_1} + \tilde{q}_{H_2}). \tag{2.54}$$

The M-site also carries the isotropic point dipole moment which is induced by the electric field around the water molecule. Thole's method is employed for the treatment of the

electrostatic interaction, i.e. charge-charge, charge-dipole, and dipole-dipole interactions [20]. According to this scheme, an effective density replaces the interactions between point charges/dipoles. The density $\rho(r)$ is expressed as

$$\rho(r) = \frac{1}{\tilde{A}^3}\frac{3a_s}{4\pi}\exp\left(-a_s\left(\frac{r}{\tilde{A}}\right)^3\right), \tag{2.55}$$

where a_s and $\tilde{A}$ are the parameters related to the polarizability of molecules. The vdW interaction acting between the oxygen atoms is described by the Buckingham exponential-six potential,

$$U(r) = \frac{\epsilon}{1-6/\lambda}\left\{\frac{6}{\lambda}\exp\left(\lambda\left[1-\frac{r}{\sigma}\right]\right)-\left(\frac{\sigma}{r}\right)^6\right\}. \tag{2.56}$$

References of chapter 2

[1] R. Kubo, M. Toda, and N. Hashitsume, "Statistical Physics II", Springer (1985).

[2] S. Mukamel, "Principles of nonlinear optical spectroscopy", Oxford, (1999).

[3] S. Mukamel and J. B. Maddox, J. Chem. Phys. **121**, 36 (2004).

[4] T. L. C. Jansen, K. Duppen, and J. G. Snjiders, Phys. Rev. B **67**, 134206 (2003).

[5] S. A. Egorov, K. F. Everitt, and J. L. Skinner, J. Phys. Chem. A **103**, 9494 (1999).

[6] Y. Tanimura, J. Phys. Soc. Jpn. **75**, 080021 (2006).

[7] T. Hasegawa and Y. Tanimura, J. Chem. Phys. **128**, 154521 (2008).

[8] T. Yagasaki, J. Ono, and S. Saito, J. Chem. Phys. **131**, 164511 (2009).

[9] W. H. Miller, J. Chem. Phys. **53**, 3578 (1970).

[10] X. Sun and W. H. Miller, J. Chem. Phys. **110**, 6635 (1999).

[11] S. Saito and I. Ohmine, J. Chem. Phys. **119**, 9073 (2003).

[12] T. Hasegawa and Y. Tanimura, J. Chem. Phys. **125**, 074512 (2006).

[13] T. Yagasaki and S. Saito, J. Chem. Phys. **128**, 154521 (2008).

[14] M. Khalil, N. Demirdöven, and A. Tokmakoff, Phys. Rev. Lett. **90**, 47401 (2003).

[15] M. P. Allen and D. J. Tildesly, *Computer Simulation of Liquids*, Oxford University Press, 1991.

[16] D. Frenkel and B. Smit, *Understanding Molecular Simulation: from Algorithms to Applications*, Academic Press, 2001.

[17] M. E. Tuckerman, *Statistical Mechanics: Theory and Molecular Simulation*, Oxford University Press, 2010.

[18] G. S. Fanourgakis and S. S. Xantheas, J. Chem. Phys. **128**, 074506 (2008).

[19] H. Partridge and D. W. Schwenke, J. Chem. Phys. **106**, 4618 (1997).

[20] B. T. Thole, Chem. Phys. **59**, 341 (1981).

Chapter 3

Difference in the HOH bend of the IR spectra between liquid water and ice*

3.1 Introduction

Water is the most abundant liquid on earth and has several anomalous thermodynamic and dynamical properties,[1] many of which have been attributed to its fleeting three-dimensional hydrogen bond (HB) network [2]. There are many experimental and theoretical studies on the HB in water. For example, the Infrared (IR) spectrum of liquid water has been extensively studied because it is sensitive to the underlying HB structures [3-5]. The IR spectrum of liquid water consists of the intermolecular motions between 0 and 1000 cm^{-1}, a band centered at 1600 cm^{-1} due to the HOH bend and a broad band between 3000 and 4000 cm^{-1} corresponding to the OH stretching vibrations. It is well known that both the frequency and the intensity of the OH stretching vibrations are sensitive to the local HB environment. Strong HBs result in red-shifted transition frequencies, as is the case, for instance, for the OH stretching vibrations in ice when compared to liquid water. The dynamics of the OH stretch have been studied using ultrafast nonlinear spectroscopy, e.g. two dimensional (2D) IR spectroscopy. The 2D IR spectra revealed that the frequency correlation of the OH stretch in liquid D_2O and the OD stretch in liquid H_2O are associated with a rapid sub 100 fs decay, an underdamped oscillation of 130 fs induced by HB stretch, and a slow decay with the time constant of approximately 1 ps [6-9]. The 2D IR spectra of the OH stretch in neat water display a loss of frequency correlation on a 50 fs time scale and that of neat ice display a sub 100 fs time scale randomization of the transition dipole [10, 11].

It is known that the bend mode in the IR spectrum of liquid water shows a red-shift with increasing temperature, i.e. the temperature-dependence of the IR spectrum of the HOH bend is opposite to that of the OH stretch [4]. In addition, the IR spectrum of the HOH bend of

* S. Imoto, S. S. Xantheas, and S. Saito, "Molecular origin of the difference in the HOH bend of the IR spectra between liquid water and ice", J. Chem. Phys. **138**, 054506 (2013)

ice is weaker and broader than that of liquid water [12]. The time scale of the energy relaxation of the HOH bend in neat liquid water and aqueous solution of ions at room temperature has been measured by using pump-probe experiments [13-16]. The vibrational relaxation of the HOD bend in liquid D_2O has been also experimentally studied [17]. The details of the fluctuation and dynamics of the HOH bend are, however, not well understood.

Theoretical studies of the HOH bend have also been limited. However, the energy relaxation dynamics of the HOH bend have been theoretically examined recently. Hynes and co-workers revealed the time scale and pathway of the HOH bend relaxation by using the classical non-equilibrium MD simulations [18, 19]. Miguel and co-workers investigated the quantum effects on the energy relaxation of the HOH bend and the HOD bend by using the quantum/classical hybrid MD simulations [20, 21]. Kandratsenka and co-workers showed the energy relaxation pathway of the OD stretch in D_2O via the HOD bend employing the classical non-equilibrium MD simulations [22]. The scarcity of the theoretical studies can be in part attributed to the fact that the value of the average HOH angle of the water molecule in ice and liquid water decreases when simple model potentials are used, a qualitative difference from the results of experimental studies and first principles simulations [23-28]. It is also known that the IR intensity of the HOH bend is overestimated by simple interaction potentials for water.

This is not, however, the case for the Thole-type models (TTM), previously introduced by Xantheas and co-workers, who showed that the intramolecular charge transfer is essential for reproducing the experimentally observed increase of the HOH angle in the condensed phase with respect to the monomer [29]. When this intramolecular charge transfer was "turned off", the HOH bend in ice and liquid water was smaller than the monomer value, like in all previous fixed charge models. The flexible, polarizable transferable model TTM2.1-F [30], which uses the *ab initio*-based dipole moment surface of the gas phase monomer, was

shown to properly describe both the increase and associated IR intensity of the HOH bend in the condensed phase [29, 30]. The latest version 3.0 of the TTM family of potentials (TTM3-F) [31], was shown to reproduce the IR spectra [31-34] and other properties of the liquid [31, 35-37] more accurately.

In this study, the author used the TTM3-F water model potential to analyze obtain molecular level insight into the difference between in the IR peak band structure of the HOH bend of between ice and liquid water. The present chapter is organized as follows. The theoretical background is outlined in Section 3.2. The details of classical MD simulations and subsequent analysis for the clusters via *ab initio* electronic structure calculations are described in Section 3.3. The results are presented and discussed in Section 3.4 with final conclusions drawn in Section 3.5.

3.2 Computational methods

The IR spectrum is related to the fluctuation of the total dipole moment of the system. When the harmonic quantum correction is applied to the classical IR spectra to satisfy the detailed balance condition, the IR spectrum is expressed as

$$I(\omega) = \frac{4\pi\omega^2}{3Vck_BT} \cdot \frac{1}{2\pi} \int dt\, e^{-i\omega t} \langle \delta\mathbf{M}(t)\delta\mathbf{M}(0)\rangle. \quad (3.1)$$

Here V, T, and $\delta\mathbf{M}$ are the volume, temperature, and fluctuation of total dipole moment of the system, c is the speed of light, and k_B is the Boltzmann constant. The total dipole moment is expressed as the sum of the permanent and interaction induced dipole moments,

$$\mathbf{M} = \mathbf{M}^{\mathrm{perm}} + \mathbf{M}^{\mathrm{ind}}. \quad (3.2)$$

$\mathbf{M}^{\mathrm{perm}}$ and $\mathbf{M}^{\mathrm{ind}}$ for MD simulations and *ab initio* calculations are defined later. Thus, the IR spectrum is the contribution of three terms, viz.,

$$I(\omega) = I^{\mathrm{perm}}(\omega) + I^{\mathrm{ind}}(\omega) + I^{\mathrm{cross}}(\omega)$$
$$\propto \int dt e^{-i\omega t} \langle \delta\mathbf{M}^{\mathrm{perm}}(t)\delta\mathbf{M}^{\mathrm{perm}}(0)\rangle \quad (3.3)$$

$$+ \int dt e^{-i\omega t} \langle \delta \mathbf{M}^{\mathrm{ind}}(t) \delta \mathbf{M}^{\mathrm{ind}}(0) \rangle$$

$$+ \int dt e^{-i\omega t} \langle \delta \mathbf{M}^{\mathrm{perm}}(t) \delta \mathbf{M}^{\mathrm{ind}}(0) + \delta \mathbf{M}^{\mathrm{ind}}(t) \delta \mathbf{M}^{\mathrm{perm}}(0) \rangle.$$

Hereafter the author will refer to these three terms in the right-hand side of eq. (3.3) as the *permanent*, *induced* and *cross terms*, respectively.

The instantaneous normal mode approach when employed to obtain $\mathbf{M}(t)$ via the lowest-order expansion yields [38]

$$\mathbf{M}(t) = \mathbf{M}(0) + \sum_\alpha \left. \frac{\partial \mathbf{M}}{\partial Q_\alpha} \right|_{t=0} Q_\alpha(t), \tag{3.4}$$

where $Q_\alpha(t)$ is normal mode α given by

$$Q_\alpha(t) = Q_\alpha(0) \cos(\omega_\alpha t) + \frac{V_\alpha(0)}{\omega_\alpha} \sin(\omega_\alpha t). \tag{3.5}$$

Here $V_\alpha(0)$ is the initial velocity of normal mode α. By substituting eq. (3.4) into eq. (3.1), the IR spectrum is expressed as

$$I(\omega) = \frac{2}{3Vc} \langle \sum_\alpha \left| \frac{\partial \mathbf{M}}{\partial Q_\alpha} \right|^2 \delta(\omega - \omega_0) \rangle. \tag{3.6}$$

The angle bracket represents averaging over the thermal distribution of ice or liquid water configurations. As a result, the permanent, induced, and cross terms in the normal mode approximation are given by

$$I^{\mathrm{perm}}(\omega) \propto \langle \sum_\alpha \left| \frac{\partial \mathbf{M}^{\mathrm{perm}}}{\partial Q_\alpha} \right|^2 \delta(\omega - \omega_\alpha) \rangle, \tag{3.7}$$

$$I^{\mathrm{ind}}(\omega) \propto \langle \sum_\alpha \left| \frac{\partial \mathbf{M}^{\mathrm{ind}}}{\partial Q_\alpha} \right|^2 \delta(\omega - \omega_\alpha) \rangle, \tag{3.8}$$

$$I^{\mathrm{cross}}(\omega) \propto 2 \langle \sum_\alpha \frac{\partial \mathbf{M}^{\mathrm{perm}}}{\partial Q_\alpha} \cdot \frac{\partial \mathbf{M}^{\mathrm{ind}}}{\partial Q_\alpha} \delta(\omega - \omega_\alpha) \rangle. \tag{3.9}$$

3.3 Computational details

a. Molecular Dynamics and Normal Mode Analysis

The author used the TTM3-F interaction potential, which is a transferable, flexible, polarizable model to describe the intra- and inter-molecular interactions in liquid water and

ice [31]. The author briefly accounts for some of its salient features here. The intramolecular interaction and charge transfer schemes of the TTM3-F potential are based on the high level *ab initio* gas phase water monomer potential and dipole moment surface of Partridge and Schwenke [39]. As regards the intermolecular interaction, the TTM3-F potential has four interaction sites. The Oxygen-Oxygen interaction is described by a Buckingham exponential-6 potential. A positive charge is placed on each hydrogen atom and a negative charge and an isotropic point dipole moment are placed on the M site located on the bisector of the HOH angle. The Thole type damping function is employed for the treatment of the electrostatic interactions [40]. In the analysis with the TTM3-F potential, the permanent and induced dipole moments are defined as the dipole moment originating from the point charges and the point dipole moment, respectively.

The author carried out classical MD simulations of periodic supercells of liquid water and ice Ih under the constant volume and energy conditions [41]. The MD simulations of liquid water were carried out at a temperature of 300 K using a supercell of 125 water molecules with dimensions $L_x \times L_y \times L_z = 15.5 \times 15.5 \times 15.5$ Å^3 and a density of 1.0 g/cm³. The resultant dielectric constant calculated with the TTM3-F potential of is 67.7. The author averaged the results over eight trajectories, each of which had a length of 500 ps. The MD simulations of ice Ih were performed at a temperature of 230K with a rectangular supercell of 96 molecules with dimensions $L_x \times L_y \times L_z = 13.5 \times 15.6 \times 14.7$ Å^3 containing $3 \times 2 \times 2$ unit cells and a density of 0.92 g/cm³. The analysis of the results for ice was performed over a hundred trajectories, which started from different initial configurations. The length of each trajectory for the ice simulations was 50 ps. For both the liquid water and ice simulations periodic boundary conditions were employed and the long-range electric interactions were calculated by using the Ewald sum. Equations of motion were integrated using the velocity-Velret algorithm with the time step of 0.05 fs. The induced dipole moment was

obtained iteratively at each step.

Normal modes for ice and liquid water were obtained using configurations taken from the MD trajectories. The author used a total of 300 and 200 configurations for ice and liquid water, respectively. The author also performed normal mode analysis for ~3,000 pentamer clusters randomly selected from the MD trajectories of liquid water and ice.

b. *Ab-initio* calculations

The total dipole moment of each molecule in a pentamer cluster was calculated using the distributed multipole analysis (DMA), in which the *n*-th multipole expansion is obtained via spherical harmonics [42]. The advantage of using DMA is that both the out of plane and in-plane components of the induced dipole moments can be reproduced. The author defined the total dipole moment of each molecule as a sum of the dipole moment calculated from the point charges and point dipoles. The author also defined the permanent and induced dipole moments of each molecule as the dipole moment of the water molecule given by Partridge and Schwenke in Ref. [39] and the difference between the total dipole moment and the permanent dipole moment, respectively. The DMA was carried out using GDMA 2.2 program [43]. All *ab initi*o calculations for the pentamer clusters extracted from the MD trajectories generated with the TTM3-F potential, were carried out at the MP2 level of theory with the aug-cc-pVDZ basis set [44] using the Gaussian09 package [45]. The positions of only the hydrogen atoms of the central molecules in each pentamer cluster were optimized. Overall we performed MP2/aug-cc-pVDZ calculations on ~600 configurations for both ice and liquid water. The dipole derivatives were evaluated by using a 4-point differentiation formula.

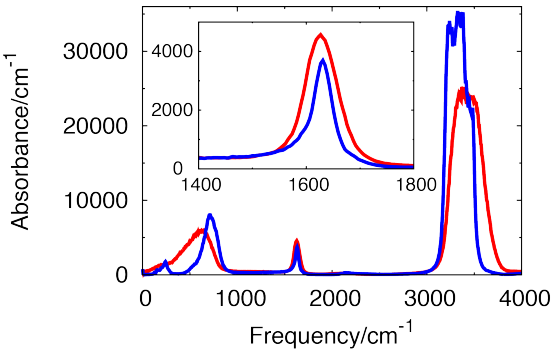

Figure 3.1: IR spectra of ice (blue) and liquid water (red) obtained from MD simulations with the TTM3-F potential. The inset shows the magnification of the HOH bend region.

3.4 Results and discussion

Figure 3.1 shows the IR spectra of ice (blue line) and liquid water (red line) obtained with TTM3-F potential. Intermolecular translational and rotational motions are seen at 200 cm^{-1} and 600 cm^{-1} as broad bands in liquid water, whereas two distinct peaks with the corresponding maxima approximately at 200 cm^{-1} and 800 cm^{-1} are obtained for ice. The peak at 60 cm^{-1}, arising from the low frequency translational motion, is significantly suppressed in ice, whereas it appears as a shoulder in the spectra of liquid water in agreement with the experimental results [3, 5].

The permanent, induced, and cross terms defined in eq. (3.3) are shown in Figure 3.2. The IR spectrum in the intermolecular region mainly arises from the permanent term both in ice and in liquid water. Although the spectrum shows a shoulder around 200 cm^{-1} due to the cross term, the intensity of the shoulder is smaller than the experimental results. Previous analysis of this feature via CPMD simulations suggests that the shoulder is related to the intermolecular charge transfer [46].

The peak maxima of the OH stretch are centered at 3340 cm^{-1} in ice and at 3430 cm^{-1} in liquid water, respectively. The peak of the OH stretch in ice is narrow and red-shifted

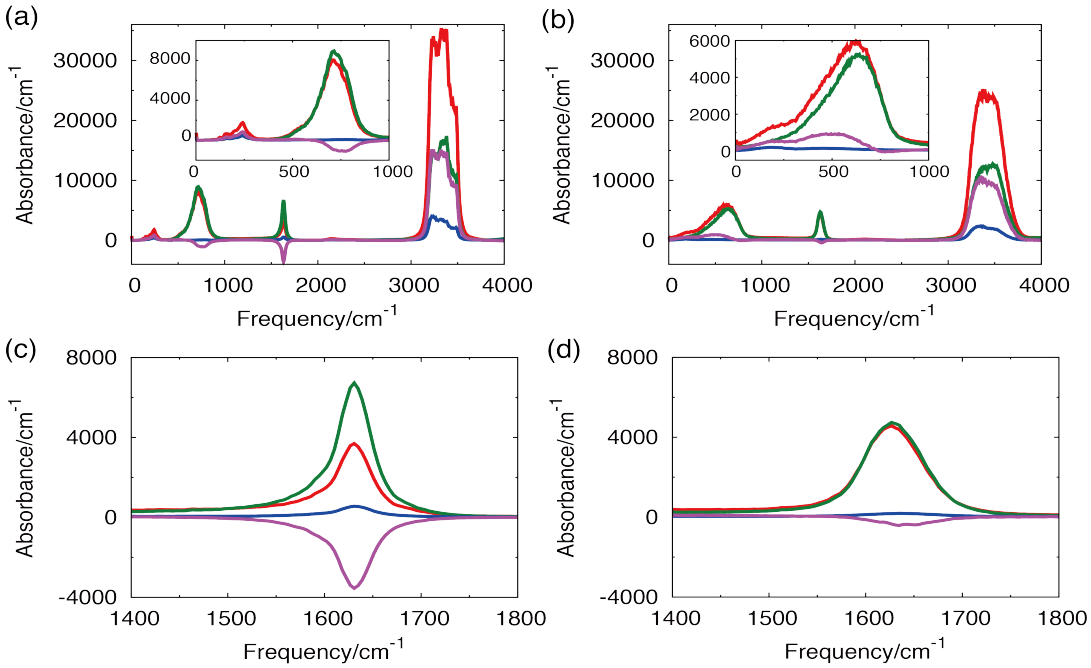

Figure 3.2: IR spectrum (red) and its components arising from the permanent (green), induced (blue), and cross term (purple) of (a) ice and (b) liquid water obtained from the MD simulations. The inset shows the magnifications in the intermolecular region. Panels (c) and (d) are magnifications of the HOH bend region in ice and liquid water, respectively.

compared to that in liquid water due to the less heterogeneous, stronger HBs in ice. It has been previously suggested that the calculated OH stretching band consists of three peaks due to the intermolecular vibrational coupling [47]. The intensity of the OH stretch in liquid water is the same as reported in Ref. [34]. However, it is much larger than the IR spectrum in the paper on the TTM3-F model [31] because a long time interval was used in the calculation of the dipole correlation function in Ref [31]. Since the permanent and cross terms of the OH stretch in ice are slightly larger than those in liquid water, the IR intensity of the OH stretch in ice is larger than that in liquid water as seen in Figures 3.2(a) and 3.2(b).

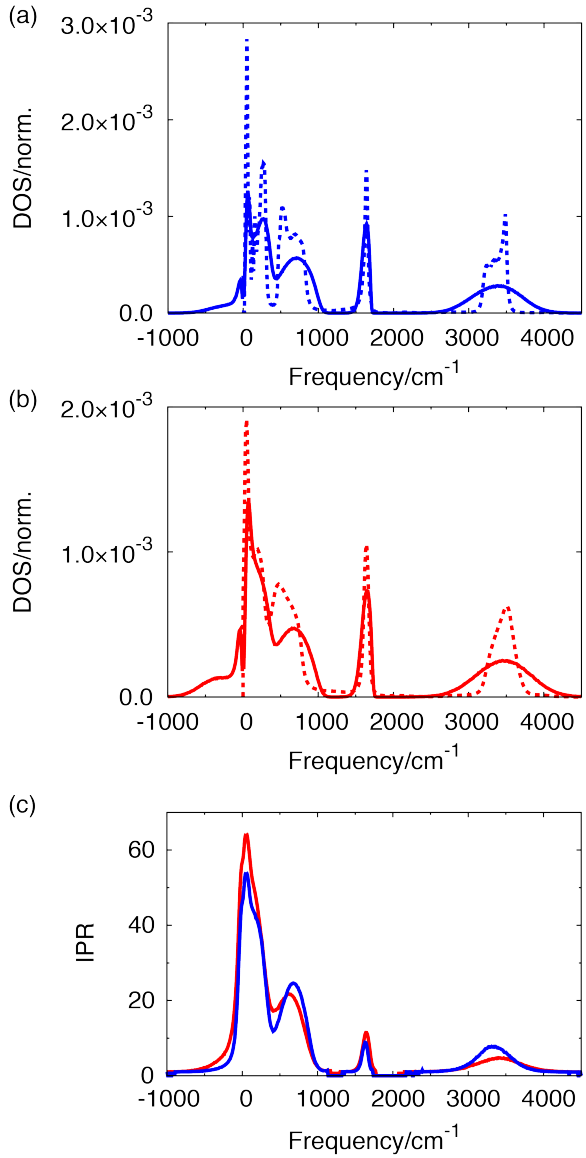

Figure 3.3: Density of states (DOS) of (a) ice and (b) liquid water obtained from velocity-velocity correlation function (dotted line) and normal mode analysis (solid line). The DOS is normalized by the integrated values. (c) Inverse participation ratio (IPR) of ice (blue) and liquid water (red).

The IR spectra of the HOH bend of ice and liquid water are shown in the inset of Fig. 3.1. The calculated IR intensity of the HOH bend in ice is weaker than that in liquid water in

agreement with the experimental result [4], although the calculated width of the HOH bend in ice is narrower than the experimental result. Figures 3.2(c) and 3.2(d) show the three terms of the HOH bend in ice and liquid water. In liquid water, the contributions of the induced and cross terms are very small and, thus, the IR intensity of the HOH bend mainly arises from the permanent term. On the other hand, the cross term in ice shows a large negative value, though the intensity of the permanent term in ice is larger than that in liquid water. As a result, the total IR intensity of the HOH bend in ice is weaker than that in liquid water.

The density of states (DOS) calculated from the velocity-velocity correlation function and normal mode analysis are shown in Figures 3.3(a) and 3.3(b). The DOS of ice calculated from the velocity-velocity correlation function shows structures at the OH stretch and intermolecular regions, whereas the one calculated from the normal mode analysis exhibits structureless inhomogeneous broad bands. The DOS of the HOH bend calculated from the normal mode analysis also shows inhomogeneous broadening that is about two times broader than that calculated from the velocity-velocity correlation function as the OH stretch.

The inverse participation ratio (IPR) [48] is shown in Figure 3.3(c). The IPR of the mode α is given by

$$R_\alpha = \frac{1}{\sum_{I=1}^{N_{\mathrm{mol}}}[\sum_{i\in I} U_{\alpha i}^2]^2}. \qquad (3.10)$$

Here **U** is the normal mode transformation matrix and N_{mol} is the total number of the molecules. If a normal mode is localized on a single molecule, i.e. the eigenvector elements of only one molecule is nonzero, the IPR of the mode would be equal to 1. On the other hand, for a completely delocalized mode, the IPR of the mode is equal to N_{mol}. The IPRs of the HOH bend in ice and liquid water are 9 and 11, respectively, whereas those of the OH stretch in ice and liquid water are 8 and 5, respectively. The range of numbers for liquid water obtained via the IPR analysis is consistent with the estimates reported earlier using a different metric, [33] suggesting that a number of ~10 neighbors is sufficient to reproduce the

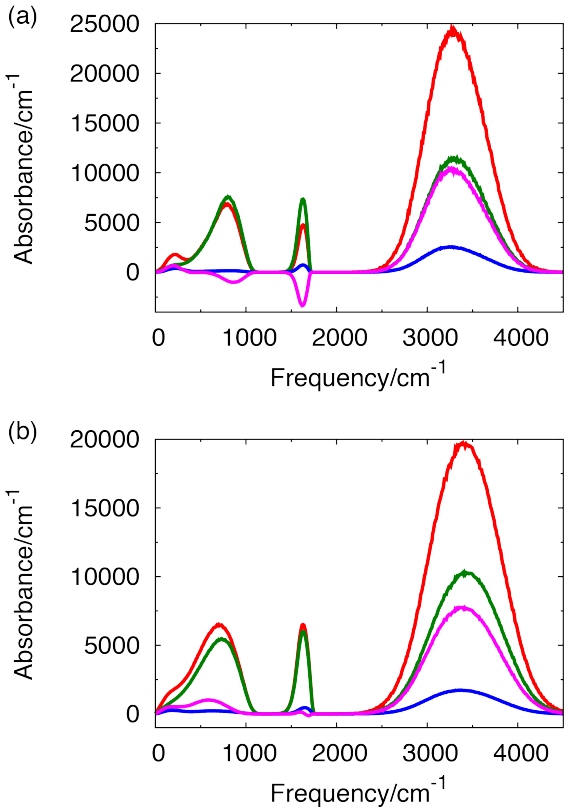

Figure 3.4: IR spectrum (red), and its components arising from the permanent (green), induced (blue), and cross term (purple) of (a) ice and (b) liquid water obtained from the normal mode approximation.

electric field along the OH bond and fully recover the structure of the OH stretching band with respect to the bulk spectra of liquid water. When the molecule with the largest IPR of a HOH bend (OH stretch) mode is defined as the central molecule of the mode, the average contribution of this central molecule to the HOH bend amounts to 0.43 and 0.38 for ice and liquid water, respectively. The cumulated contribution of the HOH bend within the first hydration shell of the central molecule amounts to 0.52 and 0.48 for ice and liquid water, respectively. The corresponding contributions of the central molecule to the OH stretch are 0.48 and 0.59, and the cumulated contribution within the first hydration shell of the central

molecule of the OH stretch is 0.70 and 0.84 for ice and liquid water, respectively. The HOH bend is therefore more delocalized than the OH stretch.

Figures 3.4(a) and 3.4(b) show the contributions of the permanent, induced, and cross terms in the IR spectra of ice and liquid water calculated from the normal mode analysis. The IR spectra calculated from the normal mode analysis are broader than those obtained via the dipole correlation function from the MD simulations because of the absence of motional narrowing in the former. Similar to the results of the MD simulation, the IR intensity of the HOH bend in liquid water arises almost exclusively from the permanent term as the contributions of the induced and cross terms are small. In contrast, the cross term of the HOH bend in ice (like the case for liquid water) is negative. Thus, the total IR intensity of the HOH bend in ice is weaker than that of the permanent term in ice and also the IR intensity of the bend in liquid water, similar to the result obtained from the MD simulations.

The author has examined the decrease in the IR intensity of the HOH bend of ice using normal mode analysis. To clarify the origin of the negative contribution of the cross term in the IR spectrum of ice, the radial component of the cross term was analyzed by using the following equation,

$$I_\alpha(r) = \langle \sum_j \left\{ \frac{\partial \mu_i^{\mathrm{perm}}}{\partial Q_\alpha} \cdot \frac{\partial \mu_j^{\mathrm{ind}}}{\partial Q_\alpha} + \frac{\partial \mu_i^{\mathrm{ind}}}{\partial Q_\alpha} \cdot \frac{\partial \mu_j^{\mathrm{perm}}}{\partial Q_\alpha} \right\} \delta(r - r_{ij}) \rangle, \qquad (3.11)$$

where α is a mode, i.e. HOH bend or OH stretch, *i* is the central molecule of the mode α and *j* is a molecule located at distance *r* from molecule *i* and μ_k^{perm} and μ_k^{ind} are the permanent and induce dipole moments of molecule *k*. The first and second terms of eq. (3.11) for the HOH bend and the OH stretch together with the Oxygen-Oxygen radial distribution function are presented in Figure 3.5. Since the second term of eq. (3.11) (dotted lines in Figures 3.5(b) and 3.5(c)) is very small compared with the first term (solid lines in Figures 3.5(b) and 3.5(c)) for both the HOH bend and the OH stretch, the author will

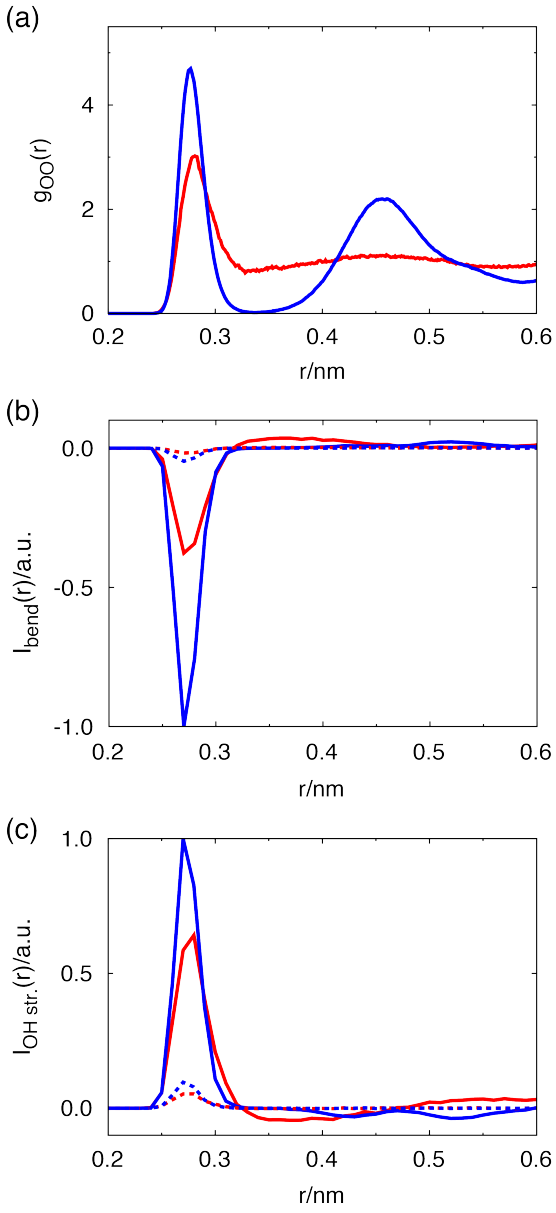

Figure 3.5: (a) Oxygen-Oxygen radial distribution functions of ice (blue) and liquid water (red). Radial components of the cross term for the HOH bend (panel (b)) and the OH stretch (panel (c)). The solid and dotted lines trace the first and second term of eq. (11), whereas blue (red) lines denote the results for ice (liquid water).

thereafter consider only the first term of eq. (3.11) in the present analysis. As seen in Figure 3.5(b), the negative correlation for the HOH bend in ice mainly arises from that between the permanent dipole moment of a given central molecule and the induced dipole moment in the first hydration shell of that molecule. Indeed, the correlation between the permanent dipole moment of the central molecule and the induced dipole moment of its second and outer hydration shells is negligible in ice. In contrast, in liquid water the negative correlation in the first hydration shell is weakened because of the disordered orientation. In addition, the permanent dipole moment of the central molecule and the induced dipole moment of its second and outer hydration shells have a positive correlation in liquid water. As a result, the cross term of the HOH bend is further weakened in liquid water.

The radial component of the cross term for the OH stretch is shown in Figure 3.5(c). Contrary to the negative correlation found for the HOH bend, the correlation between the permanent dipole moment of the central molecule and the induced dipole moment in its first hydration shell is positive for the OH stretch. Additionally, the correlation between the permanent dipole moment and the induced dipole moment of its second and outer hydration shells is negligible. As was the case for the correlation in the HOH bend, the correlation between the permanent dipole moment of the central molecule and the induced dipole moment of its first hydration shell in liquid water is smaller than that in ice. It is noted that similar negative and positive intermolecular correlations for the HOH bend and OH stretch modes were also reported during previous CPMD simulations [49].

Figure 3.6 shows the distribution of the magnitude of the correlation between the permanent dipole moment of the central molecule and the induced dipole moment of the molecule in its first hydration shell. The author has defined the HB acceptor and donor molecules as the nearest molecule from the hydrogen atoms of the central molecule and the two nearest molecules from the oxygen atom of the central molecule, respectively. The

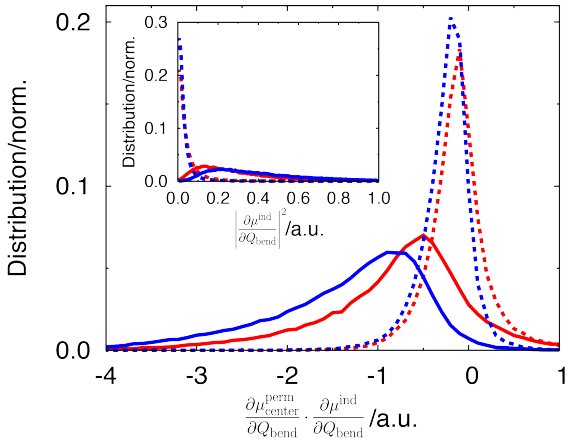

Figure 3.6: Distributions of the correlation between the permanent dipole moment of a central molecule and the induced dipole moment of the molecule in its first hydration shell. Solid (dotted) lines trace the correlation between a central molecule and its HB acceptor (donor) molecule, whereas blue (red) lines denote the results for ice (liquid water). Inset shows the distribution of $\left|\frac{\partial \mu^{\mathrm{ind}}}{\partial Q_{\mathrm{bend}}}\right|^2$ in the first hydration sell. The notation in the inset is the same as in the rest of the figure.

correlation between the permanent dipole moment of the central molecule and the induced dipole moment of its HB donor molecule is small since the induced dipole moment of the HB donor molecule is insensitive to the bend motion of the central molecule as shown in the inset of Figure 3.6. The anti-correlation between the permanent dipole moment of the central molecule and the induced dipole moment of the HB acceptor molecule is larger than that of the HB donor molecule both in ice and liquid water. The wide distribution of the anti-correlation is due to the sensitivity of the induced dipole moment of the HB acceptor molecule to the OH stretch of the central molecule as shown in the inset of Figure 3.6.

The author will now discuss the molecular picture of the anti-correlation between the permanent dipole moment of the central molecule and the induced dipole moment of its HB

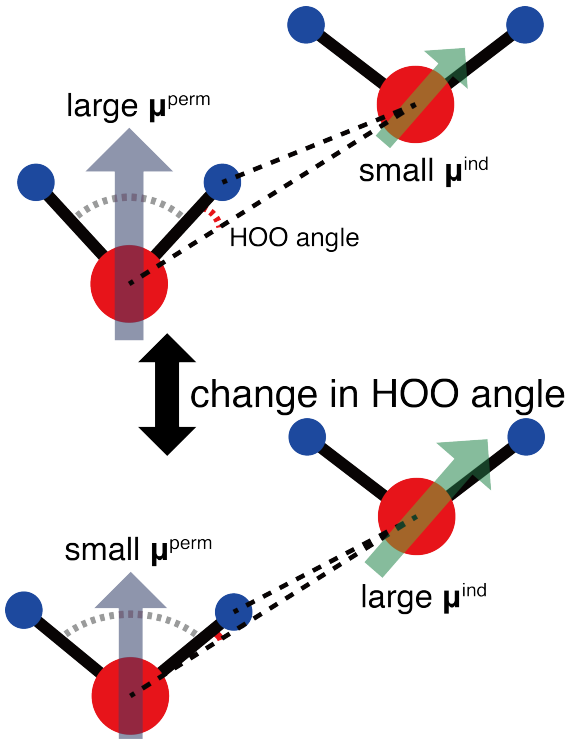

Figure 3.7: Scheme showing the origin of the anti-correlation between the permanent dipole moment of a central molecule and the induced dipole moment of its HB acceptor molecule.

acceptor molecules. The distribution of the HOH angle in ice and liquid water is centered around 106 degrees and the intermolecular Oxygen-Oxygen-Oxygen angle is around 109 degrees. When the HOH angle of the central molecule decreases, the permanent dipole moment of the central molecule becomes larger (Figure 3.7, upper panel). In addition, the distance between the oxygen atom of the HB acceptor molecule and the hydrogen atom of the central molecule becomes longer. Thus, the induced dipole moment of the HB acceptor molecule decreases due to the decrease in the electric field from the hydrogen atom of the central molecule. Consequently, the increase in the HOH angle of the central molecule

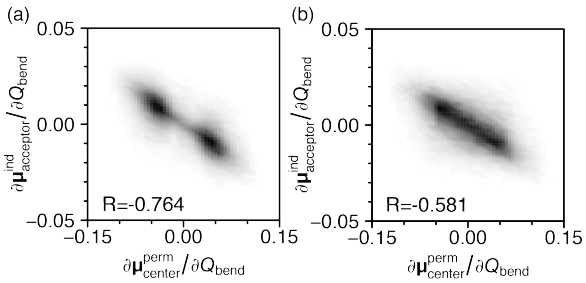

Figure 3.8: Correlation of the permanent dipole moment of a central molecule and the induced dipole moment of its HB acceptor molecule in (a) ice with ~50,000 points and (b) liquid water with ~40,000 points. The correlation coefficients (R) are also shown.

results in the decrease in the permanent dipole moment of the central molecule and the increase in the induced dipole moment of the HB acceptor molecule (Figure 3.7, lower panel). It is this variation that causes the anti-correlation between the permanent dipole moment of the central molecule and the induced dipole moment of its HB acceptor. Since the HB network is more disordered and consequently the electric field is weakened in liquid water when compared to ice, the anti-correlation between the permanent dipole moment of the central molecule and the induced dipole moment of the HB acceptor molecule is weaker in liquid water than in ice. As indeed shown in Figures 3.8(a) and 3.8(b), the anti-correlation between $\frac{\partial \mu^{\mathrm{perm}}_{\mathrm{center}}}{\partial Q_{\mathrm{bend}}}$ and $\frac{\partial \mu^{\mathrm{ind}}_{\mathrm{acceptor}}}{\partial Q_{\mathrm{bend}}}$ in ice is stronger than that in liquid water.

Similarly, for the OH stretch the permanent dipole moment of the central molecule is larger when its intramolecular OH distance is longer. At the same time, the induced dipole moment of the HB acceptor molecule is larger because of the short intermolecular Oxygen-Hydrogen distance. Thus, the permanent dipole moment of the central molecule and the induced dipole moment of the HB acceptor molecule show a positive correlation in both ice and liquid water, as shown in Figures 3.2(a), 3.2(b) and 3.5(c).

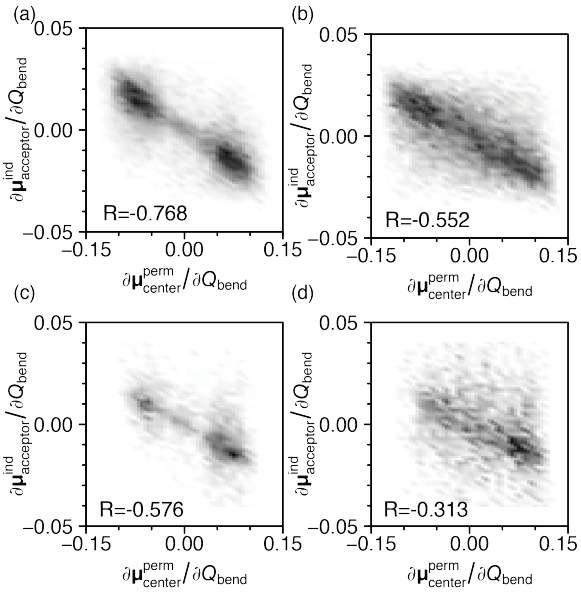

Figure 3.9: Correlation of the permanent dipole moment of a central molecule and the induced dipole moment of its HB acceptor molecule from water pentamer clusters extracted from the ice and liquid water trajectories. (a) ice and (b) liquid water using TTM3-F potential with ~10,000 points, (c) ice and (d) liquid water based on MP2 calculations with ~3,000 points. The correlation coefficients (R) are also shown.

All previous results are obtained from the MD trajectories and the normal mode analysis obtained with the TTM3-F potential. To examine the validity of the results obtained from the simulations with TTM3-F potential, the author investigated the relation between the $\frac{\partial \mu^{\mathrm{perm}}}{\partial Q_{\mathrm{bend}}}$ term of the central molecule and the $\frac{\partial \mu^{\mathrm{ind}}}{\partial Q_{\mathrm{bend}}}$ term of the HB acceptor molecules in pentamer water clusters evaluated via MP2 *ab initio* calculations. The correlations between those two terms calculated for pentamers with the TTM3-F potential and MP2 are shown in Figure 3.9. The comparison suggests that the results obtained from the MP2 calculations and with the TTM3-F potential are in excellent agreement in clearly documenting the strong anti-correlation for pentamers taken from ice and a weaker anti-correlation in those extracted

from liquid water simulations. This further justifies the results and conclusions reached by the analysis of the trajectories obtained with the TTM3-F potential.

3.5 Conclustions

The difference in the IR intensities of the HOH bend between ice and liquid water was investigated using the TTM3-F interaction potential, since this potential correctly reproduces the HOH angle and the IR intensity of the HOH bend in ice and liquid water. The author decomposed the IR spectra into the components arising from the permanent, induced, and cross terms. The author found that the IR intensity of the HOH bend in ice is weakened by the strong anti-correlation between the permanent dipole moment of a molecule and the induced dipole moment of its HB acceptor molecule, and furthermore that this anti-correlation is small in liquid water because of the disordered HB structure. This anti-correlation in the HOH bend was confirmed by performing MP2 calculations on water pentamers extracted from the liquid water and ice trajectories, which further confirmed the correct behavior of the TTM3-F potential in reproducing this feature of the spectra.

In contrast to the HOH bend, the OH stretch shows a positive correlation between the permanent dipole moment of a molecule and the induced dipole moment of its HB acceptor. Since the ordered HB structure increases the positive correlation, the IR intensity of the OH stretch in ice is larger than that in liquid water.

The sensitivity of the OH stretch on the underlying HB environment is well established. In this study the author demonstrated that the IR intensity of the HOH bend is also sensitive to the HB structure. Since the HOH bend is more delocalized than the OH stretch as shown in terms of the IPR, the properties of the HOH bend would be more strongly dependent on the HB network than for the OH stretch.

References of chapter 3

[1] D. Eisenberg and W. Kauzmann, *The structure and properties of water*, Clarendon Press, 1969.

[2] I. Ohmine and H. Tanaka, Chem. Rev. **93**, 2545 (1993).

[3] J. E. Bertie, H. J. Labbe, and E. Whalley, J. Chem. Phys. **50**, 4501 (1969).

[4] B. Zelent, N. V. Nucci, and J. M. Vanderkooi, J. Phys. Chem. A **108**, 11141 (2004).

[5] J. E. Bertie and Z. Lan, Appl. Spectrosc. **50**, 1047 (1996).

[6] J. J. Loparo, S. T. Roberts, and A. Tokmakoff, J. Chem. Phys. **125**, 194521 (2006).

[7] J. J. Loparo, S. T. Roberts, and A. Tokmakoff, J. Chem. Phys. **125**, 194522 (2006).

[8] J. B. Asbury, T. Steinel, K. Kwak, S. A. Corcelli, C. P. Lawrence, J. L. Skinner, and M. D. Fayer, J. Chem. Phys. **121**, 12431 (2004).

[9] B. Auer, R. Kumar, J. R. Schmidt, and J. L. Skinner, Proc. Natl. Acad. Sci. **104**, 14215 (2007).

[10] D. Kraemer, M. L. Cowan, A. Paarmann, N. Huse, E. T. J. Nibbering, T. Elsaesser, and R. J. D. Miller, Proc. Natl. Acad. Sci. **105**, 437 (2008).

[11] F. Perakis and P. Hamm, Phys. Chem. Chem. Phys. **14**, 6450 (2011).

[12] F. Mallamace, M. Broccio, C. Corsaro, A. Faraone, D. Majolino, V. Venuti, L. Liu, C. Y. Mou, and S. H. Chen, Proc. Natl. Acad. Sci. **104**, 424 (2007).

[13] S. Ashihara, N. Huse, A. Espagne, E. T. J. Nibbering, and T. Elsaesser, J. Phys. Chem. A **111**, 743 (2007).

[14] J. Lindner, P. Vohringer, M. S. Pshenichnikov, D. Cringus, D. A. Wiersma, and M. Mostovoy, Chem. Phys. Lett. **421**, 329 (2006).

[15] S. Ashihara, S. Fujioka, and K. Shibuya, Chem. Phys. Lett. **502**, 57 (2010).

[16] L. Piatkowski and H. J. Bakker, J. Chem. Phys. **135**, 214509 (2011).

[17] P. Bodis, O. F. A. Larsen, and S. Woutersen, J. Phys. Chem. A **109**, 5303 (2005).

[18] F. Ingrosso, R. Rey, T. Elsaesser, and J. T. Hynes, J. Phys. Chem. A **113**, 6657 (2009).

[19] R. Rey, F. Ingrosso, T. Elsaesser, and J. T. Hynes, J. Phys. Chem. A **113**, 8949 (2009).

[20] A. Bastida, J. Zúñiga, A. Requena, and B. Miguel, J. Chem. Phys. **131**, 204505 (2009).

[21] A. Bastida, J. Zúñiga, A. Requena, and B. Miguel, J. Chem. Phys. **136**, 234507 (2012).

[22] A. Kandratsenka, J. Schroeder, D. Schwarzer, and V. S. Vikhrenko, J. Chem. Phys. **130**, 174507 (2009).

[23] W. S. Benedict, N. Gailar, and E. K. Plyler, J. Chem. Phys. **26**, 1139 (1959).

[24] I. C. Baianu, N. Boden, D. Lightowlers, and M. Mortimer, Chem. Phys. Lett. **54**, 169 (1978).

[25] M. A. Floriano, D. D. Klug, E. Whalley , E. C. Svensson, V. F. Sears, and E. D. Hallman, Nature (London) **329**, 821 (1987).

[26] S. S. Xantheas, J. Chem. Phys. **102**, 4505 (1995).

[27] Y. A. Mantz, F. M. Geiger, L. T. Molina, M. J. Molina, and B. L. Trout, J. Chem. Phys. **113**, 10733 (2000).

[28] J. Jeon, A. E. Lefohn, and G. A. Voth, J. Chem. Phys. **118**, 7504 (2003).

[29] G. S. Fanourgakis and S. S. Xantheas, J. Chem. Phys. **124**, 174504 (2006).

[30] C. J. Burnham and S. S. Xantheas, J. Chem. Phys. **116**, 5115 (2002); G. S. Fanourgakis and S. S. Xantheas, J. Phys. Chem. A **110**, 4100 (2006).

[31] G. S. Fanourgakis and S. S. Xantheas, J. Chem. Phys. **128**, 074506 (2008).

[32] S. Habershon, G. S. Fanourgakis, and D. E. Manolopoulos, J. Chem. Phys. **129**, 074501 (2008).

[33] F. Paesani, S. S. Xantheas and G. A. Voth, J. Phys. Chem. B **113**, 13118 (2009).

[34] J. Liu, W. H. Miller, G. S. Fanourgakis, S. S. Xantheas, S. Imoto, and S. Saito, J. Chem. Phys. **135**, 244503 (2011).

[35] F. Paesani, I. Satoru and G. A. Voth, J. Chem. Phys. **127**, 074506 (2007).

[36] F. Paesani and G. A. Voth, J. Phys. Chem. B **113**, 5702 (2009).

[37] F. Paesani, S. Yoo, H. J. Bakker and S. S. Xantheas, J. Phys. Chem. Lett. **1**, 2316 (2010).

[38] S. Saito and I. Ohmine, J. Chem. Phys. **108**, 240 (1998).

[39] H. Partridge and D. W. Schwenke, J. Chem. Phys. **106**, 4618 (1997).

[40] B. T. Thole, Chem. Phys. **59**, 341 (1981).

[41] M. P. Allen and D. J. Tildesley, *Computer Simulation of Liquids*, Oxford University Press, 1991.

[42] A. J. Stone, J. Chem. Theor. Comp. **1**, 1128 (2005).

[43] A. J. Stone, Distributed multipole analysis of gaussian wavefunctions GDMA version 2.2, (2005).

[44] R. A. Kendall, T. H. Dunning Jr, and R. J. Harrison, *J. Chem. Phys.* **96**, 6796 (1992).

[45] M. J. Frisch, G. W. Trucks, H. B. Schlegel, G. E. Scuseria, M. A. Robb, J. R. Cheeseman, G. Scalmani, V. Barone, B. Mennucci, G. A. Petersson, H. Nakatsuji, M. Caricato, X. Li, H. P. Hratchian, A. F. Izmaylov, J. Bloino, G. Zheng, J. L. Sonnenberg, M. Hada, M. Ehara, K. Toyota, R. Fukuda, J. Hasegawa, M. Ishida, T. Nakajima, Y. Honda, O. Kitao, H. Nakai, T. Vreven, J. A. Montgomery, Jr., J. E. Peralta, F. Ogliaro, M. Bearpark, J. J. Heyd, E. Brothers, K. N. Kudin, V. N. Staroverov, R. Kobayashi, J. Normand, K. Raghavachari, A. Rendell, J. C. Burant, S. S. Iyengar, J. Tomasi, M. Cossi, N. Rega, J. M. Millam, M. Klene, J. E. Knox, J. B. Cross, V. Bakken, C. Adamo, J. Jaramillo, R. Gomperts, R. E. Stratmann, O. Yazyev, A. J. Austin, R. Cammi, C. Pomelli, J. W. Ochterski, R. L. Martin, K. Morokuma, V. G. Zakrzewski, G. A. Voth, P. Salvador, J. J. Dannenberg, S. Dapprich, A. D. Daniels, O. Farkas, J. B. Foresman, J. V. Ortiz, J. Cioslowski, and D. J. Fox, Gaussian 09 Revision A.1, Gaussian Inc. Wallingford CT 2009.

[46] M. Sharma, R. Resta, and R. Car, Phys. Rev. Lett. **95**, 187401 (2005).

[47] L. Shi, S. Gruenbaum, and J. L. Skinner, J. Phys. Chem. B **116**, 13821 (2012).

[48] M. Cho, G. R. Fleming, S. Saito, I. Ohmine, and R. M. Stratt, J. Chem. Phys. **100**, 6672 (1994).

[49] W. Chen, M. Sharma, R. Resta, G. Galli, and R. Car, Phys. Rev. B **77**, 245114 (2008).

Chapter 4

Frequency fluctuations of the OH stretch and the HOH bend in liquid water*

4.1 Introduction

Water is associated with various anomalous properties [1] and its structure and dynamics have been intensively investigated both experimentally and theoretically [2-4]. The dynamics of water are characterized by a hydrogen bond (HB) network fluctuating with a wide range of time scales ranging from femto-seconds to several pico-seconds [5].

The dynamics of water has been experimentally probed using various spectroscopic methods [6-10]. In particular, the infrared (IR) spectrum of the OH stretch has been extensively studied. It is known that the OH stretch is sensitive to its local environment since the frequency of the OH stretch correlates with the strength of the underlying HB. However, information obtained from linear spectroscopy is limited and, thus, the detailed dynamics of the HB network cannot be fully resolved. Non-linear spectroscopy can be employed to analyze the details of the frequency fluctuations [11,12]. In particular, third-order nonlinear IR spectroscopy, e.g. two-dimensional (2D) IR spectra, has been used to provide detailed information about the dynamics of the OH stretch [13,14]. The frequency correlations of probe OH (OD) stretch in liquid D_2O (H_2O) shows a fast decay with a 60 fs time constant due to the librational motion, a recursion with a 130 fs time constant because of the HB stretch, and a slow decay with a 1 ps time constant arising from the HB rearrangement. In addition, the 2D IR spectra indicate the inhomogeneous frequency fluctuation of the OH stretch in liquid D_2O due to the difference of the HB strength [15,16]. It is also known that the frequency fluctuation of the OH stretch in neat water is quite fast, less than 50 fs, due to strong inter- and intra-molecular couplings [17,18].

* S. Imoto, S. S. Xantheas, and S. Saito, "Ultrafast dynamics of liquid water: Frequency fluctuations of the OH stretch and the HOH bend", J. Chem. Phys. **139**, 044503 (2013).

The 2D IR spectra of the OH stretch have also been studied theoretically. It was found that the frequency fluctuation of the OH stretch in liquid D_2O is correlated to the fluctuation of the electric field along the OH bond [19,20]. Furthermore, it was shown that the molecular reorientation coupled with HB exchange is responsible for the long time decay of the frequency correlation with the time constant of 1 ps [21]. The 2D IR spectra of the OH stretch in liquid water have been calculated using a numerical integration of the Schrödinger equations and it was also shown that the spectral diffusion after 200 fs arises from the intermolecular coupling between the OH stretching motions [22-24].

In contrast to the OH stretch, the HOH bend has not been extensively studied. The time scale of the frequency fluctuation of the HOH bend has not been analyzed to-date either theoretically or experimentally. The scarcity of the theoretical studies regarding the HOH bend can be in part attributed to the difficulty in reproducing its properties. For example, simple model potentials cannot reproduce the difference of the average HOH angle between the gas and condensed phases [25].

In this study, the author reports the frequency fluctuations of the OH stretch and the HOH bend in liquid water by analyzing the 2D IR spectra calculated from molecular dynamics (MD) simulations. These MD simulations were performed with the *ab initio*-based, flexible, polarizable, transferable TTM3-F potential, which incorporates an intramolecular charge transfer depending on the environment and correctly reproduces the properties of both the HOH bend and the OH stretch in liquid water and ice [26-28]. The 2D IR spectra were evaluated directly from the third-order response function, instead of using the frequency-frequency time correlation function, $\langle \delta\omega(0)\delta\omega(t)\rangle$. Although the author employed the high-temperature approximation, the inter- and intra-molecular couplings are explicitly taken into account in the present analysis.

The calculated 2D IR spectra of the OH stretch show the fast decay of the frequency correlation: an initial decay with a time constant of ~40 fs, a plateau from 60 to 100 fs, and a slow decay with a time constant of ~180 fs. The frequency fluctuation of the OH stretch is due to the couplings with the HB stretch at 200 cm^{-1} and the librational motion as suggested during previous experimental and theoretical studies [18, 22-24]. In contrast, the frequency correlation of the HOH bend mainly decreases with a time constant less than 100 fs, exhibits a plateau from 100 to 150 fs, and decays with a time constant of ~120 fs. The author found that the frequency fluctuation of the HOH bend is caused by the strong couplings with the OH stretch as well as the intermolecular HB bend at 60 cm^{-1}.

The present chapter is organized as follows. In Section 4.2 the author briefly describes the theoretical background of the third-order IR spectroscopy and details of MD simulations. In Section 4.3 the author presents the 2D IR spectra of the OH stretch and the HOH bend and the analysis of those frequency fluctuations. The conclusions are given in Section 4.4.

4.2 Theoretical method and computational details

Most theoretical calculations of the third-order response function are based on mapping the electric field onto the vibrational frequency and employing Gaussian statistics for the frequency fluctuation [12]. During previous theoretical studies of the 2D IR spectra of the OH stretch in liquid water, the inter-OH stretch coupling was considered, however the coupling between the OH stretch and the HOH bend has not been taken into account [22-24]. In the present study the author calculates directly the third-order response function from non-equilibrium MD simulations. The details of the theoretical calculation of the third-order response function and corresponding spectra from non-equilibrium MD simulations are summarized in chapter 2. Here, the author

briefly describes the theoretical background and computational details for third-order nonlinear IR spectroscopy.

Third-order IR spectroscopy measures the third-order polarization, $P^{(3)}(\tau,T,t)$, which is expressed by the convolution of the third-order response function, $R^{(3)}(t_1,t_2,t_3)$, with the electric field as [11],

$$P^{(3)}(\tau,T,t)=\int_0^\infty dt_3\int_0^\infty dt_2\int_0^\infty dt_1\,E(t_s-t_3,\{\tau_i\})E(t_s-t_3-t_2,\{\tau_i\}) \qquad (4.1)$$

$$\times E(t_s-t_3-t_2-t_1,\{\tau_i\})R^{(3)}(t_1,t_2,t_3),$$

where

$$E(t,\{\tau_i\})=\sum_{i=1}^{3}\varepsilon_i(t-\tau_i)\exp\big(-i\omega_i(t-\tau_i)\big)\exp(-i\mathbf{k}_i\mathbf{r}_i)+\text{ c. c.}. \qquad (4.2)$$

Here, τ_1, τ_2, and τ_3 are the times of the centers of pulses and the three time intervals are defined as $\tau = \tau_2 - \tau_1$, $T = \tau_3 - \tau_2$, and $t = t_s - \tau_3$. The ω_i, k_i, and $\varepsilon_i(t)$ are the carrier frequency, wave vector, and envelope function of the pulse i, respectively. Equation (4.1) can be written as

$$P^{(3)}(\tau,T,t)=\sum_{\alpha=\mathrm{I}}^{\mathrm{IV}}\exp(-i\mathbf{k}_\alpha\mathbf{r})P_\alpha^{(3)}(\tau,T,t)+\text{c. c.}, \qquad (4.3)$$

where $P_{\mathrm{I}}^{(3)}$, $P_{\mathrm{II}}^{(3)}$, $P_{\mathrm{III}}^{(3)}$, and $P_{\mathrm{IV}}^{(3)}$ denote the third-order polarizations generated in the $\mathbf{k}_{\mathrm{I}} = -\mathbf{k}_1 + \mathbf{k}_2 + \mathbf{k}_3$, $\mathbf{k}_{\mathrm{II}} = \mathbf{k}_1 - \mathbf{k}_2 + \mathbf{k}_3$, $\mathbf{k}_{\mathrm{III}} = \mathbf{k}_1 + \mathbf{k}_2 - \mathbf{k}_3$, and $\mathbf{k}_{\mathrm{IV}} = \mathbf{k}_1 + \mathbf{k}_2 + \mathbf{k}_3$ phase matching conditions, respectively.

The third-order response function is given by [11]

$$R^{(3)}(t_1,t_2,t_3)=\left(\frac{i}{\hbar}\right)^3\mathrm{tr}\{\mathbf{M}(t_1+t_2+t_3)[\mathbf{M}(t_1+t_2),[\mathbf{M}(t_1),[\mathbf{M}(0),\rho_{\mathrm{eq}}]]]\}, \qquad (4.4)$$

where ρ_{eq} and $\mathbf{M}$ are the equilibrium density matrix and dipole operator of the system, respectively. By using the identity [30] with the Liouville operator for the system-field interaction,

$$\frac{i}{\hbar}[\mathbf{M}(t),\ ] \equiv iL_{\mathbf{M}}(t) = \lim_{\epsilon\to 0}\frac{1}{\epsilon}\{\exp(i\epsilon L_{\mathbf{M}}(t)) - 1\}, \qquad (4.5)$$

the third-order response function can be recast in the from

$$R^{(3)}(t_1,t_2,t_3) = \lim_{\epsilon\to 0}\frac{1}{\epsilon^2}\mathrm{tr}\{\mathbf{M}(t_1+t_2+t_3)(\exp(i\epsilon L_{\mathbf{M}}(t_1+t_2)) - 1) \qquad (4.6)$$

$$\times(\exp(i\epsilon L_{\mathbf{M}}(t_1)) - 1)\frac{i}{\hbar}[\mathbf{M}(0),\rho_{eq}]\}.$$

By applying a classical approximation, the author obtains the classical expression for the third-order response function based on non-equilibrium MD simulations expressed as [31]

$$R^{(3)}(t_1,t_2,t_3) \propto \langle\mathbf{M}(t_1+t_2+t_3)\dot{\mathbf{M}}(0)\rangle_{t_1,t_1+t_2} + \langle\mathbf{M}(t_1+t_2+t_3)\dot{\mathbf{M}}(0)\rangle_{\bar{t}_1,\overline{t_1+t_2}} \qquad (4.7)$$

$$-\langle\mathbf{M}(t_1+t_2+t_3)\dot{\mathbf{M}}(0)\rangle_{\bar{t}_1,t_1+t_2} - \langle\mathbf{M}(t_1+t_2+t_3)\dot{\mathbf{M}}(0)\rangle_{t_1,\overline{t_1+t_2}}.$$

Here $\langle\ \rangle$ indicates the ensemble average, the subscripts of each term denote the time of the application of external pulses as the perturbation and the over-bar on the subscripts represents the opposite direction of external pulse based on inverted force method [32].

The author used the TTM3-F interaction potential, which is the latest version of the *ab initio*-based charge transferable, flexible, polarizable Thole-Type Models (TTM) to describe the underlying inter- and intra-molecular interactions in liquid water [26-28,33-38]. The author briefly accounts for some of its salient features here. The intramolecular interaction and charge transfer of the TTM3-F potential are based on the monomer potential and dipole moment surfaces obtained from high level *ab initio* calculations [39], appropriately modified to describe the liquid phase [27]. Because of the intramolecular charge transfer feature, the TTM3-F potential reproduces the increase of the HOH angle in the condensed phase [26] with respect to the gas

phase monomer and the correct IR spectrum of the HOH bend. Four interaction sites are used for the intermolecular interaction in the TTM3-F potential. The oxygen-oxygen interaction is described by a Buckingham expotential-6. A positive charge is placed on each hydrogen atom and a negative charge and an isotropic point dipole moment are placed on the M-site located on the bisector of the HOH angle. The Thole type damping function is employed for the treatment of the electrostatic interaction [40].

All the MD simulations have been performed under the constant volume and energy conditions at a temperature of 300 K and a density of 1.0 g/cm^3. Periodic boundary conditions were employed and the long-range electric interactions were calculated using the Ewald sum. The induced dipole moment was computed iteratively at each step. Equations of motion were integrated using the velocity-Verlet algorithm with the time step of 0.1 fs, which is needed to solve the linear equations for the induced dipole moment [38]. Equilibrium MD simulations and normal mode analysis of the whole system were carried out using 125 water molecules. The total length of the trajectories was 500 ps. The normal mode analysis was performed every 1 fs along the equilibrium trajectories by using a five-point differentiation of the analytical force.

Non-equilibrium MD simulations were carried out for a system with 64 water molecules. The author applies the δ-function-like triangular short external fields, whose intensity and time duration are 1.2 V/Å and 0.2 fs, to calculate the third-order response function shown in Eq. (4.7). The average temperature rise due to the perturbative δ-function-like pulses was approximately 10 K during each non-equilibrium MD simulation. In order to calculate $P_{\mathrm{i}}^{(3)}$ in Eq. (4.3), Gaussian functions were used for the envelope function in Eq. (4.2),

$$\varepsilon_i(t) = \frac{1}{\sqrt{2\pi}\sigma_i}\exp\left(-\frac{t^2}{2\sigma_i^2}\right), \qquad (4.8)$$

where σ_i and ω_i were 40 fs and 1600 cm^{-1} for the HOH bend and 20 fs and 3500 cm^{-1} for the OH stretch. The third-order response function for $t_1 \leq 400$ fs and $t_3 \leq 400$ fs is used for the calculation of the 2D IR spectra. The 2D IR spectra were obtained by averaging over 320,000 trajectories for $t_2 < 100$ fs, 640,000 trajectories for $t_2 < 150$ fs, 1,280,000 trajectories for $t_2 < 300$ fs, and 2,560,000 trajectories for $t_2 < 500$ fs.

4.3 Results and Discussion

a. 2D IR spectrum and peaks shifts

The 2D IR spectrum is expressed using $P_{\mathrm{I}}^{(3)}(\tau, T, t)$ and $P_{\mathrm{II}}^{(3)}(\tau, T, t)$ as [41]

$$S(\omega_1, T, \omega_3) = \mathrm{Re}\int_0^\infty dt \int_0^\infty d\tau \exp(i(\omega_1\tau - \omega_3 t)) i P_{\mathrm{I}}^{(3)}(\tau, T, t) \qquad (4.9)$$

$$+\mathrm{Re}\int_0^\infty dt \int_0^\infty d\tau \exp(i(\omega_1\tau + \omega_3 t)) i P_{\mathrm{II}}^{(3)}(\tau, T, t).$$

The 2D IR spectra are sensitive to the correlation of the two vibrational frequencies, ω_1 and ω_3, separated by the waiting time T. When T is shorter than the time scale of the frequency fluctuation, the 2D IR spectra are elongated to the diagonal direction because of the strong correlation between ω_1 and ω_3. In contrast, when T is longer than the time scale of the frequency fluctuation, the two frequencies lose their correlation and in that case the 2D IR spectra become parallel to ω_1 axis. That is, the slope of the 2D IR spectra is correlated to the extent of the initial inhomogeneity.

The 2D IR spectra have positive and negative peaks [12]. The positive peak originates from the ground state bleach and the stimulated emission in which both ω_1 and ω_3 correspond to the $0 \rightarrow 1$ transition. In contrast, the negative peak arises from the excited state absorption and ω_1 and ω_3 correspond to the $0 \rightarrow 1$ and $1 \rightarrow 2$ transitions, respectively. The difference in ω_3 for

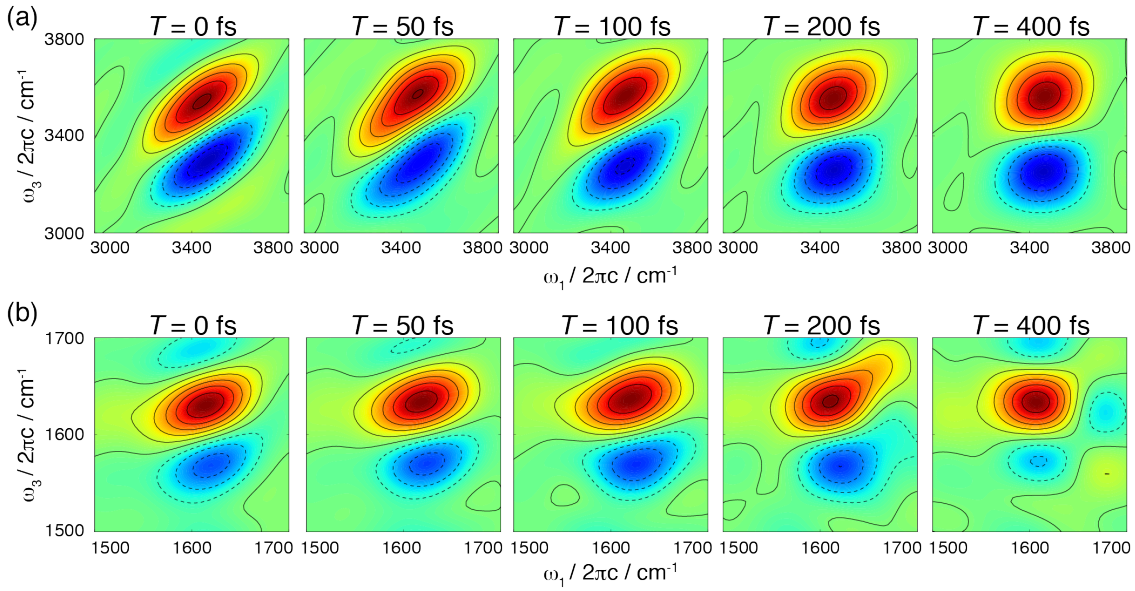

Figure 4.1: 2D IR spectra as a function of the waiting time for (a) the OH stretch and (b) the HOH bend in liquid water. The spectra are normalized to the maximum value.

the positive and negative peaks corresponds to the difference in the frequencies of the 0 → 1 and 1 → 2 transitions, i.e. the vibrational anharmonicity [42]. The dynamics in the present analysis are governed by classical mechanics and for this reason no discrete states exist. The frequencies in the present 2D IR spectra are related to those of the fluctuation of the dipole moment obtained from the trajectories perturbed by the electric fields, like in the conventional IR and sum frequency generation spectra calculated from classical MD simulations [43, 44].

Figure 4.1(a) shows the 2D IR spectra of the OH stretch. The 2D IR spectra of the OH stretch are diagonally elongated at T = 0 fs, indicating the strong correlation between ω_1 and ω_3. The vibrational anharmonicity of the OH stretch estimated from the difference of ω_3 between the positive and negative peaks is 240 cm^{-1}, which is in good agreement with the experimental result

of 250 cm^{-1} [18]. Although the spectral shape is rather elliptic at T = 0 fs, it becomes egg-shaped at T = 50 fs due to the increase / decrease in the peak intensity at (ω_1, ω_3) = (3400 cm^{-1}, 3700 cm^{-1}) / (3200 cm^{-1}, 3600 cm^{-1}). This change in the spectral shape arises from the heterogeneous dynamics of the local HB network as experimentally observed in Ref. [13]. In addition, the diagonal width decreases and the anti-diagonal width increases with increasing the waiting time T and then both the positive and negative peaks have an almost round shape at $T >$ 200 fs similarly to the previous theoretical calculations [22-24]. As in the other theoretical results, the rapid decay of the negative peak observed in the experiments [17,18] is not found in the present result either. However, the more recent experimental result by Tokmakoff *et al.* is similar to the present result [45].

To quantify the time scale of the frequency fluctuations, the slope of the 2D IR spectra of the OH stretch was examined. As seen by the red line in figure 4.2, the waiting time dependence of the slope consists of the following three processes: an initial decay with a time constant of ~40 fs, a plateau from 60 to 100 fs, and a slow decay with a time constant of ~180 fs. A similar temporal behavior was previously seen in the frequency-frequency time correlation function in Ref. [24]. In particular, the third process in liquid water is quite faster than those in liquid D_2O because of the inter- and intra-molecular resonances.

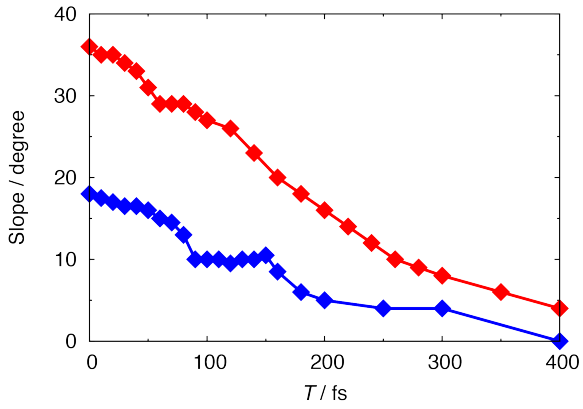

Figure 4.2: Slope of the 2D IR spectra as a function of the waiting time (T) for the OH stretch (red) and the HOH bend (blue).

Figure 4.1(b) shows the 2D IR spectra of the HOH bend. The slope of the 2D IR spectrum of the HOH bend at T = 0 fs is small compared to that of the OH stretch, which indicates a significant fast frequency fluctuation of the HOH bend. The frequency difference between the positive and negative peaks shows that the vibrational anharmonicity of the HOH bend is 60 cm^{-1}, which is slightly larger than the experimental result of 40 cm^{-1} [46]. The spectra change to a round shape with increasing T and become parallel to the ω_1 axis at T = 400 fs. In addition, the change of the spectral shape to the egg-shape seen in the 2D IR spectra of the OH stretch is not clearly seen in the time evolution of the 2D IR spectra of the HOH bend, a result suggesting that the frequency of the HOH bend is less sensitive to the local HB environment than that of the OH stretch.

The slope of the 2D IR spectra of the HOH bend is shown by a blue line in Fig. 4.2. It should be noted here that the initial slope of the HOH bend is about half of that of the OH stretch indicating that the frequency fluctuation of the HOH bend is significant even at T = 0 fs. Fig.

4.2 also exhibits an initial decay with a time constant of ~60 fs. The slope is almost constant from 100 to 150 fs and decays with a time constant of ~120 fs after T = 150 fs.

Figures 4.3(a) and 4.3(b) show the stimulated photon echo signal, $S_{\mathrm{PE}}(\tau,T) \propto \int_0^\infty dt \left|P_1^{(3)}(\tau,T,t)\right|^2$, of the OH stretch and the HOH bend. Known as three-pulse stimulated photon echo peak shift, the value τ of the maximum S_{PE} at a given waiting time T is related to the extent of the presence of the frequency correlation. The peak shift decays with increasing T due to the loss of the initial inhomogeneity [47]. The S_{PE} of the OH stretch at T = 0 fs has a maximum intensity at τ = 38 fs. The peak shift of the OH stretch behaves in a similar

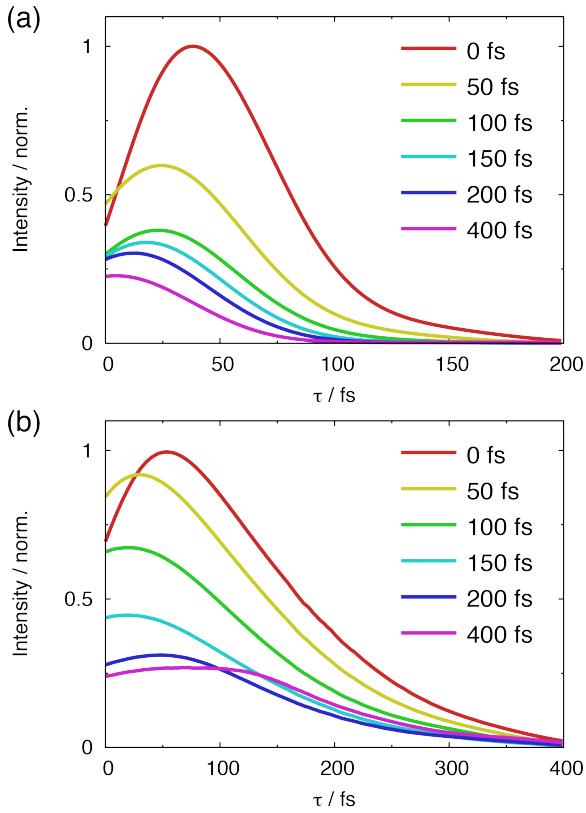

Figure 4.3: Stimulated photon echo signals of (a) the OH stretch and (b) the HOH bend at different waiting times.

way with the slope of the 2D IR spectra of the OH stretch with increasing T: an initial decay with a time constant of ~30 fs, a plateau from 50 to 100 fs, and a slow decay with a time constant of ~140 fs.

The S_{PE} of the HOH bend at T = 0 fs shows a larger peak shift of 53 fs when compared to that of the OH stretch. This is due to the smaller frequency fluctuation, $\langle \delta\omega^2 \rangle$, in the HOH bend than in the OH stretch. The peak shift clearly shows an initial decay with a time constant of ~70 fs, followed by a plateau from 100 to 150 fs and a slower decay with a time constant of ~120 fs, similar to the waiting time dependence of the slope of the 2D IR spectra of the HOH bend.

b. Fluctuation of normal mode frequency

The time evolution of the OH stretch and HOH bend frequencies along the equilibrium MD trajectories are examined using normal mode analysis to elucidate the molecular origins of the fast frequency fluctuation of these motions. Figures 4.4(a) and 4.5(a) show the spectra of the frequency fluctuation of the OH stretch and the HOH bend, viz.

$$\tilde{C}_\alpha(\omega) = \int dt \cos(\omega t) \langle \sum_i \delta\omega_{i\alpha}(t)\delta\omega_{i\alpha}(0) \rangle, \qquad (4.10)$$

$$\delta\omega_{i\alpha}(t) = \omega_{i\alpha}(t) - \langle \omega_{i\alpha} \rangle, \qquad (4.11)$$

where $\omega_{i\alpha}$ is the normal mode frequency of mode α, e.g. the OH stretch or the HOH bend of molecule i. Each mode is assigned to the molecule with the largest contribution. The averages of the largest contributions to the OH stretch and the HOH bend amount to ~0.6 and ~0.4, whereas the cumulative contributions within the first hydration shell are ~0.8 and ~0.5 for the OH stretch and the HOH bend, respectively [28]. The contributions of other molecules are, thus, much smaller than the largest contributions, which amount to ~0.4 (~0.6) for the HOH bend (OH stretch).

The frequency fluctuation of the OH stretch shows a strong peak at 3500 cm^{-1} due to the anharmonicity of the OH stretch (Fig. 4.4(a)). It is noted that the frequency of the OH stretch fluctuates due to the underlying intra- and inter-molecular anharmonic dynamics of the system, though the frequency is calculated using the normal mode analysis. As shown in figure 4.4(b), which emphasizes the contribution of the low frequency intermolecular motions, the spectrum of the OH stretch has a strong peak at 150 cm^{-1} due to the intermolecular HB stretch. It has been previously shown that the frequency fluctuation of the OH stretch in liquid D_2O is correlated to

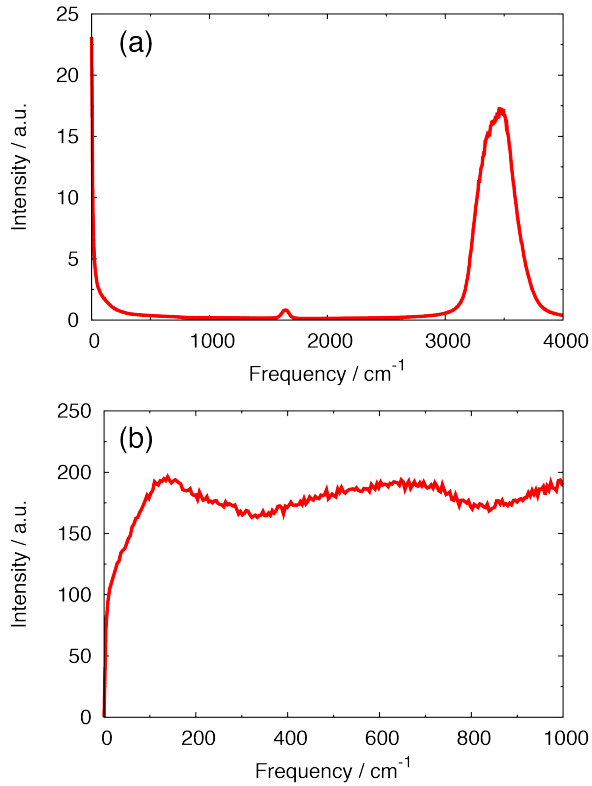

Figure 4.4: Spectra of the frequency fluctuation of the OH stretch: (a) $\tilde{C}(\omega)$ and (b) $\omega\tilde{C}(\omega)$ (cf. Eq. 4.10).

the fluctuation of the oxygen-oxygen distance [13]. The spectrum of the OH stretch also indicates the coupling between the OH stretch and the librational motion at ~700 cm^{-1} [13]. In contrast to the peaks of the OH stretch and intermolecular motions, the peak at 1600 cm^{-1} is much weaker, indicating that the frequency fluctuation of the OH stretch caused by the HOH bend is negligible.

The spectrum of the frequency fluctuation for the HOH bend shows a strong peak at 1600 cm^{-1} due to the anharmonicity of the HOH bend (Fig. 4.5(a)). The peak in the 3000 – 4000 cm^{-1}

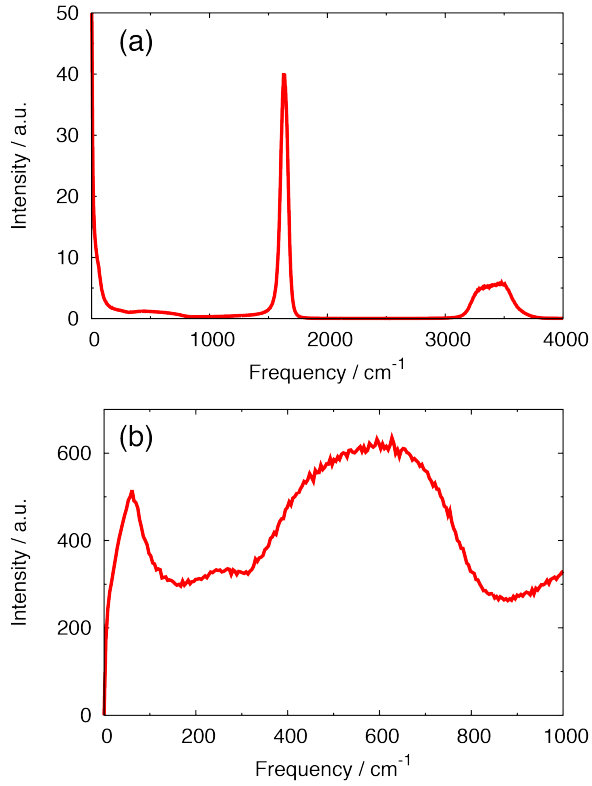

Figure 4.5: Spectra of the frequency fluctuation of the HOH bend: (a) $\tilde{C}(\omega)$ and (b) $\omega\tilde{C}(\omega)$ (cf. Eq. 4.10).

region originates from the coupling between the HOH bend and the OH stretch. As seen in figure 4.5(b), the frequency fluctuation of the HOH bend is also induced by the intermolecular HB bend at 60 cm^{-1}, whereas the coupling between the HOH bend and the intermolecular HB stretch at 200 cm^{-1} is weak. The present result shows that the frequency fluctuation of the HOH bend is due to the coupling between the HOH bend and the OH stretch and the intermolecular HB bend. Furthermore, $\tilde{C}(\omega)$ of the HOH bend, considering only the coupling between the HOH bend and the OH stretch, shows that the plateau of the frequency correlation of the HOH bend

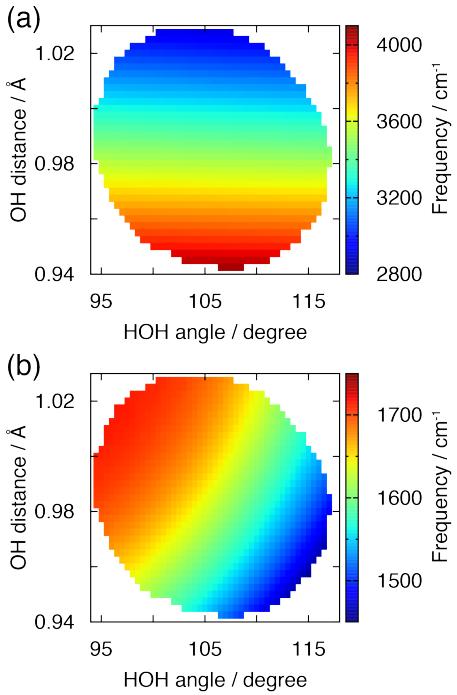

Figure 4.6: Relationship between the intramolecular structure and the normal mode frequencies of (a) the OH stretch and (b) the HOH bend. A C_{2V} structure is assumed for the water molecule and the plotted area covers 90% of a water molecule with nearly C_{2V} symmetry in liquid water.

mainly arises from the coupling between the HOH bend and the OH stretch. That is, the fluctuation of a HB can be probed through the coupling between the HOH bend and the OH stretch.

The above results suggest that the frequency fluctuation of the OH stretch is caused by the intermolecular HB stretch and the libration, while that of the HOH bend by the OH stretch as well as the intermolecular HB bend. Finally, the author analyzed the reason why the frequency of the HOH bend is modulated by the OH stretch, but that of the OH stretch is not by the HOH bend. To elucidate the mechanism of the frequency fluctuation of the HOH bend caused by the OH stretch, the author examined how the intramolecular structure affects the normal mode frequencies of the OH stretch and the HOH bend in liquid water. As seen in figures 4.6(a) and 4.6(b), the frequency of the OH stretch depends almost only on the OH distance, whereas that of the HOH bend indeed depends on both the HOH angle and the OH distance. As a result, the frequency fluctuation of the HOH bend is caused by the coupling the OH stretch, but that of the OH stretch is not significantly affected by the HOH bend.

4.4 Conclusions

In the present study the author investigated the frequency fluctuations of the OH stretch and the HOH bend in liquid water from MD simulations with the TTM3-F *ab inito*-based potential. The 2D IR spectra and peak shifts of the OH stretch and HOH bend were calculated directly from the third-order response function, for which only the high temperature approximation is used.

The 2D IR spectrum of the OH stretch at the waiting time $T = 0$ fs is diagonally elongated because of the strong correlation between ω_1 and ω_3. The calculated decrease in the diagonal width and corresponding increase in the anti-diagonal width with increasing waiting time are due to the loss of the initial inhomogeneity. The slope of 2D IR spectra of the OH stretch in liquid

water suggests three processes, i.e. an initial decay with a time constant of ~40 fs, a plateau from 60 to 100 fs, and a slow decay with a time constant of ~180 fs, similar to those of the OH stretch in liquid D_2O, though these processes in liquid H_2O are faster than those in liquid D_2O. Normal mode analysis suggests that the frequency fluctuation of the OH stretch mainly arises from the intermolecular HB stretch and the librational motion.

The present calculation revealed that the ultrafast decay of the frequency correlation of the HOH bend, i.e. the 2D IR spectrum at $T = 0$ fs already leans to the ω_1 axis. The frequency fluctuation of the HOH bend consists of three processes: an initial spectral diffusion with a time constant of ~60 fs, a plateau from 100 to 150 fs, and a slow decay with a time constant of ~120 fs. The time evolution of the normal mode frequency of the HOH bend along equilibrium MD trajectories reveals the strong couplings between the frequency of the HOH bend and the OH stretch as well as the intermolecular HB bend. Although the direct coupling between the HOH bend and the intermolecular HB stretch is not large, the effect of the intermolecular HB stretch, i.e., the fluctuation of the HB environment, via the OH stretch is seen as the plateau region from 100 to 150 fs in the time evolution of the slope of the 2D IR spectra and the peak shift. The present results demonstrate that the coupling between the HOH bend and the OH stretch is essential to reproduce the correct properties of the HOH bend though the coupling can have minimal effect on the frequency fluctuation of the OH stretch.

References of chapter 4

[1] D. Eisenberg and W. Kauzmann. *The structure and properties of water*. Clarendon Press, 1969.

[2] A. Rahman and F. H. Stillinger, J. Chem. Phys. **55**, 3336 (1971).

[3] I. Ohmine and H. Tanaka, Chem. Rev. **93**, 2545 (1993).

[4] T. Head-Gordon and G. Hura, Chem. Rev. **102**, 2651 (2002).

[5] I. Ohmine and S. Saito, Acc. Chem. Res. **32**, 741 (1999).

[6] E. T. J. Nibbering and T. Elsaesser, Chem. Rev. **104**, 1887 (2004).

[7] S. T. Roberts, K. Ramasesha, and A. Tokmakoff, Acc. Chem. Res. **42**, 1239 (2009).

[8] T. Yagasaki and S. Saito, Acc. Chem. Res. **42**, 1250 (2009).

[9] H. J. Bakker and J. L. Skinner, Chem. Rev. **110**, 1498 (2010).

[10] T. Yagasaki and S. Saito, Annu. Rev. Phys. Chem. **64**, 55 (2013).

[11] S. Mukamel, Principles of nonlinear optical spectroscopy, *Oxford*, 1999.

[12] M. Cho, Chem. Rev. **108**, 1331 (2008).

[13] J. D. Evans, J. J. Loparo, C. J. Fecko, S. T. Roberts, A. Tokmakoff, and P. L. Geissler, Proc. Natl. Acad. Sci. **102**, 13019 (2005).

[14] J. B. Asbury, T. Steinel, K. Kwak, S. A. Corcelli, C. P. Lawrence, J. L. Skinner, and M. D. Fayer, J. Chem. Phys. **121**, 12431 (2004).

[15] J. J. Loparo, S. T. Roberts, and A. Tokmakoff, J. Chem. Phys. **125**, 194522 (2006).

[16] K. Ramasesha, S. T. Roberts, R. A. Nicodemus, A. Mandal, and A. Tokmakoff, J. Chem. Phys. **135**, 054509 (2011).

[17] M. L. Cowan, B. D. Bruner, N. Huse, J. R. Dwyer, B. Chugh, E. T. J. Nibbering, T. Elsaesser, and R. J. D. Miller, *Nature* **434**, 199 (2005).

[18] D. Kraemer, M. L. Cowan, A. Paarmann, N. Huse, E. T. J. Nibbering, T. Elsaesser, and R. J. D. Miller, Proc. Natl. Acad. Sci. **105**, 437 (2008).

[19] C. P. Lawrence and J. L. Skinner, J. Chem. Phys. **118**, 264 (2003).

[20] B. Auer, R. Kumar, J. R. Schmidt, and J. L. Skinner, Proc. Natl. Acad. Sci. 1**04**, 14215 (2007).

[21] D. Laage, G. Stirnemann, F. Sterpone, and J. T. Hynes, Acc. Chem. Res. **45**, 53 (2011).

[22] A. Paarmann, T. Hayashi, S. Mukamel, and R. J. D. Miller, J. Chem. Phys. **128**, 191103 (2008).

[23] A. Paarmann, T. Hayashi, S. Mukamel, and R. J. D. Miller, J. Chem. Phys. **130**, 204110 (2009).

[24] T. L. C. Jansen, B. M. Auer, M. Yang, and J. L. Skinner, J. Chem. Phys. **132**, 224503 (2010).

[25] J. Jeon, A. E. Lefohn, and G. A. Voth, J. Chem. Phys. **118**, 7504 (2003).

[26] G. S. Fanourgakis and S. S. Xantheas, J. Chem. Phys. **124**, 174504 (2006).

[27] G. S. Fanourgakis and S. S. Xantheas, J. Chem. Phys. **128**, 074506 (2008).

[28] S. Imoto, S. S. Xantheas, and S. Saito, J. Chem. Phys. **138**, 054506 (2013).

[29] T. Yagasaki, J. Ono, and S. Saito, J. Chem. Phys. **131**, 164511 (2009).

[30] S. Mukamel and J. B. Maddox, J. Chem. Phys. **121**, 36 (2004).

[31] T. Hasegawa and Y. Tanimura, J. Chem. Phys. **125**, 074512 (2006).

[32] T. L. C. Jansen, K. Duppen, and J. G. Snijders, Phys. Rev. B **67**, 134206 (2003).

[33] F. Paesani, S. Iuchi, and G. A. Voth, J. Chem. Phys. **127**, 074506 (2007).

[34] S. Habershon, G. S. Fanourgakis, D. E. Manolopoulos, J. Chem. Phys. **129**, 74501 (2008).

[35] F. Paesani, S. S. Xantheas, and G. A. Voth, J. Phys. Chem. B **113**, 13118 (2009).

[36] F. Paesani and G. A. Voth, J. Phys. Chem. B **113**, 5702 (2009).

[37] F. Paesani, S. Yoo, H. J. Bakker, and S. S. Xantheas, J. Phys. Chem. Lett. **1**, 2316 (2010).

[38] J. Liu, W. H. Miller, G. S. Fanourgakis, S. S. Xantheas, S. Imoto, and S. Saito, J. Chem. Phys. **135**, 244503 (2011).

[39] H. Partridge and D. W. Schwenke, J. Chem. Phys. **106**, 4618, 1997.

[40] B.T. Thole, Chem. Phys. **59**, 341 (1981).

[41] M. Khalil, N. Demirdöven, and A. Tokmakoff, Phys. Rev. Lett. **90**, 47401 (2003).

[42] A. Sakurai and Y. Tanimura, J. Phys. Chem. A **115**, 4009 (2011).

[43] Y. Nagata and S. Mukamel, J. Am. Chem. Soc. **132**, 6434 (2010).

[44] T. Ishiyama, V. V. Sokolov, and A. Morita, J. Chem. Phys. **134**, 024509 (2011).

[45] K. Ramasesha, "Dynamics of Water and Aqueous Protons studied using Ultrafast Multi-dimensional Infrared Spectroscopy", Ph. D. thesis at the Massachusetts Institute of Technology (2013) (http://dspace.mit.edu/handle/1721.1/79257).

[46] N. Huse, S. Ashihara, E. T. J. Nibbering, and T. Elsaesser, Chem. Phys. Lett. **404**, 389 (2005).

[47] M. Cho, J. Yu, T. Joo, Y. Nagasawa, S. A. Passino, and G. R. Fleming, J. Chem. Phys. **100**, 11944 (1996).

Chapter 5

Energy relaxation of the OH stretch and the HOH bend in liquid water

5.1 Introduction

Vibrational energy relaxation in liquid water has been intensively investigated by using experimental and theoretical methods because it plays important roles in various chemical reactions in biological systems as well as in liquid water. Pump-probe spectroscopy enables us to analyze the time scales and detailed pathways of the vibrational energy relaxation [1-3]. The vibrational energy relaxation dynamics of the OH stretch in liquid water and heavy water have been investigated. The time scale of the energy relaxation of the OH stretch in liquid heavy water is 700 fs [4]. As shown by Bakker *et al.* [5-7] and Miller *et al.* [8,9], the time scale of the energy relaxation of the OH stretch in liquid water is 200-270 fs, i.e. much faster than that in heavy water. It is considered that the fast energy relaxation of the OH stretch in liquid water is due to the Fermi resonance between the OH stretch and the HOH bend and the strong coupling between the OH stretch and the librational motion [9].

The time scale of the vibrational energy relaxation of the HOH bend in liquid water is 170-260 fs as measured by Elsaesser, Ashihara, and their co-workers [10-13] and Lindner *et al.* [14,15]. Elsaesser, Ashihara, and their co-workers have shown that the fast energy relaxation of the HOH bend is due to the energy transfer to the motion between the HOH bend and the librational motion, i.e. 1000-1500 cm^{-1} [12]. They also found the frequency dependence of the energy relaxation to the mode from 1000 to 1500 cm^{-1} [11].

The energy relaxations of the intramolecular vibrations have also been investigated theoretically. Theoretical calculations of the vibrational energy relaxation are divided into two approaches: One is Landau-Teller theory and another is non-equilibrium molecular dynamics (MD) simulations. In the Landau-Teller theory based on the first-order time-dependent perturbation, the energy relaxation rate of a mode can be calculated from the

time correlation function of the force acting on the mode. Lawrence *et al.* investigated the time scale of the energy relaxation of the OH stretch in liquid heavy water based on the Landau-Teller theory. They obtained the time constant of 2.3-2.7 ps and found that the excess energy of the OH stretch dominantly flows into the overtone of the HOD bend [16,17]. In the Landau-Teller theory, the vibrational mode is treated quantum mechanically and its surrounding environment is governed by classical mechanics. It is, furthermore, assumed that the vibrational mode is independent of the environment. In other words, this theory cannot be applied to the analysis of the energy relaxation of a mode, such as an intermolecular mode or a mode delocalized over several molecules, in which the distinction between the system and its environment is not obvious and the mode largely changes with time.

Non-equilibrium MD simulations have also been used to investigate the vibrational energy relaxation in liquid water and heavy water [18-22]. Kandratsenka *et al.* analyzed the energy relaxation of the OH stretch in liquid heavy water and obtained a time constant of 2.7 ps [18]. Rey et al. studied the vibrational energy relaxation of the HOH bend in liquid water and found that the excess energy of the HOH bend mainly transfers to the high frequency librational motion [19-21]. Bastida *et al.* analyzed the energy relaxation of the HOH bend in liquid water by using hybrid quantum/classical simulations and found that the relaxation is unaffected by nuclear quantum effects [22].

In this chapter, the energy relaxation of the HOH bend and the OH stretch have been investigated by using the theoretical calculation of the pump-probe spectra and the frequency-resolved transient kinetic energy (FR-TKE) analysis [23] with the TTM3-F potential whose intramolecular potential surface is based on the high level ab initio calculations [24]. The pump-probe spectra were directly calculated from the third-order response function, in which the intra- and inter-molecular couplings are considered. The resultant calculated pump-probe spectra show that the energy decays of the HOH bend and

the OH stretch with time constants of 250 and 240 fs, respectively, followed by the transition to the hot ground state.

The FR-TKE analysis probes the time evolution of the change in the density of states after the excitation of a mode, similar to the pump-probe spectra. Its advantage over the theoretical calculation of the pump-probe spectra is its low computational cost. In addition, it is easy to analyze the time evolution of intra- and inter-molecular structures after the excitation because the non-equilibrium trajectories are calculated. The calculated time constants of the energy relaxation of the HOH bend and the OH stretch are 180 and 130 fs, respectively. The author found that the excess energy of the HOH bend dominantly transfers to the high frequency librational motion at ~800 cm^{-1} due to the strong coupling between these motions. The author also found that the presence of the coupling between the HOH bend and the intermolecular HB bend at ~60 cm^{-1}. The present analysis also showed that the excess energy of the OH stretch quickly relaxes to the HOH bend and the high frequency librational motion. It was also found that some portion of the excess energy of the OH stretch relaxes to the HB stretch at ~200 cm^{-1} via the anharmonic coupling. The time evolution of intermolecular structures after the excitation of the HOH bend and the OH stretch are also analyzed.

The computational method and details are outlined in section 5.2. The results are presented and discussed in section 5.3. The conclusion is drawn in section 5.4.

5.2 Computational methods and details

5.2.1 Third-order response function and pump-probe spectra

In the present study, the author directly calculated the third-order IR response function by using non-equilibrium MD simulations. The details about the theoretical calculation of the third-order IR response function and the pump-probe spectra from non-equilibrium MD

simulations are summarized in chapter 2. Here, the author briefly describes the theoretical back- ground and computational details for the third-order nonlinear IR spectroscopy.

Pump-probe spectroscopy measures the third-order polarization, $P^{(3)}(\tau,T,t)$, which is expressed by the convolution of the third-order response function, $R^{(3)}(t_1,t_2,t_3)$, with electric field pulses [25],

$$P^{(3)}(\tau,T,t)=\int_0^\infty dt_3\int_0^\infty dt_2\int_0^\infty dt_1\,E(t_s-t_3,\{\tau_i\})E(t_s-t_3-t_2,\{\tau_i\}) \qquad (5.1)$$
$$\times E(t_s-t_3-t_2-t_1,\{\tau_i\})R^{(3)}(t_1,t_2,t_3),$$

where

$$E(t,\{\tau_i\})=\sum_{i=1}^{3}\varepsilon_i(t-\tau_i)\exp\big(-i\omega_i(t-\tau_i)\big)\exp(-i\mathbf{k}_i\mathbf{r}_i)+\text{ c. c.}. \qquad (5.2)$$

Here, τ_1, τ_2, and τ_3 are the times of the centers of pulses and the three time intervals are defined as $\tau = \tau_2 - \tau_1$, $T = \tau_3 - \tau_2$, and $t = t_s - \tau_3$. The ω_i, k_i, and $\varepsilon_i(t)$ are the carrier frequency, wave vector, and envelope function of the pulse i, respectively. Equation (5.1) can be written as

$$P^{(3)}(\tau,T,t)=\sum_{\alpha=\mathrm{I}}^{\mathrm{IV}}\exp(-i\mathbf{k}_\alpha\mathbf{r})P_\alpha^{(3)}(\tau,T,t)+\text{c. c.}, \qquad (5.3)$$

where $P_{\mathrm{I}}^{(3)}$, $P_{\mathrm{II}}^{(3)}$, $P_{\mathrm{III}}^{(3)}$, and $P_{\mathrm{IV}}^{(3)}$ denote the third-order polarizations generated in the $\mathbf{k}_{\mathrm{I}} = -\mathbf{k}_1 + \mathbf{k}_2 + \mathbf{k}_3$, $\mathbf{k}_{\mathrm{II}} = \mathbf{k}_1 - \mathbf{k}_2 + \mathbf{k}_3$, $\mathbf{k}_{\mathrm{III}} = \mathbf{k}_1 + \mathbf{k}_2 - \mathbf{k}_3$, and $\mathbf{k}_{\mathrm{IV}} = \mathbf{k}_1 + \mathbf{k}_2 + \mathbf{k}_3$ phase matching conditions, respectively.

The third-order response function in Eq. (5.1) is given by [25]

$$R^{(3)}(t_1,t_2,t_3)=\left(\frac{i}{\hbar}\right)^3\text{tr}\{\mathbf{M}(t_1+t_2+t_3)[\mathbf{M}(t_1+t_2),[\mathbf{M}(t_1),[\mathbf{M}(0),\rho_{\mathrm{eq}}]]]\}, \qquad (5.4)$$

where ρ_{eq} and $\mathbf{M}$ are the equilibrium density matrix and total dipole moment operator of the system, respectively. By using the identity [26],

$$\frac{i}{\hbar}[\mathbf{M}(t),\ ] \equiv iL_{\mathbf{M}}(t) = \lim_{\epsilon\to 0}\frac{1}{\epsilon}\{\exp(i\epsilon L_{\mathbf{M}}(t)) - 1\}, \qquad (5.5)$$

where the $iL_{\mathrm{M}}(t)$ is the Liouville operator for the system-field interaction, i.e., $iL_{\mathrm{M}}(t) = \frac{i}{\hbar}[\mathbf{M}(t),\ ]$, the third-order response function can be recast in the from

$$R^{(3)}(t_1,t_2,t_3) = \lim_{\epsilon\to 0}\frac{1}{\epsilon^2}\mathrm{tr}\{\mathbf{M}(t_1+t_2+t_3)(\exp(i\epsilon L_{\mathbf{M}}(t_1+t_2)) - 1) \qquad (5.6)$$

$$\times(\exp(i\epsilon L_{\mathbf{M}}(t_1)) - 1)\frac{i}{\hbar}[\mathbf{M}(0),\rho_{eq}]\}.$$

By applying a classical approximation for the Liouville operator and for the commutator between $\mathbf{M}(0)$ and ρ_{eq}, we obtain the classical expression for the third-order response function based on non-equilibrium MD simulations expressed as [27]

$$R^{(3)}(t_1,t_2,t_3) \propto \langle\mathbf{M}(t_1+t_2\ +t_3)\dot{\mathbf{M}}(0)\rangle_{t_1,t_1+t_2} + \langle\mathbf{M}(t_1+t_2+t_3)\dot{\mathbf{M}}(0)\rangle_{\bar{t}_1,\overline{t_1+t_2}} \qquad (5.7)$$

$$-\langle\mathbf{M}(t_1+t_2+t_3)\dot{\mathbf{M}}(0)\rangle_{\bar{t}_1,t_1+t_2} - \langle\mathbf{M}(t_1+t_2+t_3)\dot{\mathbf{M}}(0)\rangle_{t_1,\overline{t_1+t_2}}.$$

Here $\langle\ \rangle$ indicates the classical ensemble average, the subscripts of each term denote the time of the application of external pulses as the perturbation and the over-bar on the subscripts represents the opposite direction of external pulse based on inverted force method [28].

In pump-probe spectroscopy, the pump pulse makes population state and, then, the absorption change induced by the pump pulse is measured by the probe pulse. The observable of the pump-probe spectroscopy, i.e. the spectrally integrated absorption change at the waiting time T, is given by [25]

$$\Delta\alpha(T) \propto \omega_{\mathrm{probe}}\mathrm{Im}\int dt\ E^{*}_{\mathrm{probe}}(t)\ (P^{(3)}_{\mathrm{I}}(0,T,t) + P^{(3)}_{\mathrm{II}}(0,T,t)) \qquad (5.8)$$

Here ω_{probe} and E_{probe} are the frequency and electric field of the probe pulse. The energy relaxation processes are analyzed by the waiting time dependence of the change in the absorbance.

5.2.2 Frequency resolved transient kinetic energy analysis

In pump-probe spectroscopy, the change in absorption induced by the excitation, i.e. the change in the dipole dynamics in the vibrational or electronic excited state, is measured. The absorption change induced by the excitation can be related to the change in the weighted density of states by the excitation because the absorption, $I(\omega)$, is expressed by the weighted density of states, $\rho_M(\omega)$, i.e.

$$I(\omega) \propto \int \langle M(t)M(0)\rangle e^{-i\omega t}dt \sim \int \sum_n \left(\frac{\partial M}{\partial Q_n}\right)^2 \frac{\cos(\omega_n t)}{\omega_n^2} e^{-i\omega t}dt,$$
$$= \int \rho_M(\omega) \frac{\cos(\omega_n t)}{\omega_n^2} e^{-i\omega t}dt, \qquad (5.9)$$

where Q_n is the normal mode n of the system. Thus, the similar information to the pump-probe spectra on the relaxation dynamics can be obtained by examining the change in the density of states induced by the excitation of a mode. That is, the energy relaxation processes can be analyzed by the time evolution of the difference of the density of states between the non-equilibrium and equilibrium trajectories, i.e. the FR-TKE analysis [23].

The total Hamiltonian of the non-equilibrium MD simulations, $H(t)$, is given by

$$H(t) = H_0 - \sum_i \boldsymbol{\mu}_i \mathbf{E}(t) \qquad (5.10)$$

with

$$\boldsymbol{E}(t) = \mathbf{A}\exp\left(-\frac{t^2}{2\sigma^2}\right)\cos(\omega_{\text{excite}}t + \phi). \qquad (5.11)$$

Here H_0 and $\boldsymbol{\mu}_i$ are the Hamiltonian of the system and the dipole moment of molecule i, A, σ, and φ are the intensity, Gaussian width, frequency, and initial phase of the perturbative electric field, respectively.

The difference between the densities of states in the excited and ground states obtained from the non-equilibrium and equilibrium trajectories from time T to $T+t$ is given by

$$\Delta\tilde{C}(\omega_{t'}, T, \omega_{\text{excite}}) = \frac{1}{2\pi}\int_0^\infty dt' \cos(\omega_{t'} t') \sum_i m_i \langle \mathbf{v}_i(T+t')\mathbf{v}_i(T)\rangle^{\text{NE}}_{\phi,\omega_{\text{excite}}} \qquad (5.12)$$

$$-\frac{1}{2\pi}\int_0^\infty dt' \cos(\omega_{t'} t) \sum_i m_i \langle \mathbf{v}_i(T+t')\mathbf{v}_i(T)\rangle^{\text{EQ}}.$$

Here m_i and $\mathbf{v}_i$ are the mass and velocity of the atom i, the superscripts of NE and EQ indicate the non-equilibrium and equilibrium MD trajectories, respectively. The $\Delta\tilde{C}(\omega_{t'}, T, \omega_{\text{excite}})$ shows the excess energy of ω_t' at the waiting time T. To eliminate the phase dependence, i.e. the coherent state between the ground and excited states in quantum mechanics, of the perturbative electric field, we averaged $\varphi = 0$ and $\varphi = \pi/2$.

5.2.3 Computational details

The TTM3-F interaction potential, which is the latest version of the ab initio-based charge transferable, flexible, polarizable Thole-Type Models (TTM) to describe the underlying inter- and intra-molecular interactions in liquid water is used. The details of the TTM3-F potential are presented in Ref. [24]. The intramolecular interaction and charge transfer of the TTM3-F potential are based on the monomer potential and dipole moment surfaces obtained from high level ab initio calculations, appropriately modified to describe the liquid phase. Because of the intramolecular charge transfer feature, the TTM3-F potential reproduces the increase of the HOH angle in the condensed phase with respect to the gas phase monomer and the correct IR spectrum of the HOH bend. Four interaction sites are used for the inter- molecular interaction in the TTM3-F potential. The oxygen-oxygen interaction is described by a Buckingham expotential-6. A positive charge is placed on each hydrogen atom and a negative charge and an isotropic point dipole moment are placed on the M-site located on the bisector of the HOH angle. The Thole type damping function is employed for the treatment of the electrostatic interaction.

We performed the MD simulation of 64 water molecules under the constant volume and energy conditions at a temperature of 300 K and a density of 1.0 g/cm^3. Periodic boundary conditions were employed and the long-range electric interactions were calculated using the Ewald sum. The induced dipole moment was computed iteratively at each step. Equations of motion were integrated using the velocity-Verlet algorithm with the time step of 0.1 fs. The results of the excitations of the HOH bend and the OH stretch were obtained by averaging over 460,000 and 460,000 trajectories, respectively.

The **A**, σ and ω in the Eq. 5.11 are 0.02 V/Å, 20 fs, and 1600 cm^{-1} for the excitation of the HOH bend and 0.01 V/Å, 10 fs, and 3500 cm^{-1} for the excitation of the OH stretch. The increase in temperature of the system due to the pulse is about 10 K both for the excitation of the HOH bend and the OH stretch.

5.3 Results and discussion

Figures 5.1(a) and 5.1(b) show the time evolution of the differential cross-section of the pump-probe spectrum of the HOH bend with ω_{pump} = 1650 cm^{-1} and the pump-probe signals at (ω_{pump}, ω_{probe}) = (1650 cm^{-1}, 1475 cm^{-1}) and (1650 cm^{-1}, 1650 cm^{-1}). The positive and negative peaks are related to the 1→2 and 0→1 transitions, respectively. Unlike the experimental results [12], the intensity below 1400 cm^{-1} is weak because of the absence of explicit vibrational density of states in classical MD simulations [29]. As seen in Fig. 5.1(a) and 5.1(b), the increase of the positive peak at 1475 cm^{-1} is faster than that of the negative

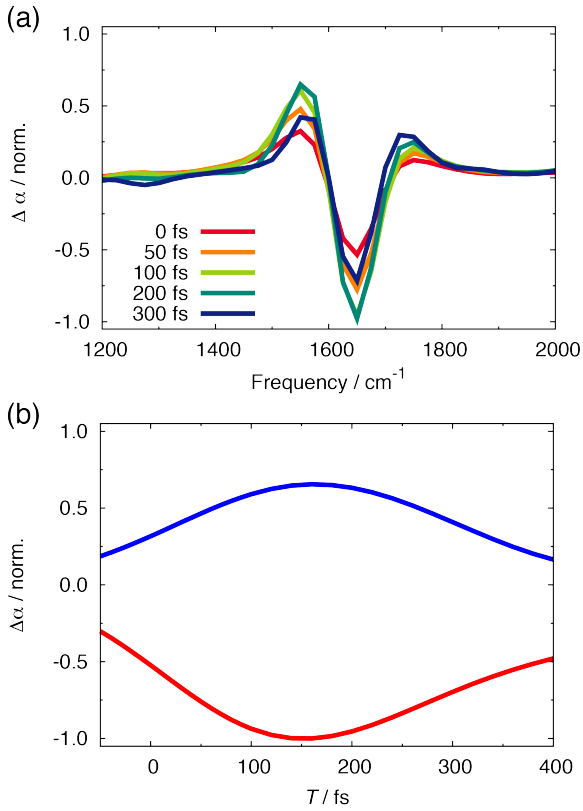

Figure 5.1: (a) Cross-sections of the pump-probe spectrum of the HOH bend. (b) Pump-probe signals of (ω_{pump} ,ω_{probe}) = (1650 cm^{-1}, 1475 cm^{-1}) (red) and (ω_{pump}, ω_{probe}) = (1650 cm^{-1}, 1650 cm^{-1}) (blue).

peak at 1650 cm^{-1} although the both peaks show the maximum intensities at T~100 fs. The difference of the initial response is also reported in the experimental studies [13]. This difference is ascribed to the spectral shift due to the ultrafast energy relaxation to the intermolecular motions. The positive and negative peaks decay with the time constant of 250 fs, which is in agreement with the experimental results of 170-260 fs [10-15]. The detailed energy relaxation of the HOH bend will be discussed below with the data of the FR-TKE analysis.

Figures 5.2(a) and 5.2(b) show the time evolution of the differential cross-sections of the

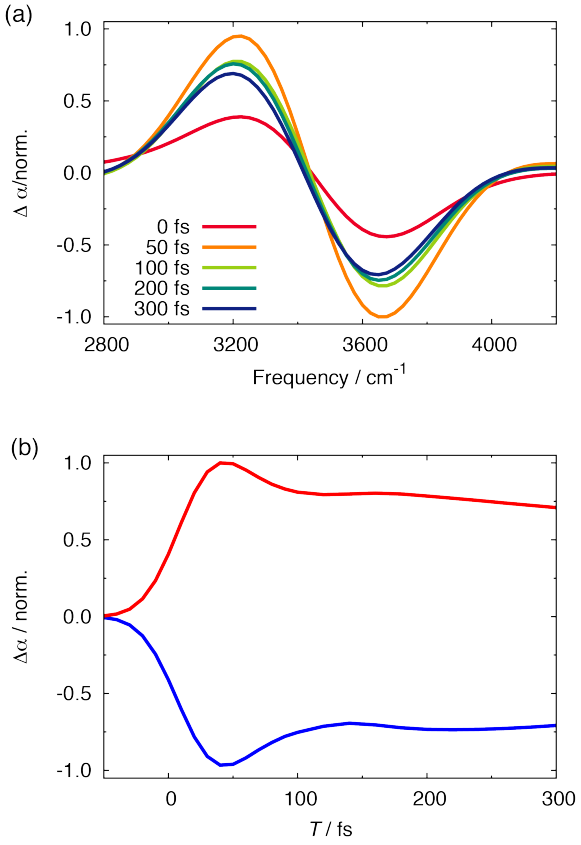

Figure 5.2: (a) Cross-sections of the pump-probe spectrum of the OH stretch. (b) Pump-probe signals of (ω_{pump} ,ω_{probe}) = (3600 cm^{-1}, 3225 cm^{-1}) (red) and (ω_{pump}, ω_{probe}) = (3600 cm^{-1}, 3600 cm^{-1}) (blue).

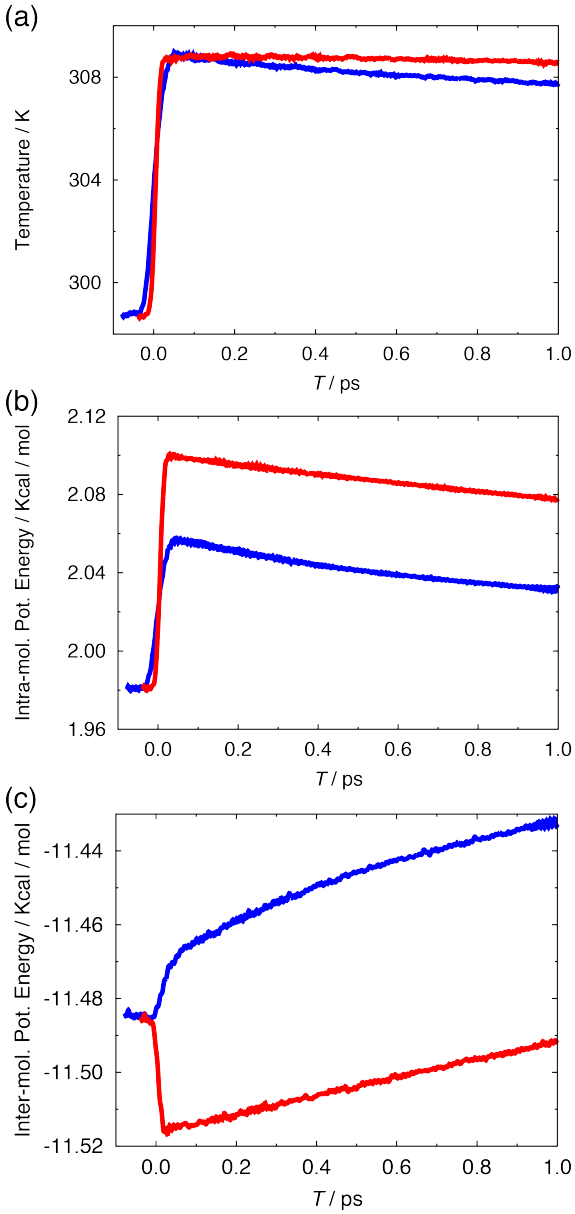

Figure 5.3: (a) Temperature, (b) intramolecular potential energy, and (c) intermolecular potential energy after the excitation of the HOH bend (blue) and the OH stretch (red).

pump-probe spectrum of the OH stretch with ω_{pump} = 3600 cm^{-1} and the pump-probe signals at (ω_{pump}, ω_{probe}) = (3600 cm^{-1}, 3225 cm^{-1}) and (3600 cm^{-1}, 3600 cm^{-1}). The negative and positive peaks slightly shift to the lower frequency region with increasing T due to the thermalization similar to the experimental result [8,9]. The positive and negative peaks

show the initial decay with the time constant of 240 fs, which is in good agreement with the experimental results of 200-270 fs [5-8,14,15], followed by the slow relaxation to the so-called hot ground state, which is a thermalized state with the different HB network structure from the initial state [30].

Although the theoretical calculation of the pump-probe spectra is a powerful tool to investigate the vibrational energy relaxation processes, it demands a lot of computational time be- cause of the slow convergence. We examined the energy relaxation dynamics by using non- equilibrium MD simulations and the FR-TKE analysis.

Figures 5.3(a)-(c) show the kinetic energy, i.e. temperature, intramolecular potential energy, and intermolecular potential energy of the system after the excitation of the HOH bend and the OH stretch. With increasing the waiting time *T* after the excitation of the HOH bend, both the kinetic energy and the intramolecular potential energy monotonically decrease while the intermolecular potential energy monotonically increases (blue lines in Figs. 5.3(a)-(c)). These three energies show the decay with a time constant of 0.6-1.0 ps for the relaxation to the hot ground state [23].

Unlike the excitation of the HOH bend, the kinetic energy reaches the maximum at *T*~200 fs after the excitation of the OH stretch (red line in Fig. 5.3(a)). In addition, in the excitation of the OH stretch the intermolecular potential energy is initially stabilized by ~0.03 kcal/mol because the strengthening of the HBs due to the intramolecular OH distance increases by the excitation of the OH stretch. The kinetic energy and intra- and inter-molecular potential energies after the excitation of the OH stretch decay with the time constants of 0.6-1.0 ps similar to the excitation of the HOH bend.

Figure 5.4 (a) shows the DOS of liquid water, and figures 5.4(b) and 5.4(c) present the FR-TKEs after the excitation of the HOH bend and the OH stretch, respectively. The both results clearly display that the intermolecular motions seen below 1000 cm^{-1} can be divided

into the four regions: the HB bend (0-80 cm^{-1}), the HB stretch (80-250 cm^{-1}), the low frequency librational motion (250-500 cm^{-1}), and the high frequency librational motion (500-1000 cm^{-1}).

Figure 5.4(b) shows the presence of the strong coupling between the HOH bend and the high frequency librational motion at ~800 cm^{-1}, i.e. the emergence of the ultrafast energy flow

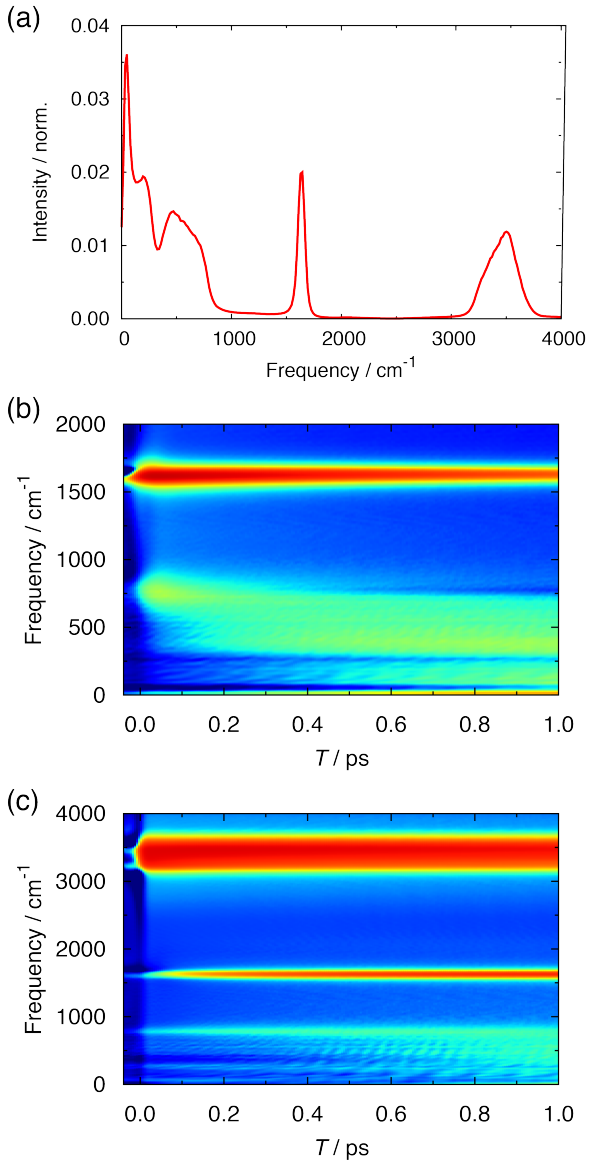

Figure 5.4: (a) DOS of liquid water. FR-TKE analysis of (b) the HOH bend and (c) the OH stretch.

to the high frequency librational motion after the excitation of the HOH bend. In addition, the intermolecular HB bend motion at ~60 cm^{-1} also quickly responds to the excitation of the HOH bend. The couplings between the HOH bend and the high frequency librational motion as well as the HB bend are also found in the analysis of the frequency fluctuation of the HOH bend in chapter 4.

Figure 5.4(c) shows the OH stretch strongly couples with the HOH bend and the high frequency librational motion. In addition to these strong couplings, the OH stretch also directly couples to the intermolecular HB stretch at ~200 cm^{-1}.

The author analyzed the detailed energy relaxation processes from the HOH bend in terms of the integrated energy defined by

$$I(T;\omega_{\min},\omega_{\max}) = \int_{\omega_{\min}}^{\omega_{\max}} \Delta\,\tilde{C}(\omega_{t'},T,\omega_{\text{excite}})\,d\omega_{t'}. \qquad (5.13)$$

for the six regions, i.e. 1000-1400 cm^{-1} and 1400-1800 cm^{-1} (the HOH bend) and four regions in the intermolecular motions.

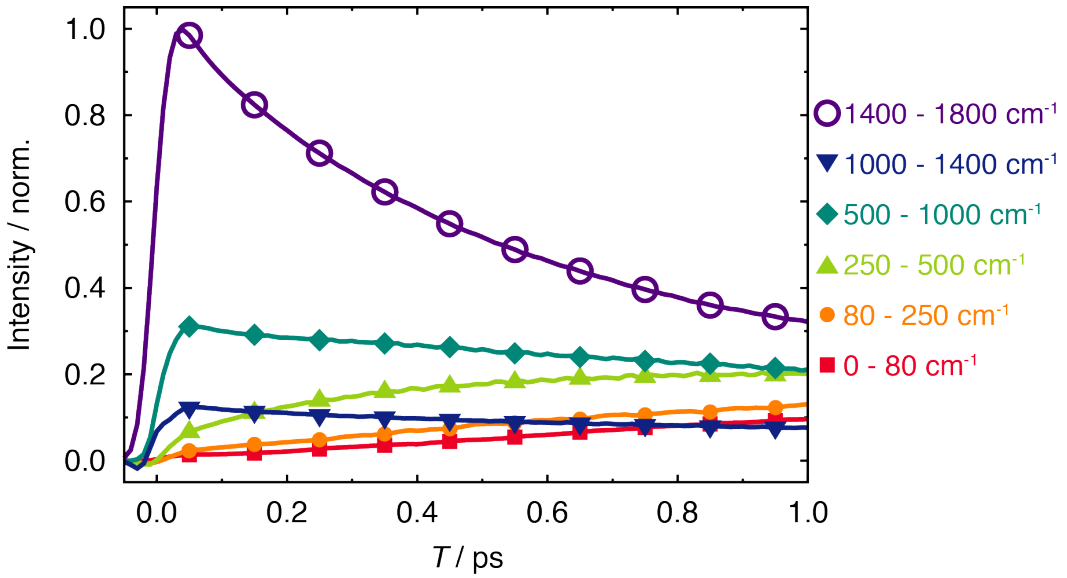

Figure 5.5: Time evolution of the excess energies of the motions after the excitation of the HOH bend.

Figure 5.5 displays the time evolution of the excess energies in the six regions. The excess energy of the HOH bend shows the initial decay with a time constant of 180 fs, which is corresponds to the time constants of 250 fs and 170-200 fs obtained from the theoretical and experimental pump-probe spectra [10-15], followed by the decay with time constants of ~0.5 ps due to the transition to the hot ground state. The energy of the high frequency libration shows the sharp increase at T~0 ps because the strong coupling between the HOH bend and the high frequency librational motion. The excess energy of the high frequency librational motion decays with the time constants of 80 and 600 fs. The fast and slow relaxations correspond to the relaxations of the high frequency librational motion and the relaxation to the hot ground state [12,23,30].

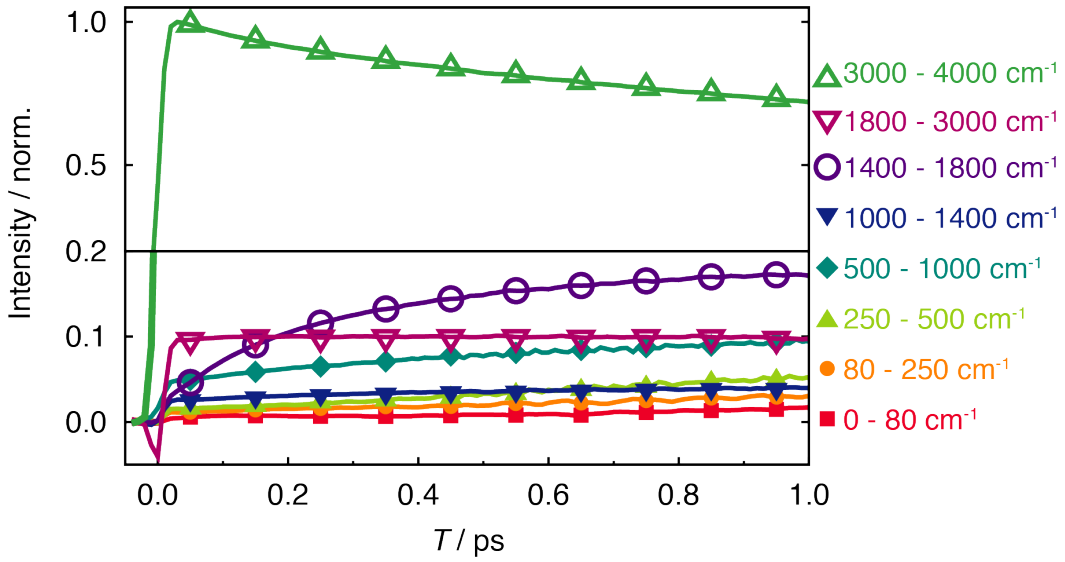

Figure 5.6: Time evolution of the excess energies of the motions after the excitation of the OH stretch.

The author analyzed the energy relaxation dynamics after the excitation of the OH stretch by dividing the frequency regions into eight regions, i.e., 1800-3000 cm^{-1}, 3000-4000 cm^{-1} (the OH stretch), and the six regions below the HOH bend. Figure 5.6 displays the change in the excess energies in the eight regions. The excess energy of the OH stretch shows the fast decay with time constants of 70 and 220 fs, and ~500 fs. The time constant of 70 fs originates from the energy relaxation to the high frequency librational motion. As a result, the excess energy of the high frequency librational motion increases faster than that of the HOH bend. The time constant of 220 fs, which corresponds to the time constant of 240-270 fs in the theoretical and experimental pump-probe spectra [5-9,11,12,14,15], is assigned to the energy relaxation from the OH stretch to the HOH bend. The time constant of 500 fs is due to the transition to the hot ground state. Figure 5.6 also shows the excess energy of the HOH bend increases with the time constant of 270 fs. In addition, we can see the impulsive increase in the excess energy of the HB stretch due to the anharmonic coupling between the OH stretch and the HB stretch. The anharmonic coupling is also found in the analysis of chapter 4.

The changes in liquid structure after the excitation of the OH stretch and the HOH bend were examined. Figure 5.7(a) shows the oxygen-oxygen radial distribution function, $g_{OO}(r)$, in the equilibrium state at 300 K and Figs. 5.7(b) and 5.7(c) show the time evolution of the difference between $g_{OO}(r)$ calculated from the non-equilibrium and equilibrium trajectories. The time evolution of $g_{OO}(r)$ after the excitation of the HOH bend is similar to that after the excitation of librational motion [23]. For the excitation of the HOH bend, the change in $g_{OO}(r)$ is induced by the weakening of the HBs due to the increase in temperature. The first peak of $g_{OO}(r)$ decreases with time constants of 150 fs and 0.9 ps due to the transition of the hot ground state. In contrast to the change in $g_{OO}(r)$ after the excitation of the HOH bend, $g_{OO}(r)$ shows the initial rise at r~2.8 Å after the excitation of the OH stretch. This initial rise

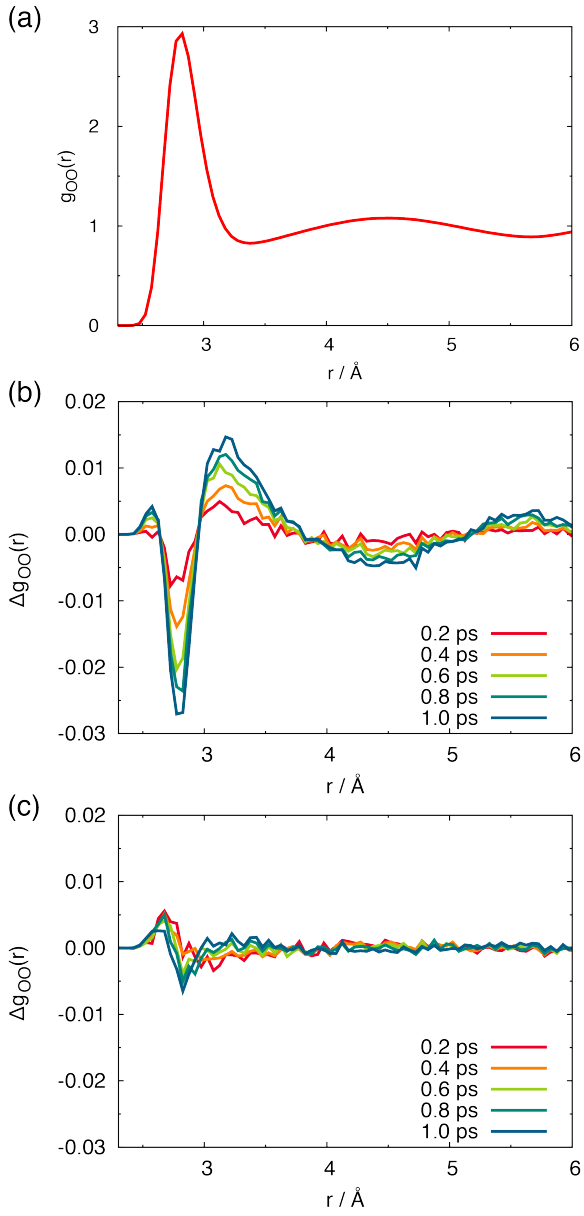

Figure 5.7: (a) Oxygen-oxygen radial distribution function, $g_{OO}(r)$, in the equilibrium state at 300 K. Time evolution of the difference in $g_{OO}(r)$ between the equilibrium state and the non-equilibrium state after the excitation of (b) the HOH bend and (c) the OH stretch.

is related to the rapid increase in the energy of the intermolecular oxygen-oxygen stretch, i.e. the HB stretch, after the excitation of the OH stretch as seen in Fig. 5.3. At long waiting times, $g_{OO}(r)$ after the excitation of the OH stretch is similar to that after the excitation of the

HOH bend because the change in liquid structure is governed by the weakening of the HBs due to the transition to the hot ground state.

5.4 Conclusion

The author studied the vibrational energy relaxation of the HOH bend and the OH stretch in liquid water by using the theoretical calculation of the pump-probe spectra and the FR-TKE analysis with the *ab initio*-based TTM3-F potential. The pump-probe spectra are calculated from the directly calculated third-order response function. The calculated pump-probe signal of the HOH bend showed the fast initial increase in the frequency region of the $1 \rightarrow 2$ transition compared with that of the $0 \rightarrow 1$ transition and the vibrational energy relaxation with a time constant of 250 fs. These temporal behaviors are in agreement with the experimental results [13]. The pump-probe signal of the OH stretch shows the decay with the time constant of 240 fs, followed by the transition to the hot ground state.

The details of the energy relaxation dynamics were examined by using the FR-TKE analysis. The fast energy relaxation of the HOH bend is due to the strong coupling with the high frequency librational motion. The present result also shows that some portion of the HOH bend energy directly relaxes to the intermolecular HB bend. The FR-TKE of the OH stretch shows time constants of 70 and 220 fs. These fast energy relaxations are caused by the strong coupling of the OH stretch to the high frequency librational motion as the HOH bend. As already elucidated in the theoretical study by Yagasaki and Saito, the energy of the high frequency librational motion relaxes to the low frequency librational motion with a time constant of ~60 fs and the subsequent cascading energy relaxations to the low frequency motions. The present analysis indeed shows that all the motions are strongly coupled and the fast thermalization is realized in liquid water.

The author also examined the time evolution of liquid structure after the excitation of the HOH bend and the OH stretch. The difference of the liquid structure between the excitation

of the HOH bend and the OH stretch can be seen for the short waiting times, whereas the difference disappears for the long waiting times.

References of chapter 5

[1] E. T. J. Nibbering and T. Elsaesser, Chem. Rev. **104**, 1887 (2004).

[2] H. J. Bakker and J. L. Skinner, Chem. Rev. **110**, 1498 (2010).

[3] T. Yagasaki and S. Saito, Annu. Rev. Phys. Chem. **64**, 55 (2013).

[4] C. J. Fecko, J. J. Loparo, S. T. Roberts, and A. Tokmakoff, J. Chem. Phys. **122**, 054506 (2005).

[5] S. Woutersen, U. Emmerichs, H. Nienhuys, and H. J. Bakker, Phys. Rev. Lett. **81**, 1106 (1998).

[6] S. Woutersen and H. J. Bakker, Phys. Rev. Lett. **83**, 2077 (1999).

[7] S. Woutersen and H. J. Bakker, Nature **402**, 507 (1999).

[8] M. L. Cowan, B. D. Bruner, N. Huse, J. R. Dwyer, B. Chugh, E. T. J. Nibbering, T. Elsaesser, and R. J. D. Miller, *Nature* **434**, 199 (2005).

[9] D. Kraemer, M. L. Cowan, A. Paarmann, N. Huse, E. T. J. Nibbering, T. Elsaesser, and R. J. D. Miller, Proc. Natl. Acad. Sci. **105**, 437 (2008).

[10] N. Huse, S. Ashihara, E. T. J. Nibbering, and T. Elsaesser, Chem. Phys. Lett. **404**, 389 (2005).

[11] S. Ashihara, N. Huse, A. Espagne, E. T. J. Nibbering, and T. Elsaesser, Chem. Phys. Lett. **424**, 66 (2006).

[12] S. Ashihara, N. Huse, A. Espagne, E. T. J. Nibbering, and T. Elsaesser, J. Phys. Chem. A **111**, 743 (2007).

[13] S. Ashihara, S. Fujioka, and K. Shibuya, Chem. Phys. Lett. **502**, 57 (2011).

[14] J. Lindner, P. Vöhringer, M. S. Pshenichnikov, D. Cringus, D. A. Wiersma, and M. Mostovoy, Chem. Phys. Lett. **421**, 329 (2006).

[15] J. Lindner, D. Cringus, M. S. Pshenichnikov, and P. Vöhringer, Chem. Phys. **341**, 326 (2007).

[16] C. P. Lawrence and J. L. Skinner, J. Chem. Phys. **117**, 5827 (2002).

[17] C. P. Lawrence and J. L. Skinner, J. Chem. Phys. **119**, 1623 (2003).

[18] A. Kandratsenka, J. Schroeder, D. Schwarzer, and V. S. Vikhrenko, J. Chem. Phys. **130**, 174507 (2009).

[19] F. Ingrosso, R. Rey, T. Elsaesser, and J. T. Hynes, J. Phys. Chem. A **113**, 6657 (2009).

[20] R. Rey, F. Ingrosso, T. Elsaesser, and J. T. Hynes, J. Phys. Chem. A **113**, 8949 (2009).

[21] R. Rey and J. T. Hynes, Phys. Chem. Chem. Phys. **14**, 6332 (2012).

[22] A. Bastida, J. Zúñiga, A. Requena, and B. Miguel, J. Chem. Phys. **131**, 204505 (2009).

[23] T. Yagasaki and S. Saito, J. Chem. Phys. **134**, 184503 (2011).

[24] G. S. Fanourgakis and S. S. Xantheas, J. Chem. Phys. **128**, 074506 (2008).

[25] S. Mukamel, "Principles of nonlinear optical spectroscopy" Oxford (1999).

[26] S. Mukamel and J. B. Maddox, J. Chem. Phys. **121**, 36 (2004).

[27] T. Hasegawa and Y. Tanimura, J. Chem. Phys. **125**, 074512 (2006).

[28] T. I. C. Jansen, K. Duppen, and J. G. Snijders, Phys. Rev. B **67**, 134206 (2003).

[29] J. Liu, W. H. Miller, G. S. Fanourgakis, S. S. Xantheas, S. Imoto, and S. Saito, J. Chem. Phys. **135**, 244503(2011).

[30] T. Yagasaki, J. Ono, and S. Saito, J. Chem. Phys.**131**, 164511 (2009).

Chapter 6

General Conclusion

The present thesis has been devoted to the studies of liquid water by calculating linear and nonlinear spectroscopy of liquid water with the state of the art model potential, TTM3-F. In particular, the author has investigated the fluctuation and relaxation dynamics of the OH stretch and the HOH bend in liquid water. The author started chapter 2 with the theoretical backgrounds of linear and nonlinear spectroscopy, the basis of MD simulations, and the details of the TTM3-F potential. The first topic in chapter 3 describes the spectral difference between ice and liquid water. The second topic in chapter 4 describes the frequency fluctuation of the OH stretch and the HOH bend in liquid water. The third topic in chapter 5 describes the vibrational energy relaxation of the OH stretch and the HOH bend in liquid water.

In chapter 3, the difference in the IR intensities of the HOH bend between ice and liquid water was investigated. The IR spectra of ice and liquid water were decomposed into the components arising from the permanent, induced, and cross terms. The author found that the IR intensity of the HOH bend in ice is weakened by the strong anti-correlation between the permanent dipole moment of a molecule and the induced dipole moment of its HB acceptor molecules. This anti-correlation is small in liquid water because of the disordered HB structure. The author also found that the OH stretch shows a positive correlation between the permanent dipole moment of a molecule and the induced dipole moment of its HB acceptor. Since the ordered HB structure increases the positive correlation, the IR intensity of the OH stretch in ice is larger than that in liquid water.

In chapter 4, the author investigated the frequency fluctuations of the OH stretch and the HOH bend in liquid water by using the theoretical calculations of the 2D IR spectra. The slope of 2D IR spectra of the OH stretch in liquid water suggests three processes of the

frequency fluctuation, i.e. an initial decay with a time constant of ~40 fs, a plateau from 60 to 100 fs, and a slow decay with a time constant of ~180 fs, similar to those of the OH stretch in liquid D_2O, though these processes in liquid H_2O are faster than those in liquid D_2O. The present calculation revealed that the ultrafast decay of the frequency correlation of the HOH bend. The frequency fluctuation of the HOH bend consists of three processes: an initial spectral diffusion with a time constant of ~60 fs, a plateau from 100 to 150 fs, and a slow decay with a time constant of ~120 fs. The time evolution of the normal mode frequency of the HOH bend along equilibrium MD trajectories reveals the strong couplings between the frequency of the HOH bend and the OH stretch as well as the intermolecular HB bend.

In chapter 5, the author investigated the vibrational energy relaxation of the HOH bend and the HOH bend in liquid water by using the theoretical calculation of the pump-probe spectra and the FR-TKE analysis. The results showed that the energy relaxation with a time constant of 180-250 fs for the HOH bend and 70-240 fs for the OH stretch. The author also found that the excess energy of the HOH bend transfers to the high frequency librational motion and that of the OH stretch relaxes to both the HOH bend and the high frequency librational motion. The most of the excess energy for $T > 1$ ps is dissipated into the low frequency intermolecular motions, i.e. the relaxation to the hot ground state and, thus, the difference between the excitation of the HOH bend and the OH stretch becomes small. The present analysis indeed shows that all the motions are strongly coupled and the fast thermalization is realized in liquid water.

In conclusion, the author elucidated the molecular details of the fluctuation and relaxation of the OH stretch and the HOH bend in liquid water. The advantage of MD simulations and theoretical calculations over experiments is that they provide the molecular mechanism of the fluctuation and relaxation dynamics. The author revealed that the frequency fluctuation of the HOH bend is very fast because the HOH bend strongly couples to

the OH stretch, the librational motion, and the HB bend. The dynamics of the HOH bend is sensitive to the change in the HB structure. It is required to analyze the effects of the temperature change and the existence of solutes on the dynamics of the HOH bend. Although the theoretical calculation of the third-order response function by using non-equilibrium MD simulations is a powerful tool to analyze the dynamics in condensed phases, its calculation is time consuming. It is needed to develop a new computational method which calculates the third-order response function more easily than the present method.

The preset results show that the energy relaxation from the intramolecular motions to the intermolecular motions is mediated by the high frequency librational motion. That is, the high frequency librational motion directly receives the excess energy of the OH stretch and the HOH bend and, then, it immediately transfers the energy to low frequency intermolecular motions. This efficient energy transfer is related to ultrafast energy dissipation caused by chemical reactions in liquid water. As noted above, the energy relaxation dynamics is sensitive to the change in the HB structure. It is required to study the relationship between the HB structure and the energy relaxation dynamics.

The time constant of the energy relaxation of the OH stretch is validated by several groups. However, the detail of the energy relaxation pathway of the OH stretch is controversial, i.e. it is not known whether the excess energy of the OH stretch transfers to two HOH bends of two molecules or the HOH bend and librational motion of the same molecule. The author is currently studying the spatial information about the energy relaxations of the OH stretch and the HOH bend by using the single molecule excitation. This study would provide the answer of the above issue.

Nevertheless, there are many problems on the linear and nonlinear spectra of liquid water. The present calculation cannot reproduce the broadening of the IR spectrum of the HOH bend

in ice compared to that in liquid water. The calculated IR spectrum of the HOH bend in ice is narrower than that in liquid water. The discrepancy between experimental results and theoretical calculation seems to be caused by the inaccurate description of the HB in ice. Since the polarizability of the TTM3-F potential is isotropic, the TTM3-F potential underestimates the difference of the HB binding energies in the different HB structures. It is desirable to calculate the IR spectrum of the HOH bend in ice by using the TTM2.1-F potential or AMOEBA force field which consider anisotropic induced dipole moment and improve the HB binding energy in ice.

Quantum effects are non-negligible for high frequency vibrational motions, although the present studies, i.e. theoretical calculation of the third-order response function and FR-TKE analysis, are based on classical mechanics. While the violation of the detailed balance condition cannot be avoided if classical MD simulations are employed, nuclear quantum effects, e.g. zero-point energy and tunneling effect, can be considered by using semi-classical theories. The IR spectrum of liquid water calculated by using the LSC-IVR, which is one of semi-classical theories, indicates the presence of large nuclear quantum effects between the librational motion and the HOH bend. The pump-probe experiments of the HOH bend suggest the importance of the mode between the librational motion and the HOH bend for the energy relaxation of the HOH bend. However, the present study cannot quantitatively reproduce the ultrafast energy transfer from the HOH bend to the mode between the librational motion and the HOH bend. The theoretical calculation of the third-order response function combined with semi-classical theories could provide a new insight on the energy relaxation dynamics of liquid water. The author thinks that the theoretical studies on the above problems provide a deeper understanding of dynamics in liquid water.